Characterisation and modelling of nitrogen plasmas for the deposition of nanostructured GaN using different plasma sources

THÈSE N^{O} 6202 (2014)

PRÉSENTÉE LE 11 JUILLET 2014
À LA FACULTÉ DES SCIENCES DE BASE
CRPP - PROCÉDÉS PLASMAS
PROGRAMME DOCTORAL EN PHYSIQUE

ÉCOLE POLYTECHNIQUE FÉDÉRALE DE LAUSANNE

POUR L'OBTENTION DU GRADE DE DOCTEUR ÈS SCIENCES

PAR

David MARTINET

acceptée sur proposition du jury:

Prof. F. Mila, président du jury
Dr C. Hollenstein, Prof. M. Q. Tran, directeurs de thèse
Dr M. Gindrat, rapporteur
Prof. N. Grandjean, rapporteur
Prof. H. Kersten, rapporteur

ÉCOLE POLYTECHNIQUE
FÉDÉRALE DE LAUSANNE

Suisse
2014

"Ce n'est qu'en essayant continuellement
que l'on finit par réussir.
Autrement dit: plus ça rate,
plus on a de chances que ça marche."
Devise Shadok

Un problème sans solution
est un problème mal posé.
Albert Einstein

To my parents, Cathy and Roger,
and my brother, Sébastien

Abstract

This thesis presents an experimental investigation of RF and DC arc plasma sources used at low gas pressure ($10^{-4}-10^{-2}$ mbar), for the deposition of structured GaN layers directly on silicon wafer, in order to increase the growth rate and lower the costs. The aim is to characterise the nitrogen plasmas from both plasma sources, exhibiting different electron energy distribution functions (EEDF), and their influence on the plasma composition to increase the growth rate. Numerical simulations were developed to understand the underlying physics in such low pressure plasmas, and the predictions are compared to the experimental plasma parameters and composition.

Langmuir probe measurements were used to determine the EEDF in both plasma sources: a Maxwell distribution in the RF plasma source, and a Maxwell with an electron beam superposed in the DC plasma source, due to the accelerating voltage. The plasma composition, determined by means of optical emission spectroscopy, was found to be similar with the different plasma sources in the various configurations tested. The variation of the external parameters caused slight changes in the ratio of excited state densities, but no fundamental modifications were observed. Nevertheless the plasma density is sensitive to these changes and can vary from $10^{15}-10^{17}$ m^{-3}. The admixture of Ga vapour in such plasmas does not affect the nitrogen composition and plasma density, as the fraction of Ga is very low, below 1%. The uniformity of the plasma is better than 5% with the RF plasma source, but worse than 10% with the DC plasma source. This is due to the electron beam penetrating into the chamber and being only slightly affected by the collisions. The current in the DC arc discharge and the use of magnetic field are the principal parameters which lead to a non-uniformity of the plasma which is directly linked to the deposition profile. The developed collisional-radiative model showed good agreement with the experiment in the electron temperature determination as well as in the plasma composition. The dominant reactions occurring in plasmas at low gas pressures have thus been identified.

In parallel to the plasma diagnostics, GaN layers were deposited and their morphology, uniformity and growth rates were correlated to the plasma parameters. The structure can be either 2D bulk layer or 3D nanocolumns with both plasma sources, depending on the density ratio of the N and Ga. The growth rates are dependent on the plasma density, which determines the density of atomic nitrogen. The typical growth rate using the RF plasma source is 1.5 μm/h. The maximal growth rate reached with the DC plasma source is 6.9 μm/h showing a nanocolumnar shaped deposition, higher than with the typical MOCVD deposition technique ($\sim$ 4 μm/h) or MBE systems ($\sim$ 2 μm/h).

KEYWORDS: nitrogen plasma, low pressure, collisional-radiative model, GaN, nanocolumn, silicon wafer, Langmuir probe measurement, optical emission spectroscopy.

Résumé

Ce travail a pour objet la caractérisation expérimentale de plasmas d'azote utilisés à basse pression ($10^{-4} - 10^{-2}$ mbar), créés par des sources plasma RF et DC. Ces plasmas sont utilisés pour la déposition de couches nano-structurées de GaN, afin d'augmenter le taux de dépôt et diminuer leur coût de fabrication. Les deux types de sources plasma présentent des fonctions de distribution d'énergie des électrons (EEDF) différentes. Leur influence sur la composition du plasma afin d'augmenter la vitesse de croissance est discutée. Des simulations numériques ont été développées afin de comprendre les phénomènes physiques dans les plasmas à basses pressions. Leurs prédictions sont comparées aux résultats expérimentaux, en termes de paramètres plasma ainsi que de composition du plasma.

Des mesures de sonde Langmuir ont été faites afin de déterminer l'EEDF dans les deux sources plasma: une distribution de Maxwell avec la source RF et une distribtion de Maxwell surmontée d'un faisceau électronique avec la source DC, à cause du potentiel d'accélération. La composition du plasma, analysée par spectroscopie optique, est similaire pour les deux sources plasma dans différentes configurations testées. La variation des paramètres extérieurs a un effet négligeable sur les densités d'états excités. En revanche, la densité plasma y est sensible et varie entre $10^{15} - 10^{17}$ m^{-3}. L'injection de vapeur de Ga dans de tels plasmas n'affecte ni la composition ni la densité du plasma d'azote, car la fraction de Ga est inférieure à 1%. L'uniformité du plasma est inférieure à 5% avec la source RF, mais supérieure à 10% avec la source DC, dû au faisceau électronique pénétrant dans la chambre, car il est très peu amorti par les collisions. Le courant de la décharge ainsi que l'application d'un champ magnétique sont les principaux paramètres altérant l'uniformité du plasma, qui est directement liée au profil de la déposition. Le modèle collisionnel-radiatif développé est en bon accord avec les mesures déterminant la température électronique et la composition du plasma. Les principales réactions dans le plasma à basse pression ont donc été identifiées.

Parallèlement à la caractérisation du plasma, des dépositions de couches de GaN ont été faites. Leurs morphologies, uniformités et vitesses de croissance ont été corrélées aux paramètres plasma. La structure des dépôts peut être bi- ou tri-dimensionnelle (nano-colonne) avec les deux sources plasma, selon la valeur du rapport de densités entre N et Ga. Les vitesses de croissance dépendent de la densité plasma, laquelle détermine la densité d'azote atomique. A titre de comparaison, la vitesse de croissance obtenue avec la source RF est de l'ordre de $1.5\,\mu$m/h, et la vitesse maximale a été atteinte avec la source DC, et est de $6.9\,\mu$m/h, tout en exhibant un dépôt nano-colonnaire. Cette dernière est supérieure à celle obtenue à l'aide des techniques standard MOCVD ($\sim 4\,\mu$m/h) et MBE ($\sim 2\,\mu$m/h).

MOTS-CLES: plasma d'azote, basse pression, modèle collisionnel-radiatif, GaN, nano-colonne, substrat de silicium, mesures de sonde Langmuir, spectrocopie optique.

Contents

Introduction

The market for light emitting diodes (LED) based lighting applications has reached a significant size, mainly due to new applications for LED lighting. Some examples are backlight units for liquid crystal display (LCD) screens used for laptop computers and high-end television sets, architectural lighting, outdoor displays, and ultimately general illumination, where LEDs are already starting to replace the incumbent technologies of incandescent and fluorescent light bulbs and tubes. The deployment of LEDs into these applications is driven by their higher energy efficiency, longevity and versatility in terms of design, flexibility and colour tuning.

Gallium nitride (GaN) is one of the most important materials among the wide-band-gap nitrides for the above mentioned optical devices. The current costs for end customers of commercially available white high-power LEDs are still high when compared to incandescent tubes. A major reason for the high costs is the complexity of the manufacturing processes used today for the fabrication of the nitride semiconductor layers which lie at the core of blue and white LEDs. The state-of-the-art manufacturing technique is MOCVD (Metal Organic Chemical Vapour Deposition), which is based on high process temperatures (up to $\approx 1100°$C) and involves both toxic precursors and the need for complex and expensive security systems. Another manufacturing challenge lies in the lack of a bulk crystal growth process for GaN and thus the need for using foreign substrate materials like sapphire [1]. Growing GaN films of sufficient quality on sapphire involves growing a relatively thick GaN buffer layer [2], which is costly and time-consuming. An additional limiting element to the efficiency of LEDs is the rather large refractive index of the nitride semiconductor materials involved, leading to a large fraction of light being reflected at the device surface. Beside this, sapphire poses severe problems, such as the difficulty to be cleaved or the fact that it cannot be made conductive [3].

The use of silicon can solve all these difficulties, but there are still problems in achieving good crystal quality of GaN because of the large lattice mismatch (which is around 17% [4]) and the difference of thermal expansion coefficient as well as surface chemistry.

Studies of the heteroepitaxial growth of GaN on silicon substrates have been made [5–9], but a nucleation layer between the silicon and the GaN is often used, in order to reduce the lattice mismatch. For the last decades, silicon as a substrate has attracted much attention for the epitaxial growth of III-V compounds. Thus, the integration of Si- and GaN-based devices on the same chip becomes feasible as well as a silicon based optoelectronics technology. However, despite the large efforts made, no real breakthrough has been obtained because of the high mobility of dislocations in these materials, leading to a rapid degradation of all devices fabricated so far [4].

An interesting approach addressing both the current need for thick GaN buffer layers and the difficult light extraction from devices is the main motivation for the use of nanostructured semiconductor materials. Nitride based nanocolumns (NCs) are the subject of intense research since the past decade because of their unique properties and potential applications in electronic and optoelectronic domains [9]. Contrary to continuous layers, NCs overcome the lattice-mismatch with the substrate through misfit dislocations localised at the interface [10]. It is now commonly recognised that they are largely free of defects [11]. NCs have also the advantages of strongly reducing the effect of total internal reflection, and being easily grown at a very high level of structural perfection without the need for thick buffer layers. Therefore, nanocolumns are excellent candidates to develop arrays of highly efficient nanolight-emitters in the infrared-visible-ultraviolet range. Furthermore, these nanostructured films can also be grown on inexpensive substrates like silicon [9]. Hence, by using an innovative manufacturing technology for the cost-efficient production of such nanostructured nitride semiconductor films, a highly competitive process technology would be available to serve a fast-growing market of energy-saving lamps.

This innovative manufacturing technology could require the use of plasmas. In fact, plasmas are widely used in industry for various applications where a high deposition rate and good crystallinity are required. The main domains of application concern lighting, material etching, ion implantation, electric discharge machining, waste treatment, plasma thrusters or even thin film deposition. The photovoltaic industry uses radio-frequency (RF) capacitively coupled plasmas for the deposition of thin film silicon layers not only for the high deposition rate, but also for the good uniformity, making possible the growth of large area solar cells and flat displays [12]. The plasma techniques are also used in the deposition of hard coatings with a plasma torch [13–15], for the deposition of diamond (tooling industries) or for aircraft engines, or in the packaging industry, where the deposition of barrier films is made on polymer foils [16, 17]. Plasmas are also used for high speed welding, in electric discharge machining, allowing the machining of conductive materials nearly independently of their hardness, such as steel or titanium, or in the engraving industries, for the production of re-writeable CDs or DVDs. The use of plasmas in industries are not only limited to the high speed, but also for the chemical possibilities at low gas temperature operation, such as for the sterilisation of medical tools [18, 19], and these techniques are still under investigation [20–23].

For the current application, nitrogen plasma is needed to supply atomic nitrogen onto the substrate for the growth of GaN. Nitrogen plasmas are also used in industry for other applications, such as the watch industry, to change the chemical composition of the first atomic layers of ceramics [24, 25], or for lighting applications, because the light emitted by a nitrogen plasma can be nearly a white spectrum [26]. The range of pressure where such plasmas are used goes from the ultra high vacuum (UHV) to atmospheric pressure. Growth of GaN is already made with the help of nitrogen plasmas in plasma-assisted molecular beam epitaxy (PA-MBE) [11, 27, 28]. In these deposition systems the plasma source acts as an atomic nitrogen source. However the plasma used in these techniques has not been studied, thus better depositions could be made if the plasma would be optimized.

Nitrogen plasmas have also taken an important place in the research because of its properties. Plasmas of molecular gases are complex due to the large quantity of interactions between the gas and the electrons, such as the rotational and vibrational excitations. Many groups are still working on the modelling of such plasmas, taking into account more and more reactions to explain the behaviour in the glow discharge or even in the afterglow, in order to understand and use this type of plasma in pulse mode. Loureiro, Guerra *et al.* intensively investigated the modelling in the mbar range [29–37], Zhu *et al.* tried to develop methods to easily extract the plasma parameters from the plasma diagnostics (Langmuir probe and optical emission spectroscopy) [38–42], other groups try to understand atmospheric pressure nitrogen plasma, as it is the main component of air, for the aircraft industry or space applications. Active research is also done on beam plasmas, which have the advantages of low electron temperature and high plasma density producing low ion energies, in order to control the electron energy distribution function (EEDF) to have less damages due to the ion bombardment [43, 44]. The modelling of EEDF for different plasma sources at various pressure has also been a topic of an abundant literature.

The domain of application of the present thesis work is thin film deposition. The aim is to investigate the plasma composition in order to understand the effect of the plasma on the deposition of nano-structured GaN layers (NCs), by evaporating gallium in a nitrogen plasma. The purpose of the present work is to study nitrogen plasma in order to develop and manufacture GaN substrates which differentiate from the current state-of-the-art by reducing the production cost, investigating a deposition technique at higher N_2 pressure and using a novel nanostructured surface morphology. This latter will enable the manufacturing of higher-efficiency LEDs, compared to the current state-of-the-art, by providing a high density of small areas of nearly perfect crystallinity for the actual light generation.

In the application presented here the pressure range is limited to $10^{-4} - 10^{-2}$ mbar, because of the use of effusion cell for the evaporation of Ga. The nitrogen pressure used in this work is higher than in the PA-MBE techniques, leading to a high proportion of background nitrogen molecules for the same atomic nitrogen available for the growth, which is new with respect to the actual plasma assisted techniques. This thesis work will focus on the nitrogen plasma obtained in this pressure range, the influence of the external parameters, such as the electrical power, the gas pressure or the magnetic field, and the possible ways to tune them in order to increase the density of the desired species, with a change of the EEDF by changing the plasma source. The plasmas will be characterised by means of Langmuir probe and optical emission spectroscopy to extract the plasma parameters. Numerical models have been developed to understand the mechanisms occurring in such a low pressure regime, whose literature is not yet abundant. They will be presented and compared to the results of the experimental measurements. Besides the plasma characterisation, GaN depositions will be presented and the layer analysis results will be correlated with the plasma parameters.

The thesis has the following structure: In chapter 1 the two different plasma reactors used for this work are presented. Chapter 2 introduces the diagnostics used for the plasma characterisation and for the deposited layer analysis. In chapter 3 the models developed to simulate the nitrogen plasma are presented and their predictions are discussed. The experimental results obtained with the different plasma sources are presented in chapters 4 and 5. Chapter 6 presents the experimental results of the plasma characterisation with the evaporation of gallium. Finally chapter 7 exhibits the deposited layers and the correlation between plasma parameters and deposited layers, before concluding the work.

1 Plasma reactors

In this chapter the two plasma reactors used in this work will be presented: the LEP[1] device, a research reactor with a direct current (DC) plasma source installed, and the LEPEVPE[2] deposition system, used with both radio frequency (RF) and DC plasma sources where all the deposition experiments were made. The LEP device was originally used for epitaxial film growth and was manufactured by *OC Oerlikon* (former Unaxis). The LEPEVPE system is a home built deposition vessel, based on the LEP configuration, used for the deposition of gallium nitride for lighting application in a previous project [45].

Two reactors were used to separate the plasma characterisation and the deposition of GaN layers. The LEP device was not equipped with a Ga evaporation system, and this reactor has more view-ports available for the plasma diagnostics than the deposition reactor. As no deposition were made in this reactor, the handling and modifications of electrical configurations (see below) were easier, and the UHV and clean conditions, necessary for epitaxial growth, were not necessary.

Since the LEPEVPE deposition system was the only reactor equipped with a RF plasma source, it was thus used to characterise the nitrogen plasmas created with this plasma source, before the first depositions of GaN. Once the deposition procedures were run, the openings of the reactor, to modify the configuration of the plasma source or the electrical configurations, were minimised, in order to reduce at maximum the contaminations from the atmosphere (oxygen, water vapour, ...). Therefore, the reactor was no more suitable for the plasma characterisation. The degassing and the heating of the reactor for the cleaning are also factors which led to the favouring of the LEP device for the characterisation of the nitrogen plasmas using a DC plasma source.

---

[1] LEP : Low Energy Plasma

[2] LEPEVPE : Low Energy Plasma-Enhanced Vapour Phase Epitaxy

1.1 Reactor with DC plasma source

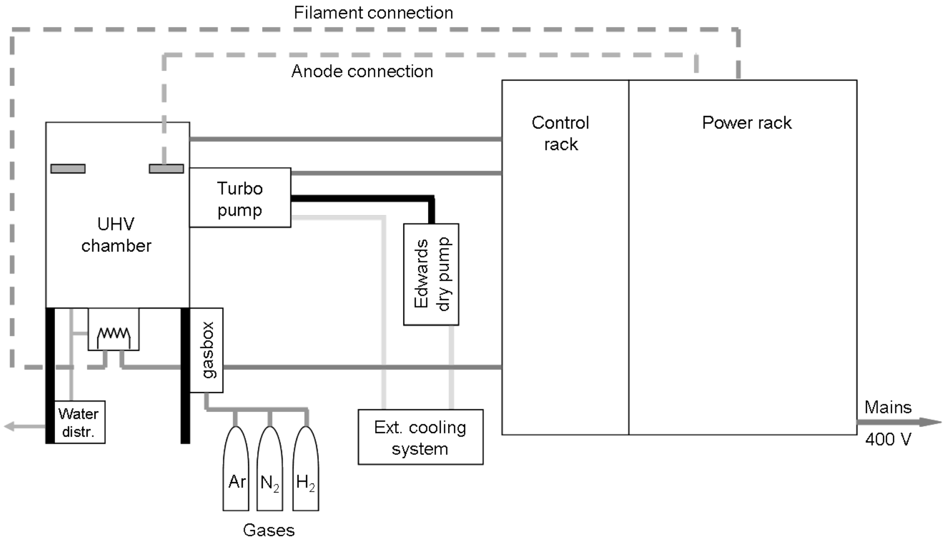

Figure 1.1: Schematic view of the LEP experimental setup [46].

Figure (1.1) shows schematically the LEP experiment together with the equipment needed to produce a plasma. The whole setup, described more in details hereafter, consists of an UHV chamber, its dedicated vacuum pumping system, gas lines for the different gases composition and two water cooling systems: for the chamber and for the vacuum pumps.

The power rack contains the DC current source for producing the plasma. In this Fronius DPS 400 power supply a low pass filter is installed to reduce the electrical noise on the output [46]. The control rack contains the turbo pump controller, the pressure gauges readings and the main control of the system via a SEAL $S5703N$ control computer.

Plasma reactor

The reactor is schematically shown in figure (1.2). The system consists of a water cooled metal-sealed UHV chamber (7), which is pumped by a dry pumping system (4). The inner vessel dimensions are $r = 29$ cm and $h = 56.5$ cm. An ionisation source (10) is attached to the bottom of the chamber, containing a tantalum or tungsten filament (8) heated by an AC current. The ionisation source is separated from the reactor by a separation plate (9) containing in its centre a 6 mm diameter hole. Another separation plate, containing 37 holes of 2 mm diameter, was tested to improve the uniformity of the plasma density, due to the multiplicity of the "electron showers" (see chapter 5 and figure (1.4) below). Both plates are shown in figure (1.3). To initiate the discharge, the filament is heated and a voltage between filament and anode (3) is applied. A DC power source generates a low voltage high current DC discharge (5) of typically $10-20$ A and a voltage of $20-50$ V, depending on the gas pressure. The generated plasma can be diagnosed by

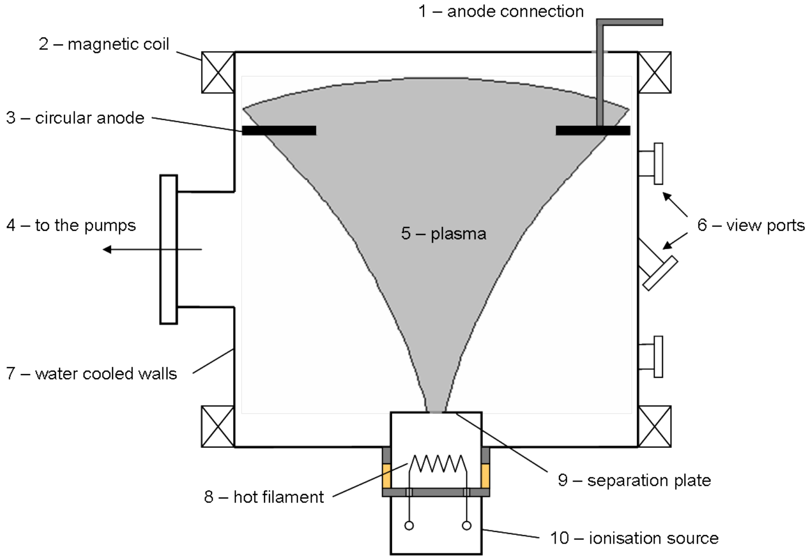

Figure 1.2: Schematic view of the LEP plasma reactor [46].

several view ports (6). The device is called *Low Energy Plasma* (LEP) device because the temperature of the ions is near the room temperature and thus the energy of the ions produced in this discharge for the deposition can be as low as 15 eV, a necessary condition for successful epitaxial growth [47, 48].

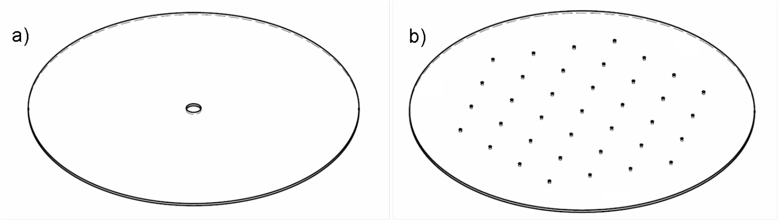

Figure 1.3: Scheme of the two separation plates used in the LEP reactor to investigate the uniformity of the plasma density: *(a)* single hole and *(b)* multi holes.

Nitrogen and argon gases are fed directly into the ionisation source. A magnetic field produced by two magnetic coils (2) in Helmholtz configuration can be applied, leading to a maximal magnetic field on the reactor axis of 45 G. The DC power source is connected on one end to the filament and the other end to the anode (1), whose shape and position in the reactor have been varied during the work, and the electrical circuit is closed by the plasma. The reactor was already set up in the framework of a previous PhD work [46].

Ionisation source and plasma sources

The ionisation source consists of a small cylindrical box made of graphite, with a radius of $r = 8.5$ cm and a height of $h = 16$ cm. Electrical vacuum feedthroughs are installed in the bottom cover for the electrical connection of the tungsten heating filament. The thermionic production of fast electrons used for the ignition of the plasma arc is typically achieved with an AC heating current of 150 A in the filament and an applied voltage V_{fil} of about 8 V. This heating current is obtained from a transformer connected to the mains circuit with 400 V AC. The DC plasma source is a Fronius DPS 400, connected to the anode (+) and the centre of one of the transformer coils (-). The applied DC voltage accelerates the electrons towards the anode, ionising the gas in the reactor chamber. This feature creates an electron beam (or plasma plume) penetrating into the chamber, as shown in figure (1.4), whose shape and length depend on the plasma conditions and the separation plate used. Further discussion on the plasma plume is made in chapter 5. The electrical scheme of the reactor is given in figure (1.5). In this configuration the anode is electrically floating with respect the grounded chamber, but in some cases the anode was electrically connected to the vessel. This affects the voltage of the filament, which becomes negative, and the whole chamber acts as an anode.

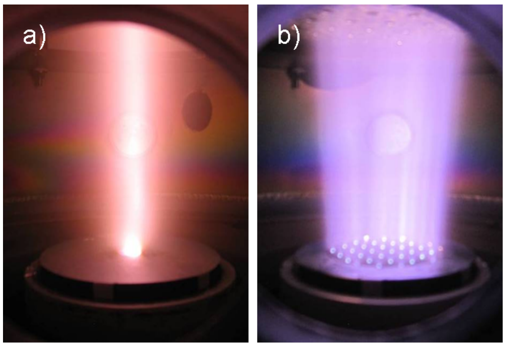

Figure 1.4: Pictures of the source exit with a magnetic field showing *(a)* single hole separation plate with a nitrogen plasma and *(b)* multi-holes separation plate with an argon plasma.

As the distance between anode and filament is about 50 cm, it can be difficult to ignite the plasma only with the applied DC voltage, which is limited to 75 V in our case. Therefore a 22 Ω resistance can be connected to the ionisation source for plasma ignition support. It acts as a temporary second anode, closer to the filament, and is disconnected again after ignition takes place. The DC voltage can rise up to the limit of the DC power source if the desired arc current is too high.

Pumping system

A dry pumping system (Edwards $iH1800$) pumps down the process system through a bypass connection from atmosphere to a medium vacuum of about $5 \cdot 10^{-3}$ mbar. A turbopump (type $STP-A2203C$) evacuates the vacuum chamber to UHV. The pump has a nitrogen purge facility to minimise corrosive attack of the pump motor and sensor coils. In absence of leaks the base pressure obtained with the turbo pump is about 10^{-6} mbar.

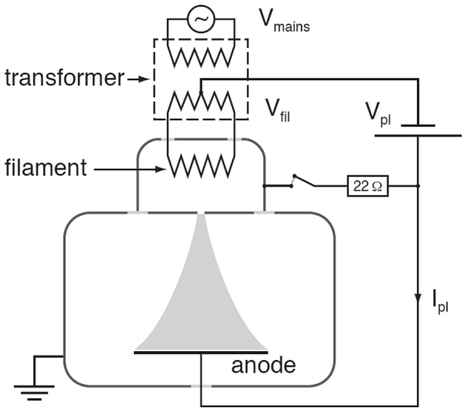

Figure 1.5: Electrical circuit of the LEP reactor [46].

Cooling water circuit

The system is cooled down using two distinct water cooling systems. One system is responsible for the cooling down of the dry primary pumps and the turbo pump. A second in-house water cooling system, using deionised water, is used to cool the reactor chamber, the ionisation source and the electrical feedthrough of the circular anode.

Computer control system

A SEAL $S5703N$ is used as computer control system. It handles 16 analog input and 8 analog output channels as well as 16 digital in- and output channels. The programming is done graphically, comparable to LabVIEW from National Instruments. The system controls the gas flows, the DC plasma current, the magnetic field, the AC filament heating current, gas valves and security issues such as the cooling water flow or pneumatic valves.

Magnetic field

The magnetic field produced by the Helmholtz coils reaches 45 G on axis at a maximum current of 10 A. The coils have 276 spires and a total resistance of $1.9\,\Omega$. The radius of the coils is $R = 340$ mm and the distance between the coils is $d = 685$ mm. With such magnetic field strength, the plasma exhibits a columnar shape, due to the magnetisation of the electrons.

Different electrical configurations

To test different electrical configurations and to characterise more in details the behaviour of DC plasmas, the LEP device was used. Two ports for Langmuir probe measurements (section 2.1.1), one close and one far from the plasma source, were used to measure the changes in the plasma density, electron beam energy and electron temperature of the bulk Maxwellian distribution. Four view ports have been used for the optical emission spectroscopy (OES) measurements (section 2.1.2), the farest being a large horizontal window. This window was used to check the uniformity of the plasma using the optical fibre, and to compare the profiles obtained with the profiles of the movable Langmuir probe, measured 9 cm closer to the source (see on figure (1.6)). The port close to source was also used to measure the plasma plume. In this plume, created by the electron beam produced by the accelerating voltage, the composition is different than in the bulk plasma, because a different electron energy distribution function (EEDF) is expected. The size of the plume changes with the plasma parameters, in particular with the gas pressure, the external magnetic field and the different electrical configurations tested. The figure (1.7) shows pictures of the plume at the separation plate exit with increasing pressure. The discharge current makes the plume propagating up to the top of the reactor, because the accelerating voltage is increased to sustain the discharge. The energy of the primary electrons and thus their path in the reactor are increased. The magnetic field forces the electrons to follow the magnetic field lines, thus it increases the path of the primary electrons in the reactor. Finally the gas pressure increases the collision frequency, thus the electron beam is attenuated due to the collisions close to the source exit. This affects the shape of the plume, which broadens and its length is decreased, as on the pictures. At $p = 10^{-4}$ mbar, the plasma plume is visible by eye at the horizontal window as a brighter slice of plasma in the centre of the reactor. Controlling the plasma plume is important for the process, because energetic electrons can be present and can modify the surface chemistry, when the plume reaches the substrate.

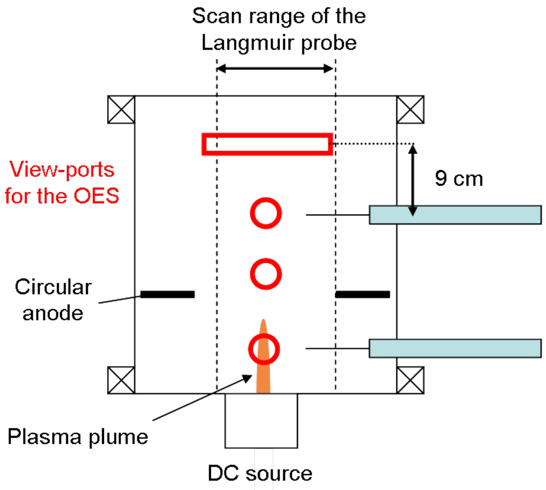

Figure 1.6: Different positions of the Langmuir probe in the LEP device. More view-ports are available for the OES system (red circles).

The different electrical configurations tested are schematically shown in figure (1.8). Note that the grids used with the multi-holes separation plate (figure (1.3)) have the same

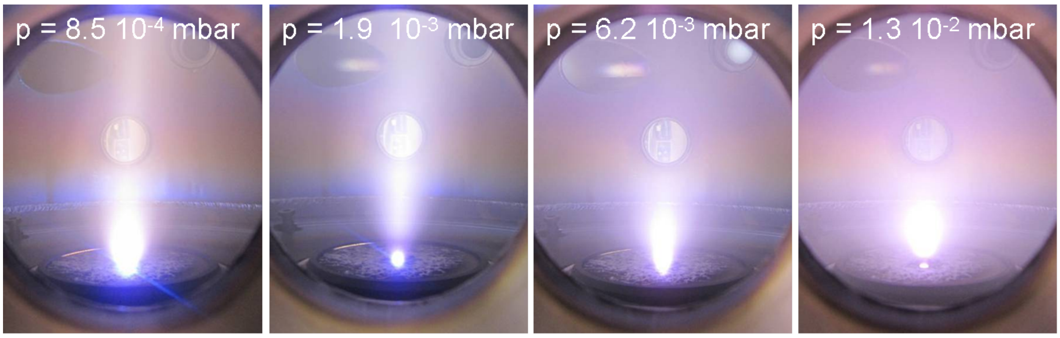

Figure 1.7: Pictures of the separation plate, showing the evolution of the plasma plume as a function of the pressure in argon, without external magnetic field.

pattern as the separation plate, and are different than the grid used with the single hole separation plate. In some cases, the anode has been set floating with respect to the grounded walls of the chamber. This has an effect on the floating and plasma potentials. If the anode is grounded, the most positive potential is the ground, i.e. 0 V. The plasma potential will then be some volts, typically $3-4$ V. But if the anode is floating, it can be polarised up to 15 V, making the plasma potential rising up to about 20 V. The difference of potential between the plasma potential and the ground determines the maximal energy that can have ions hitting a grounded surface, for example the substrate. The change of anode connection affects also the floating potential of the plasma, which is the point where no net current is drawn (section 2.1.1). The floating potential can be used as an indicator of the electron beam energy. The confinement tube (4. in figure (1.8)) is an aluminium foil rolled in a circular shape inserted inside the circular anode, in order to reduce the radius of the reactor.

1.2 Deposition reactor with RF and DC plasma sources

Beside the LEP experiment equipped with a DC plasma source, another UHV reactor was used for the deposition of GaN. This plasma reactor could be used with a RF plasma source or with a DC plasma source, similar to the one of the LEP reactor. A modification of the EEDF is expected due to the change of plasma source. Figure (1.9) presents the deposition system with the equipment needed.

The LEPEVPE setup is very similar to the one of the LEP presented previously. Additionally to the plasma diagnostics, some characterisation methods are mounted on the vessel to probe the growth *in situ*, making the reactor configuration more complex than the LEP device. Due to requirements for epitaxial growth, the base background pressure before deposition is about $2 \cdot 10^{-9}$ mbar. To reach such low base pressure, the reactor needs to be heated up for several days, to get rid of the contamination and the outgassing of the reactor walls. These conditions make the reactor much less suitable for plasma

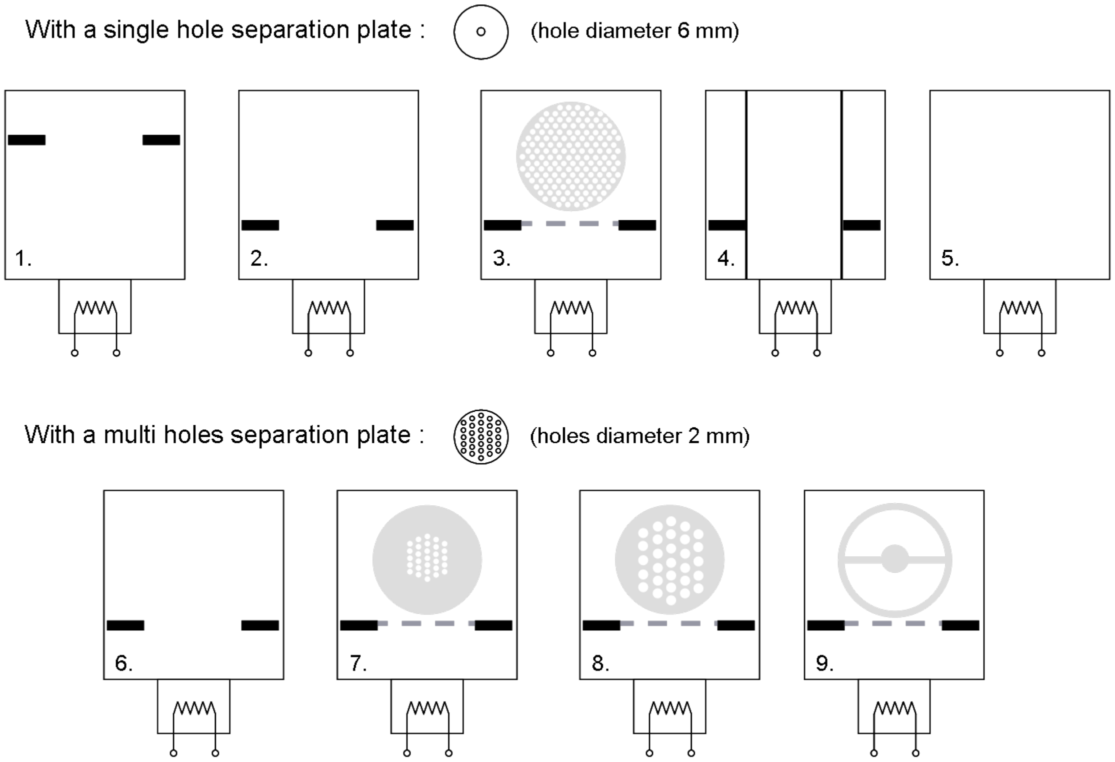

Figure 1.8: Electrical configurations tested in the LEP device: 1. circular anode far from source; 2. circular anode close to the source; 3. gridded anode; 4. with a confinement tube; 5. without anode; 6. circular anode close to the source; 7. gridded anode with tiny holes (5 mm diameter); 8. gridded anode with larger holes (10 mm diameter); 9. with a central disc of 80 mm diameter.

characterisation. The power rack contains the RF generator for the RF plasma source, different electrical power sources for the Ga cell, the magnetic field coils, the sample heater and the DC current source for the DC plasma. The control rack is constituted of the Reflection of High-Energy Electron Diffraction (RHEED) gun controller, the pressure gauges reading, the Eurotherms controlling the temperatures in the reactor (heater, cell, ...), the pneumatic valves (gas valves, cell opening, ...) and the flux meter controller. The Eurotherms and all controllers are interconnected by means of the software LabView.

The experimental reactor is shown schematically in figure (1.10). The system consists of a UHV chamber (13) with water cooled walls, in order to maintain the wall temperature as stable as possible during deposition processes. The vessel inner dimensions are $r = 27.5$ cm and $h = 57$ cm. The chamber is pumped down through a main turbopump (6), and additional turbo pumps are used for the various connected diagnostics and the load lock assembly (7). On top of the chamber is the sample heater assembly (1), which is not only used to heat the wafer (8), but also to rotate the substrate holder (3) and thus the wafer. The assembly is equipped with a lifting system, which allows to tune the distance between the plasma source (15) and the wafer. At the bottom of the chamber the plasma

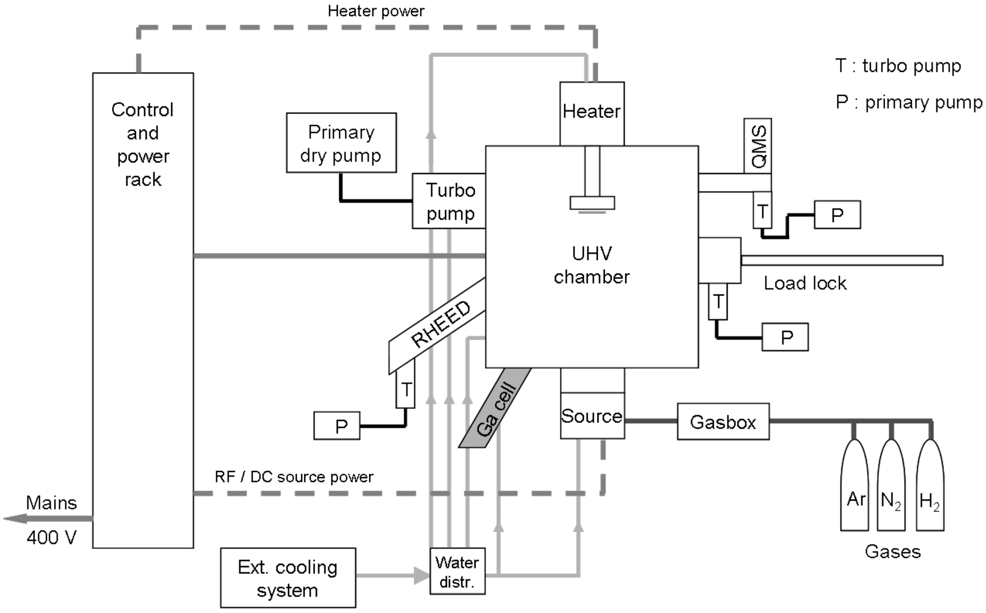

Figure 1.9: Schematic view of the deposition system in the laboratory.

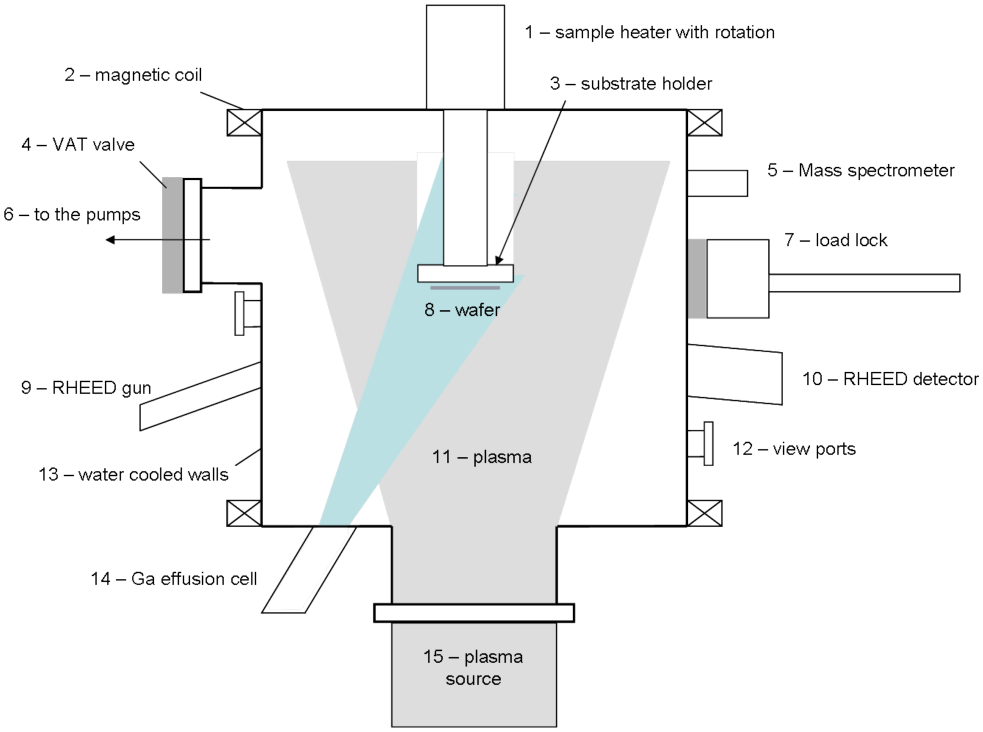

Figure 1.10: Schematic view of the LEPEVPE deposition reactor.

source is fixed. The reflectometry system (laser and detector), pyrometer, effusion cells (14) are also mounted on the bottom plate. Some additional diagnostics are mounted on the vessel, such as RHEED gun (9) (Staib Instruments) and screen (10), quadrupole mass spectrometer (5) (QMA 200 M from Pfeiffer Vacuum) and several view ports (12) for optical emission spectroscopy. The plasma (11) is produced by the RF or DC source and expands into the deposition chamber. The plasma can be confined by two magnetic coils (2) in Helmholtz configuration, with a maximal magnetic field on the reactor axis of 45 G, at a current of 20 A. The load lock assembly consists of a pumping station and a magnetic transfer mechanism used to insert wafer into the main chamber. The load lock is isolated from the main chamber by a valve (4).

Effusion cells

The gallium (99.999% purity) is injected into the plasma by means of an effusion cell (Muscle MS540 from Addon Riber). Effusion cells are the most common type of molecular beam epitaxy (MBE) source, usually fitted with a removable, open-faced crucible having a large exit aperture. The solid Ga is placed in the crucible, made of pyrolytic boron nitride (PBN) in our case, which is heated by two independent filaments. Ga melts at about 30°C and starts to evaporate above 800°C. The filament at the top of the crucible regulates the out coming flow of Ga. With this kind of double filament cell with independent control of the power in both filaments, the power is regulated with a Eurotherm (type 2408 from Invensys), a thermocouple is used to allow closed-loop feedback control. The out coming flux is calibrated via a flux gauge (ionisation gauge GP350 from Granville-Philips), measuring the beam equivalent pressure (BEP). The cell is mounted on the bottom flange of the vessel, and oriented in such a way to inject Ga to the middle of the wafer. The typical BEP used is 10^{-6} mbar, low compared to typical nitrogen pressure range of $10^{-4} - 10^{-2}$ mbar. To uniformalise the Ga distribution on the wafer, this latter is rotated.

Plasma sources

The RF commercial plasma source (CCR technologies, [49]) shown in figure (1.11) consists of an assembly of magnetic field coil, a plasma beam extraction unit (in our case a grid), a gas distribution system and a high frequency matching system.

RF power is injected to the antenna, using an external high frequency generator (13.56 MHz, Apex 7 kW Advanced Energy), and is limited to 1500 W. The incorporated matching system is used to reduce the reflected power from the electrode. The working gas is injected into the plasma chamber by the gas distribution system into the plasma source. The boundaries of the plasma chamber are held at ground potential. The coupling of power into the plasma is mainly inductive and is set into the plasma by a high frequency power connection. To increase its efficiency, a transverse magnetic field, necessary for the excitation of resonance effects, is applied across the excitation electrode and the plasma. The magnetic field is produced with direct current. By varying this

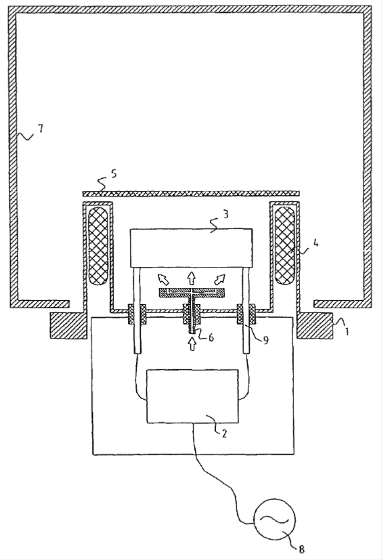

1 – mounting element
2 – high frequency matching network
3 – excitation electrode
4 – magnetic field coil
5 – beam extraction unit (grid)
6 – gas distribution system
7 – chamber wall
8 – high frequency power generator
9 – vacuum current feedthrough

Figure 1.11: Schematic view of the LEPEVPE RF plasma source [49].

field, resonance excitation of the plasma can be achieved. The source can be operated with or without an extraction unit, which consists of a grounded grid. The grid separates the chamber into two volumes: the one of the creation of the plasma and a second one where the plasma is expanding. As the Ga is evaporated outside the source volume (see figure (1.10)), the insertion of the grid between the plasma source and the wafer not only reduce the plasma density, but also modify the energy of the electrons, leading to a different interaction between the nitrogen and the Ga. The atomic flow coming out of the source with the extraction grid can be increased by varying the gas flow, and the dissociation can be increased up to 80% [50], which would be suitable for the deposition process. The radius of the grid is 9 cm and its thickness is 2.5 mm. It is perforated by holes of 8 mm in diameter, leading to an optical transparency of 27%.

The DC source used in this reactor is very similar to the one used in the LEP reactor. It consists of a cylindrical box, with a radius of $r = 7.5$ cm and a height of $h = 18$ cm, containing a tungsten filament, heated with an AC current of 150 A and an applied voltage V_{fil} of about 8 V. The DC plasma source is a Fronius DPS 400, connected to the anode (+) and the centre of one of the transformer coils (-). Contrary to the LEP device, the ignition of the plasma is made using argon, because it is easier to ionise than a molecular gas, and the desired gas composition is then set up. The replacement time of the gas is about 20 seconds. The position of the anode is shown in figure (1.12), and the electrical connections are the same as in figure (1.5). The anode can be made floating with respect to the reactor walls.

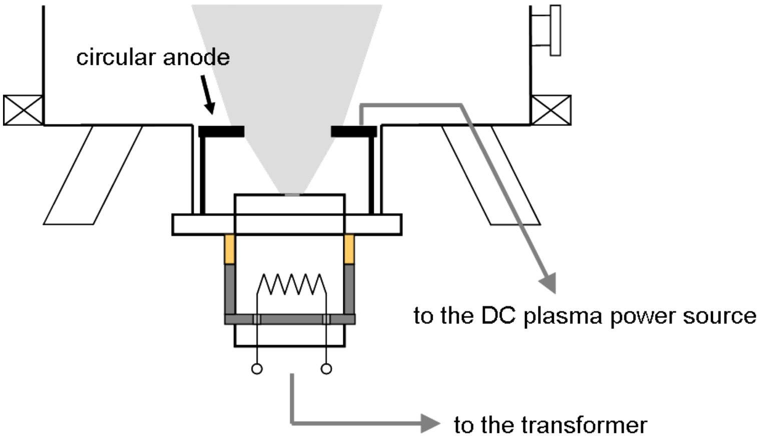

Figure 1.12: Scheme of the bottom of the LEPEVPE reactor with the DC source attached.

2 Diagnostics

In this chapter the different plasma diagnostics and film characterisation techniques are presented. Section 2.1 is dedicated to the plasma diagnostics used such as Langmuir probes and optical emission spectroscopy. Section 2.2 will describe the measurement techniques applied during the growth and section 2.3 introduces the methods used to analyse the deposited GaN layers. The main features of the diagnostics used in this work for the characterisation of the layers will only be briefly presented, as the focus of the thesis is on the plasma.

2.1 Plasma diagnostics

2.1.1 Langmuir probe

The most common *in situ* plasma diagnostic is the Langmuir probe, first introduced by Mott-Smith and Langmuir in 1926 [51]. It consists of immersing a piece of metal into the plasma and observing the current it draws when it is biased against ground. The advantage of such a Langmuir probe is the simple handling. The probe can be used to extract the electron temperature, the floating and plasma potentials and the ion and electron densities. In contrast to the simple experimental requirements, the analysis of the resulting current-voltage (I-V) characteristics of the probe can be quite complex.

In this work a single Langmuir probe has been used, and its schematics is shown in figure (2.1). The pin is made of a piece of tungsten wire (cylindrical shape), with a length of 2.3 mm and a diameter of 1 mm. The tip is in contact with the plasma and the rest of the wire is insulated from the plasma by a ceramic tube (see figure (2.1)), and the assembly is mounted on a movable rail permitting to move the probe over a distance of 20 cm. The pin is biased using a set of batteries to −27 V, or a voltage generator is used, allowing to sweep the voltage between −100 and +100 V. To prevent coating on the probe tip, the Langmuir probe was not used during Ga-N_2 plasmas.

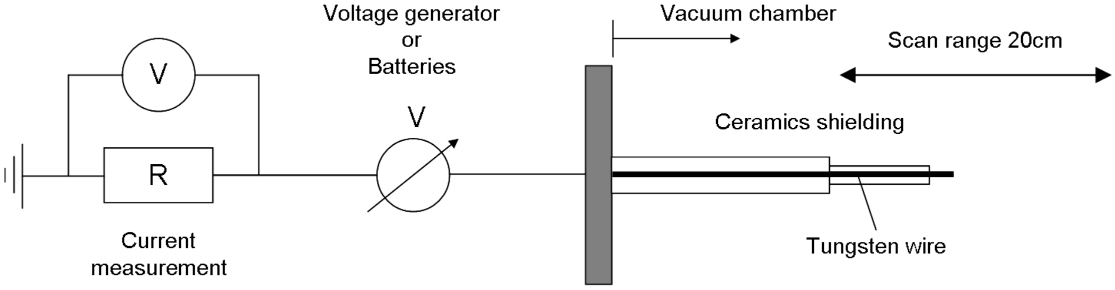

Figure 2.1: Schematics of the single pin Langmuir probe.

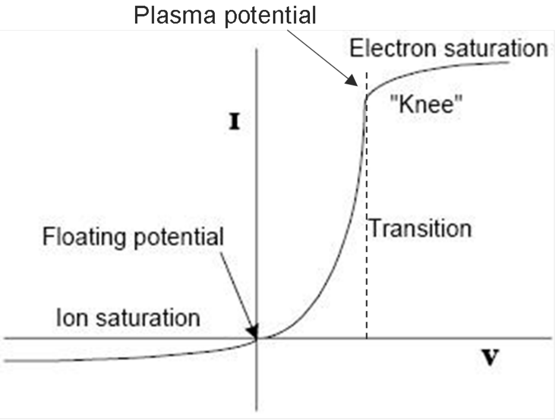

Figure 2.2: Typical single pin Langmuir probe I-V characteristic [52].

A typical I-V characteristic of a single pin Langmuir probe is shown in figure (2.2). From this kind of current-voltage curve, the plasma parameters quoted above can be obtained [52,53]. The point at which the curve crosses the V-axis is the floating potential, V_f, the voltage where no net current is drawn by the probe ($\mathrm{I_{probe}} = 0$ A). This voltage is generally not at $V = 0$ V, as in the figure. To the left of this point, the probe draws an ion current, reaching at very negative voltage saturation, the ion saturation current $I_{i,sat}$. To the right of V_f, the probe draws an electron current, and the curve shows an exponential part, also called transition region. Increasing the bias voltage to the plasma potential V_p, the ideal curve takes a sharp turn, called "knee". Electron saturation current ($\mathrm{I}_{e,sat}$) is reached by increasing the voltage.

The electron temperature T_e can be obtained by plotting $\ln(I)$ as a function of V [52], in the transition region. Assuming a Maxwellian electron distribution, the electron current can be described by

$$I_e = \underbrace{en_eA\sqrt{\frac{k_BT_e}{2\pi m_e}}}_{I_{e,sat}} \cdot \exp\left[\frac{e(V-V_p)}{k_BT_e[\mathrm{K}]}\right] = I_{e,sat} \cdot \exp\left[\frac{V-V_p}{T_e[\mathrm{eV}]}\right] \tag{2.1}$$

where e is the elementary charge, n_e the electron density, A the surface of the probe tip, k_B the Boltzmann constant, T_e the electron temperature in K or eV, and m_e the electron mass. The slope of $\ln(I)$-V plot is therefore $1/T_e$, with T_e in eV.

At $V = V_p$ the probe current is equal to the electron saturation current. This voltage corresponds to the plasma potential. This potential is more positive than the most positive voltage in the reactor, to confine the electrons in the plasma. In fact, the electric field created in this way repulses the electrons from the walls. From the electron saturation current the plasma density can be determined, knowing the electron temperature (see equation (2.1)). Unfortunately the "knee" in the experimental I-V curve is generally not as clear as on figure (2.2). To determine the plasma density, the ion saturation current $I_{i,sat}$ is preferred, because $\mathrm{I}_{i,sat} \ll \mathrm{I}_{e,sat}$ and because of the indistinct knee at the plasma potential. The plasma density is linked to the ion saturation current through the Bohm sheath criterion:

$$I_{i,sat} = 0.61 eAn\sqrt{\frac{eT_e}{M}} \tag{2.2}$$

where M is the atomic mass of the gas used and T_e expressed in eV. The ion saturation current is measured with a very negative bias on the probe, to repel all the electrons.

At the floating potential V_f, the net current is null, i.e. $I_i = I_e$. Equating equations (2.1) and (2.2) with $V = V_f$ yields an approximation of T_e

$$V_f - V_p = -\frac{k_B T_e}{2e}\ln\left(\frac{2M}{\pi m_e}\right) \tag{2.3}$$

The value $V_p - V_f$ is about 5.2 T_e for nitrogen. The study of the variation of the floating potential in the reactor can lead to an estimation of the direct variation of T_e, assuming V_p constant. The floating potential is very sensitive to fast electrons, and can be determined by measuring the voltage of the probe set into the plasma without bias using a high impedance voltage measurement device, such as a voltmeter or an oscilloscope.

Figure (2.3) shows a Langmuir I-V curve obtained with the RF plasma source with the grid in the deposition reactor. On this figure the entire I-V curve is seen in *(a)* and in *(b)* it is shown in logarithm scale. The ion saturation current can be determined at negative voltages. The inset in *(a)* illustrates the floating potential determination, the bias voltage when the curve passes at zero current. The "knee" at the plasma potential is not as distinct as in figure (2.2). To obtain the plasma potential of such a I-V curve, it is drawn on logarithmic scale. The plasma potential is taken at the crossing point of two lines: the one from the transition region and the other from the electron saturation current.

The transition region of the I-V curve is the straight line between $0-10$ V, as predicted for a Maxwellian distribution. This indicates that in this particular case, the EEDF is

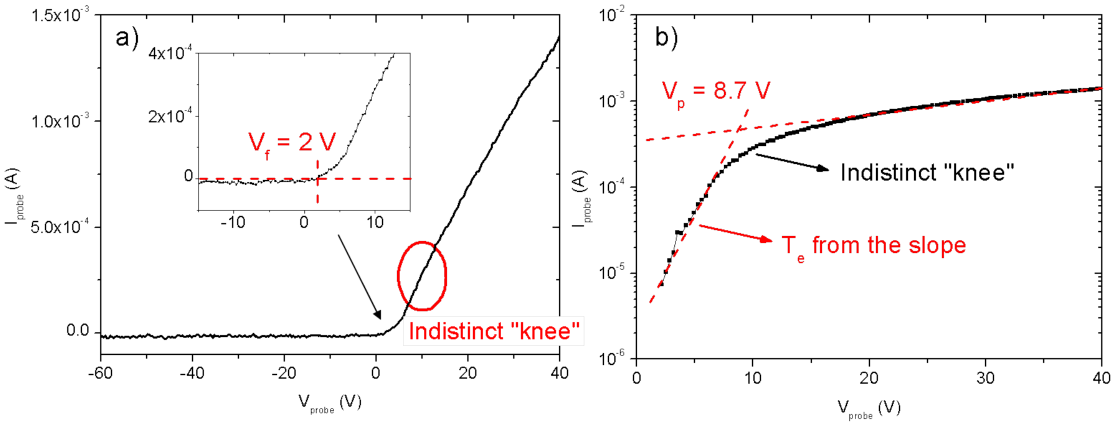

Figure 2.3: Experimental Langmuir probe signal obtained with the RF plasma source with grid in the deposition reactor: *(a)* full I-V curve, with the inset showing the floating potential, and *(b)* logarithmic plot of the electron current region.

near to a Maxwellian distribution, at a temperature that can be determined from the inverse of the slope in the logarithm plot. This type of EEDF has only one parameter, the electron temperature. From the I-V curve presented, an estimation of the EEDF can be obtained.

With the DC plasma source the electrons created by thermionic production are accelerated by the potential difference between the filament and the anode. This electric field leads to the creation of an electron beam penetrating the chamber visible as plasma plume. A large part of these fast electrons will be lost by collision but a part of these primary electrons can survive due to the low pressure and reach the measurement point. These fast electrons form a beam, a situation described by Hershkowitz in [54]. The probe current due to these primary electrons is given by [54]

$$\begin{aligned} I &= I_p^* \equiv \frac{n_p e A v_p}{4}, & V > V_p \\ &= I_p^* \left(1 - \frac{e\left(V_p - V\right)}{E_b}\right), & V_p - \frac{E_b}{e} \leq V \leq V_p \\ &= 0, & V < V_p - \frac{E_b}{e} \end{aligned} \tag{2.4}$$

where I_p^* is defined as the primary electrons saturation current, n_p is the density of the primary electrons and $v_p = \sqrt{2E_b/m_e}$ the velocity of the primary electrons, V the probe bias and V_p the plasma potential.

With this kind of I-V curve, T_e and n_e from the bulk plasma electrons can be approximately obtained by first subtracting the current due to these primary electrons. As seen in equation (2.4), the current from the primary electrons exhibits a linear increase with the probe bias between $V_p - \frac{E_b}{e}$ and V_p. The saturation current of this electron beam is determined at V_p, by continuing the linear part with a straight line (see figure (2.4a)). This procedure is however subject to error, because it is difficult to estimate the tail of the bulk Maxwellian. With both I_p^* and E_b, the density of the beam electrons can be determined. The proportion of primary electrons compared to the total electron density is typically between $2-3\%$.

Figure (2.4) presents an I-V curve of the Langmuir probe in a DC plasma. The I-V curve is again shown in *(a)* in linear scale and in *(b)* in logarithm scale, to highlight the beam electrons current. The inset in *(a)* shows the part coming from the primary electrons and the determination of I_p^*, the saturation current of the primary electrons. On the logarithm scale the current coming from the beam electrons is more in evidence. In fact if the EEDF would have been a pure Maxwellian, the electron current in the region -5 to 5 V would have decreased with the same slope, indicated by the dashed red curve in figure (2.4b). The presence of the electron beam increases the electron current to the probe at negative voltages, and as a consequence lowers the floating potential. In this particular case the floating potential is at about -30 V. This means that to repulse all the electrons of the plasma a surface should be polarised at this potential. With this plasma source, the EEDF is more complex: two parameters are needed to determine the EEDF. The transition region permits to extract the electron temperature of the bulk Maxwellian part, and the slope of the linear part gives the indication of the electron beam energy. The energy width of the distribution cannot be determined experimentally with sufficient accuracy with this method.

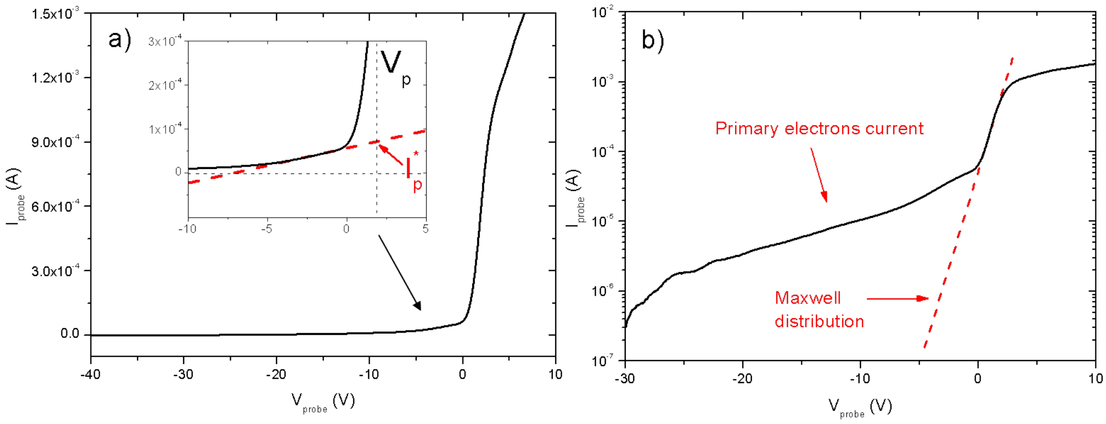

Figure 2.4: Experimental Langmuir probe signal obtained with the DC plasma source: *(a)* full I-V curve, with the inset showing the primary electrons current, and *(b)* logarithm of the electron current region.

2.1.2 Optical emission spectroscopy

The second plasma diagnostic used to analyse the plasma is the optical emission spectroscopy (OES). The collection of the light coming out of the plasma can be used to determine the plasma composition. The spectrometer used was an Ocean Optics PlasCalc 2000. In figure (2.5) the schematics of the measurement setup is shown. Several viewports on both reactors could be used to monitor the light coming out of the plasma. The aperture angle of the fibre is about 4°. The optical fibre is then connected to the spectrometer, which has a spectral range of $200-1200$ nm and a resolution of 1 nm. The signal is treated with the *PlasCalc* software (MikroPack PlasCalc v. 2.3). The software can monitor the spectrum in time, showing that the plasma is stable within 3%.

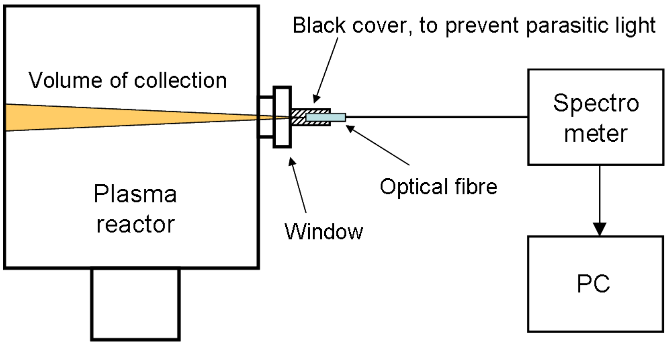

Figure 2.5: Schematics of the optical emission spectroscopy (OES) measurement.

Several phenomena can alter the signal: attenuation in the optical fibre, transmission coefficient of the window or response of the CCD camera in the spectrometer are some examples. To take into account these factors, a relative calibration of the wavelengths has been done using a white lamp (*LabSphere*) with a known spectrum. The spectrum of the lamp was recorded by the fibre through the different windows of the reactor, and the obtained spectra were compared to the calibrated spectrum of the lamp. The ratio between both spectra gives a calibration factor for each wavelength, and takes into account all phenomena which alter the optical signal. Because deposition was made in the LEPEVPE reactor, the windows were located at the end of a tube, so that the radicals deposit on the tube before reaching the window. Additionally the windows were equipped with a shutter to prevent direct coating on windows. After some hours of deposition, the most used windows were replaced by cleaned ones, which were previously calibrated with the white lamp.

To collect only the light emitted by the plasma, a background acquisition was made before any OES measurement. Internal reflections on the walls or on the tube in front of the windows during a plasma are not cancelled by this procedure, but the intensities of these reflections are supposed to be negligible and their effect small compared to the plasma emission intensity. The plasma intensity depends on the plasma conditions, thus the integration time has been chosen not to saturate the detector. The background

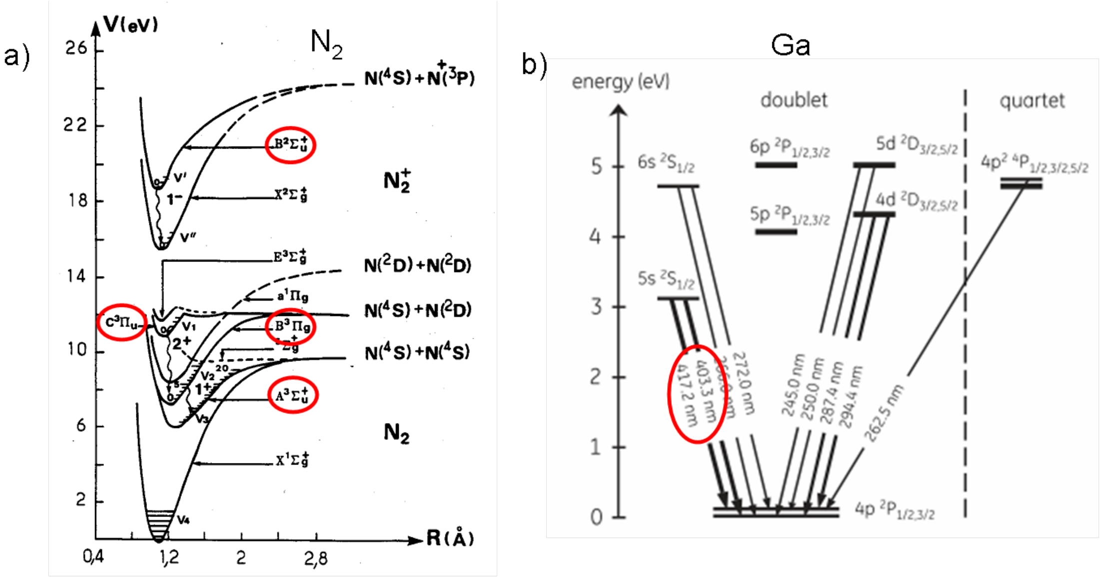

Figure 2.6: *(a)* Energy diagram of the nitrogen molecule and *(b)* Grotrian diagram of gallium, respectively taken from [55] and [56].

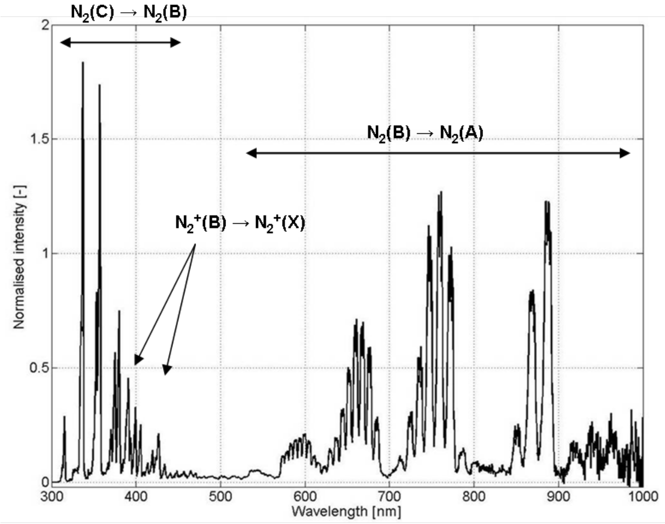

Figure 2.7: Example of a nitrogen spectrum obtained in the deposition reactor.

intensities were measured for each integration time and fibre position.

Nitrogen is a diatomic molecule, thus having several excitation modes: electronic, vibrational and rotational. Electronic excitation is a change in the electronic energy levels, according to the energy level pattern shown in figure (2.6). The changes in the electronic level are generally accompanied by a change in the vibrational level according to the Frank-Condon principle [57–59]. Vibrations are relative motions of the atomic nuclei composing the molecule, whereas rotations are collective motions of all the atomic nuclei of the molecule. The two latter are sub-levels of the electronic states. The de-excitation from a selected state leads to a specific photon of the exact energy between the two states. The de-excitation from a ro-vibrational state leads to many different wavelengths, thus creating the bands seen in figure (2.7). The transition probability between two states is called the Einstein coefficient of spontaneous emission [60], and can be found in literature, such as in [59].

Figure (2.6) presents the energy diagram of the nitrogen molecule, with (highlighted with red circles) the main electronic states of the neutral molecule N_2(A), N_2(B) and N_2(C), and the radiative electronic state of the molecular ion N_2^+(B). The figure shows also the Grotrian diagram of the gallium, with the highlighted emission lines which can be observed through the windows of the reactors. Other Ga emission lines are at too low wavelengths, thus absorbed by the windows. The three main electronic levels have different energies: N_2(A) 7.65 eV (metastable), N_2(B) 8.55 eV and N_2(C) 11.03 eV; and at higher energy the molecule is ionised (15.6 eV (ground ion) or 19 eV (excited ion)). As it is a molecule, energy can also be deposited into vibration and rotation of the two N atoms. These processes are of lower energy, typically $1-2$ eV. Each electronic states has ro-vibrational states. The energy for the dissociation of the neutral ground state molecule is 9.8 eV (figure (2.6)).

The composition of the plasma can be estimated from the OES spectrum. In fact the excited species emit light, depending on their excitation level. Three distinct regions can be drawn on a typical spectrum (figure (2.7)), the three major nitrogen components: first positive system (FPS), from 550 nm to 1000 nm, corresponding to the de-excitation of the N_2(B) into the N_2(A) state. The second positive system (SPS) is the region from 300 nm to 400 nm, corresponding to the de-excitation from the N_2(C) into the N_2(B) state. Finally there is the first negative system (FNS) from the molecular ion (N_2^+(B)→N_2^+(X)), corresponding to bands around 400 nm (main band head at 391 nm). The spectrum divides itself into bands for the molecular excitations, whereas the atoms (N and Ga) emit light at specific wavelengths, leading to emission lines.

The emitted light intensity can be linked to the density of the excited states through a simple relationship [40, 42, 61]:

$$I = C \cdot n \cdot A \tag{2.5}$$

where I is the intensity of the emitted wavelength, C a constant including the spectral response of the spectrometer, A the Einstein coefficient for spontaneous emission of the transition, and n the excited state density. From the above description of the different wavelengths regimes, the sum of all the transitions from the first positive system gives an indication of the electronic state denstiy N_2(B). The same can be made for the second positive system (N_2(C)). The sum of the Einstein coefficients is the inverse of the radiative lifetime of the excited state, which can be found in literature [59]. To cancel the constant

C in equation (2.5), the ratio $N_2(C)/N_2(B)$ is calculated, as proposed by Zhu *et al.* [42]. The evolution of the ratio indicates a change in the energy of the electrons. The ratio of the density can be compared with the one found with models.

2.2 *In situ* crystal growth diagnostics

To characterise the growth rate and the morphology of the deposited layer mainly two diagnostic techniques are used.

2.2.1 Laser reflectometry

Laser reflectometry is a commonly used technique to estimate the growth rate of thin film semi-conductor layers and their roughness variation with time [62–64]. The setup of this measurement technique consists of a red laser diode with a wavelength of $\lambda = 650$ nm and a Si photodiode, detecting the laser beam reflected from the sample. The detector is equipped with a $640-660$ nm bandpass filter to block the plasma ambient light and to attenuate the radiation coming from the substrate heater. The signal of the photodiode is then amplified and finally digitised. In order to cancel out any straylight effects, a dark measurement (the laser source turned off) is subtracted from the signal.

The working principle of this technique is to analyse the reflected signal from the growing layer, based on the interferences from parallel surfaces, whose thickness increases with time (see figure (2.8)). The different reflected rays will interfere, because there are many internal reflections in the growing layer. The detected signal will then oscillate as a function of the thickness of the grown layer. The amplitude and the periodicity of the oscillations are depending on the physical parameters of the growing layer and of the substrate.

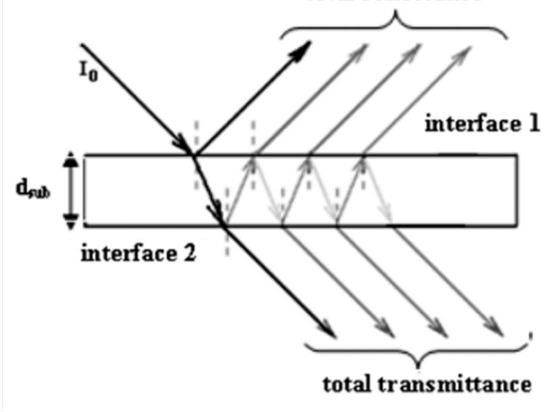

Figure 2.8: Schematic plot of multiple reflections and transmissions in a slab geometry [65].

The periodicity of the intensity oscillations can be used to estimate the growth rate, using the following formula [62]

$$v_g = \frac{\lambda \cos(\theta)}{2nT} \tag{2.6}$$

where λ is the wavelength of the laser, θ the angle with respect to the normal direction of the surface, n the refractive index of the GaN of 2.37 [63] and T the period of the reflections oscillations. The maximum of the amplitude is then an integer multiple of $\frac{\lambda \cos(\theta)}{2n}$, which is about $0.16\,\mu$m in the case of GaN growth.

The amplitude of the fringes gives an indication on the roughness of the surface. A bidirectional growth leads to constant oscillation amplitude, whereas a tridimensional one leads to a decreasing mean value of the signal, because the diffraction is increased, as it can be seen on figure (2.9), presenting an experimental curve obtained with the RF plasma source.

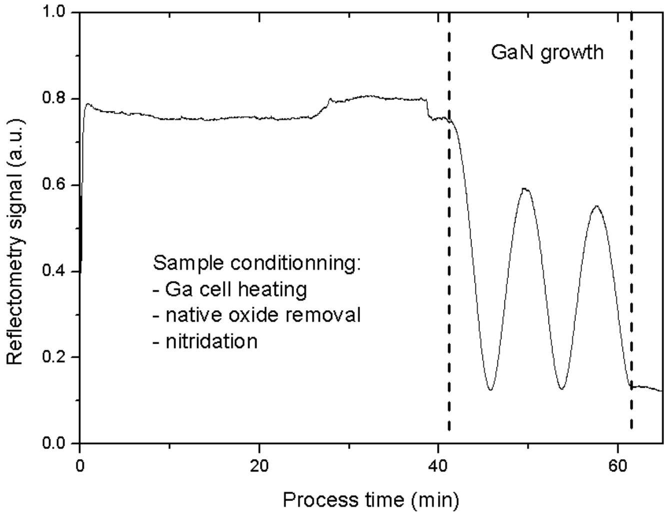

Figure 2.9: Experimental reflectometry curve, showing the oscillation of the signal during the growth and the decrease of the amplitude, due to an increasing roughness of the surface.

2.2.2 RHEED pattern

Another *in situ* technique to characterise the growth of thin films is the RHEED, which is used in this work for the surface analysis and well described in the literature [66–68]. A RHEED system consists of an electron source (gun) and an electroluminescent detector screen. The electron gun (NEK 150 from Staib Instruments) generates a beam of electrons which strikes the sample at a very small angle relative to the sample surface ($\theta \approx 3°$). Figure (2.10) shows the setup of the RHEED system used.

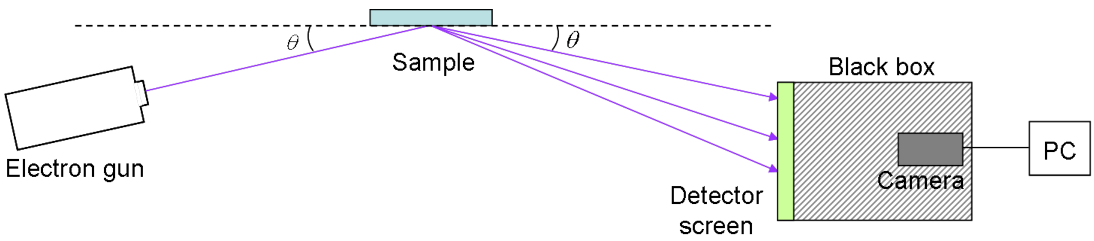

Figure 2.10: RHEED setup used in this work.

Incident electrons diffract from atoms at the surface of the sample, and a fraction of the diffracted electrons interfere constructively at specific angles and form regular patterns on the detector [69]. The electrons interfere according to the position of atoms on the sample surface, so the diffraction pattern at the detector is a picture of the sample surface [66], see also figures (2.11) and (2.12).

The glancing angle of incident electrons allows them to escape the bulk of the sample and to reach the detector. Atoms at the sample surface diffract (scatter) the incident electrons due to the wavelike properties of electrons. The diffracted electrons interfere constructively at specific angles according to the crystal structure and spacing of the atoms at the sample surface and the wavelength of the incident electrons. Some of the electron waves created by constructive interference arrive to the detector, creating specific diffraction patterns according to the surface features of the sample. It is possible to characterise the crystallography of the sample surface through analysis of the diffraction patterns.

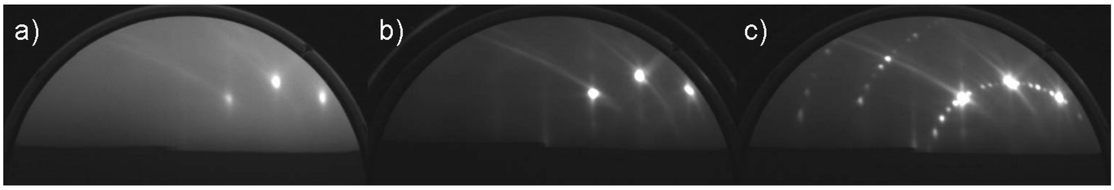

Figure 2.11: RHEED observations of the sample during a degasing *(a)* at 600°C, *(b)* 1000°C and *(c)* during the cooling down which allows to see the 7*x*7 transition.

In this work the RHEED system has been used to check the cleanliness of the sample before the growths, by detecting the so called 7*x*7 transition of the silicon wafers after heat treatment removing the oxide layer (figure (2.11)). The 7*x*7 reconstruction of the Si(111) is obtained by annealing a clean surface [70]. The atoms of the surface rearrange themselves into a larger and more stable cell, if the surface is clean, and assume a different structure than that of the bulk. The 7*x*7 unit cell is the most stable reconstruction pattern, whose unit cell is 49 times larger than a standard, unreconstructed 1*x*1 unit cell. It can be detected by the apparition of many dots on the RHEED pattern, as on figure (2.11). The first reconstruction process was observed by Schlier and Farnsworth in 1959 [71].

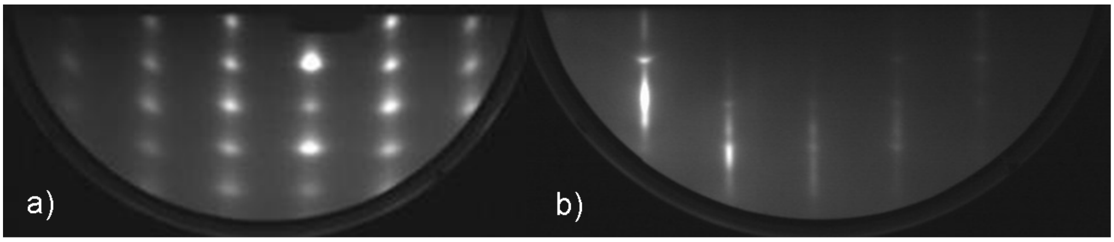

Figure 2.12: RHEED patterns obtained in this work, showing *(a)* 3D structure at the surface and *(b)* 2D structure.

RHEED patterns shown in figure (2.12) have been used to check the morphology of the surface. In fact, in a first approximation, a pattern showing an array of spots as in figure (2.12a) indicates a 3D surface, whereas an array of lines indicates a 2D surface (figure (2.12b)) [72].

The RHEED system can also be used to estimate the growth rate, by analysing the intensity oscillations of the specular spot (greatest intensity spot on a RHEED pattern). A period of oscillation corresponds to a thickness variation of one mono-layer. However, the RHEED must operate at a pressure low enough to prevent significant scattering of the electron beams by gas molecules in the chamber. The pressure limits the types of materials and processes that can be monitored *in situ* with RHEED. For this reason the RHEED could not be used during the growth in a continuous mode, because the pressure in the chamber was about $5 \cdot 10^{-3}$ mbar, too high for the operation of the RHEED. The use of magnetic field with the DC plasma source, to increase the plasma density, also limits the use of the RHEED, because the intensity of the field deviates the electrons out of the sample and/or of the detector. The RHEED pattern was thus only used to estimate the surface cleanliness and morphology, as a qualitative indicator.

2.3 *Ex situ* layers diagnostics

After the deposition process the film can be characterised by different *ex situ* methods. In this work mainly: scanning electron microscopy (SEM) and X-ray diffraction (XRD) were used.

2.3.1 Scanning electron microscope

A scanning electron microscope (SEM) is an electron microscope that produces images of a sample by scanning it with a focused beam of electrons. The electrons interact with atoms in the sample, producing various signals (emission of secondary electrons, back scattering of electrons, ...) that can be detected and that contain information about the sample's surface topography and composition [73, 74].

When the primary electron beam interacts with the sample, the electrons lose energy by repeated random scattering and absorption within a teardrop-shaped volume of the sample known as the interaction volume, which extends from less than 100 nm to around 5 μm into the surface. The size of the interaction volume depends on the electron's energy, the atomic number of the surface's atoms and its density. The energy exchange between the electron beam and the sample results in the reflection of high-energy electrons by elastic scattering, emission of secondary electrons by inelastic scattering and the emission of electromagnetic radiation. Electronic amplifiers of various types are used to increase the signals, which are displayed as variations in brightness on a monitor. Each pixel is synchronized with the position of the beam on the sample in the microscope, and the resulting image is therefore a distribution map of the intensity of the signal being emitted from the scanned area of the sample. Figure (2.13) shows examples of images produced by a SEM.

The electron beam is generally scanned in a raster scan pattern, and the beam's position is combined with the detected signal to produce an image. The resolution of the used SEM (Jeol JSM-6701F) can be as low as 2.2 nm, with an accelerating voltage of 1 kV. Due to the very narrow electron beam, SEM micrographs have a large depth of field yielding a characteristic three-dimensional appearance useful for understanding the surface structure of a sample. A wide range of magnifications is possible, from about 25 times to more than $650'000$ times.

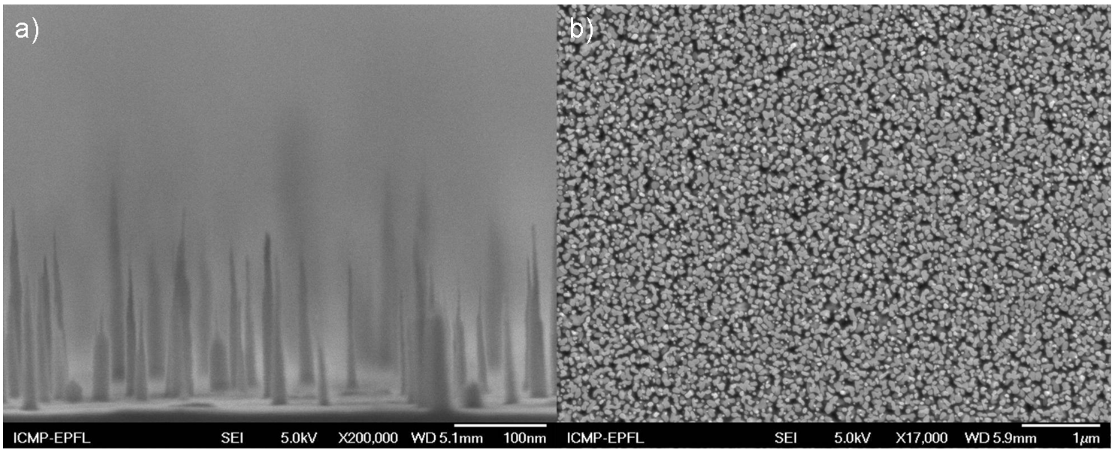

Figure 2.13: SEM picture from *(a)* the side and *(b)* the top of a sample, indicating the topography of the surface: nanocolumns in both cases.

2.3.2 X-ray diffraction

The other *ex situ* diagnostic used in the framework of this thesis is the X-ray diffraction (XRD). XRD is a set of measurements used to get information about the crystalline structure, the composition, the strain or the quality of solid or powder crystals, including semiconductors [75–77].

Diffraction occurs when incoming waves interact with a regular structure, which exhibits a repeat distance of about the wavelength length. X-rays can have wavelengths of the order of a few angstroms, typical interatomic distances in crystalline solids, meaning that X-rays can be diffracted from crystals. When certain geometric requirements are met, X-rays scattered from a crystalline solid can interfere constructively, producing an intense reflected beam. The Bragg law gives the angles for coherent and incoherent scattering from a crystal lattice following the relationship

$$n \cdot \lambda = 2d \sin\theta \tag{2.7}$$

where d is the distance between atomic planes, λ the wavelength of the incident X-ray, θ (also noted ω in the literature) is the angle of incidence (and diffraction) and n an integer (see figure (2.14)). Knowing the incident X-ray wavelength and all the angles of constructive interferences, it is possible to deduce the complete crystalline structure and all the lattice parameters of the target and from there determine the nature of the material [75, 78].

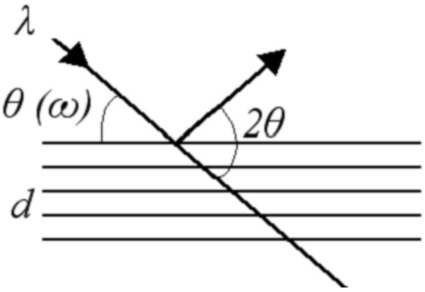

Figure 2.14: Diffraction of X-rays on atomic planes.

In the XRD system used, the sample is mounted on a four-circle (ω, 2θ, χ, ϕ) rotating stage. ω and 2θ are the incident and diffraction angles, respectively. χ is defined as the angle between the sample surface and the horizontal plane, which is defined by the incident and diffraction lines. The angle ϕ measures the rotation around the surface normal of the substrate. In this work, XRD is used to measure the distance between atomic planes. The method consists of an omega/2-theta angle scan of all the constructive diffraction peaks. Each structural defect or dislocation creates a local misorientation of the atomic planes, leading to a slight alteration of the local diffraction mechanisms. Consequently, the full-width at half maximum (FWHM) of the diffracted peak gives a qualitative indication about the defect concentration in the crystal. The measurement consists of an omega scan (rocking curve) while the detection angle 2-theta is fixed. Figure (2.15) shows two patterns of XRD measurements on a GaN sample prepared with MOCVD [79], and one prepared in our system with the RF plasma source. The difference of FWHM highlights the poor crystallinity of our sample.

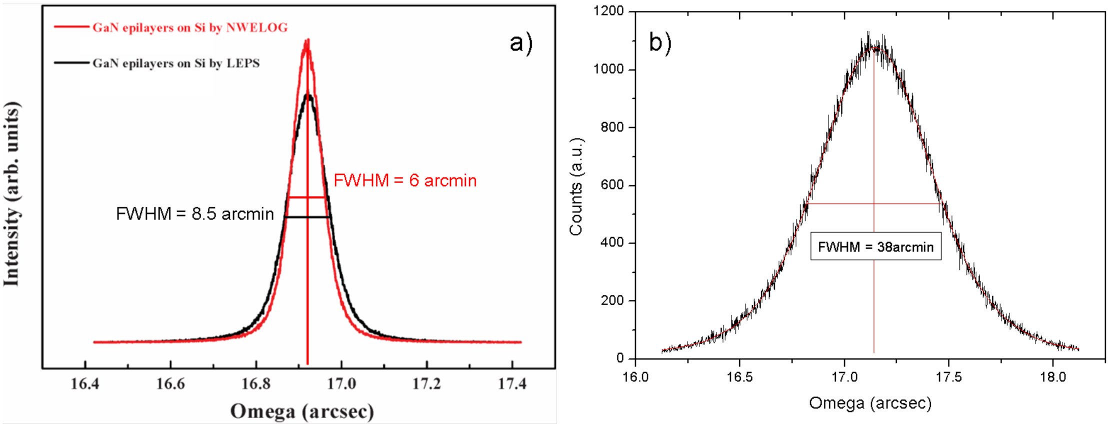

Figure 2.15: Rocking curve of GaN grown on Si(111) by *(a)* MOCVD [79], and *(b)* in our system.

3 Nitrogen plasma modelling

In this chapter three models of the nitrogen plasmas will be presented. Modelling is a powerful tool to understand the physics occurring in the process plasma. In a first approximation it can also show the trends to be expected when changing some input plasma parameters. The three models are the following: a particle balance model as proposed by Lieberman [53], originally used for argon which has been adapted for nitrogen, a corona model to compare the excited states densities with the measured ones, and finally a collisional-radiative model (0 dimensional) where balance equations are solved to find the excited states and non-radiative states densities.

3.1 Electron energy distribution functions and reaction rates

The electrons of the plasma with an energy distribution interact with the neutral gas through collisions. The number of reactions is determined by the reaction rates, which can be mathematically calculated as follow, with ε being the energy :

$$k_i = \int_0^\infty \sigma_i(\varepsilon)\, f(\varepsilon)\, \varepsilon \sqrt{\frac{2e}{m_e}} \mathrm{d}\varepsilon \tag{3.1}$$

where $\sigma_i(\varepsilon)$ is the cross section of the collision type i (excitation, ionisation, ...), $f(\varepsilon)$ is the electron energy distribution function (EEDF) with $\int f(\varepsilon)\mathrm{d}\varepsilon = 1$, e is the elementary charge and m_e is the electron mass.

Figure (3.1) presents a graphical representation of the reaction rate: the overlap of the EEDF and the cross section. From this picture, it can be seen that the EEDF plays an important role in the determination of the reaction rates, by varying the area of the overlap, and is thus the key point for the processing plasmas. The cross sections are fixed, thus in order to vary the reaction rates, the EEDF needs to be changed, which can be performed by a change of the plasma source or by variation of the external process parameters, such as the gas pressure or the electric power. Some reactions can be favoured with different EEDFs, because of differences in shape and threshold energies of the cross sections.

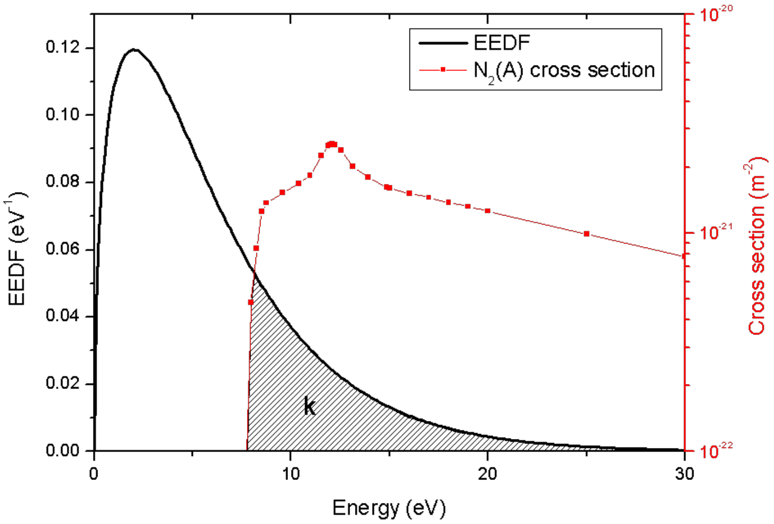

Figure 3.1: Graphical representation of the reaction rate: overlap of the EEDF and the cross section of a collision.

The cross sections of the collisions with electrons are found in literature, for example in [80–82] for nitrogen and in [83] for gallium. They are presented in figures (3.2) and (3.3) respectively. The different authors present the cross sections for the same processes, but the values can vary up to a factor of 3, leading to large error bars on the curves. For convenience, only the ones for the N_2(A) state excitation are shown. In this work, the cross section values of the most recent articles found have been chosen for each reaction. Another observation on the cross sections is that the threshold energies for the cross sections are different, according to the energy diagram shown in figure (2.6), with ionisation processes requiring a higher energy to occur. The maximum values for the excitation differ for each state. The order of magnitude of the cross section is the same for the different electronic states, and the shape of the curve is about the same also. The ionisation into the ground state molecular ion is the dominant cross section for electrons above 20 eV.

The gallium cross sections have a different shape than the ones for nitrogen. In fact they are more flat and the threshold energies are much lower. The order of magnitude of the gallium cross sections is higher than the one for the nitrogen, indicating that the reactions with gallium will be favoured if the densities of both species are equivalent.

As mentioned in section 2.1.1, there are two types of EEDF found in our experiments: a pure Maxwell distribution and a Maxwell distribution with an electron beam superimposed.

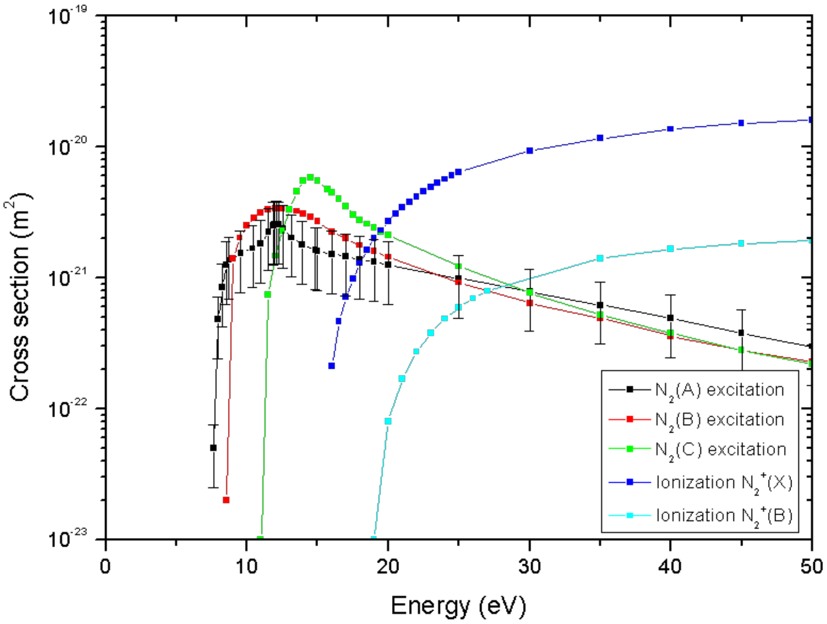

Figure 3.2: Cross sections of processes in nitrogen, from the ground neutral molecule: excitation of the electronic states and ionisation into molecular ion at ground state and excited state [80–82]. The error bars on the other curves are not shown for convenience.

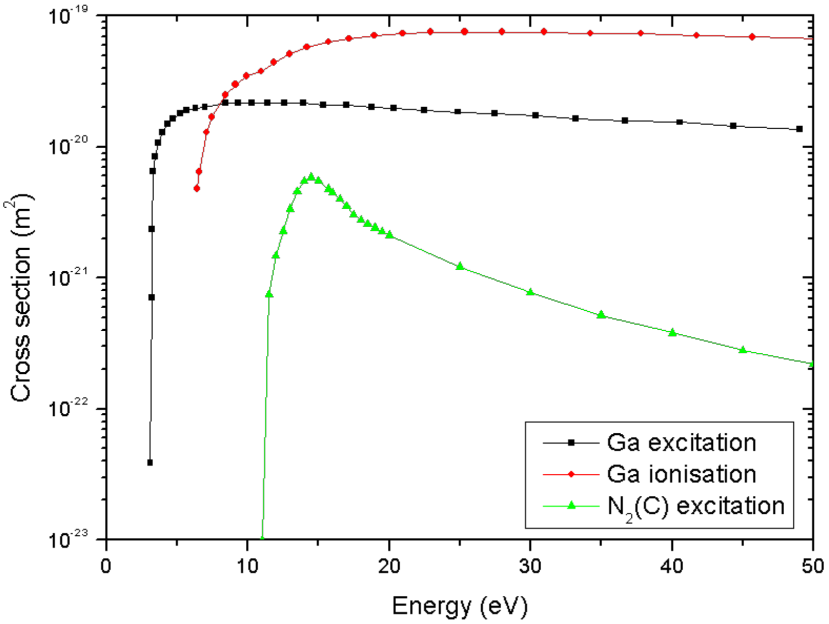

Figure 3.3: Gallium excitation and ionisation cross sections from the ground neutral atom, and comparison with the nitrogen N_2(C) cross section [83].

The Maxwell-Boltzmann energy distribution function is given by [84, 85]

$$f(\varepsilon) = 2\sqrt{\frac{1}{\pi}}\left(\frac{1}{T}\right)^{3/2}\sqrt{\varepsilon}\exp\left[-\frac{\varepsilon}{T}\right] \tag{3.2}$$

where T is the temperature of the distribution in eV and ε the energy in eV.

Figure (3.4) shows the Maxwell EEDF as a function of the energy with an increasing temperature in linear and logarithm scale. As the temperature increases, the maximum of the distribution shifts to higher values of energy, as does the mean value of the distribution. As seen on the logarithm scale, the proportion of electrons having an energy above 10 eV increases rapidly with the temperature. This means that the temperature plays a central role in the chemistry occurring in a plasma, because only a small proportion of electrons have sufficient energy to undergo high energy reactions, such as ionisation or dissociation.

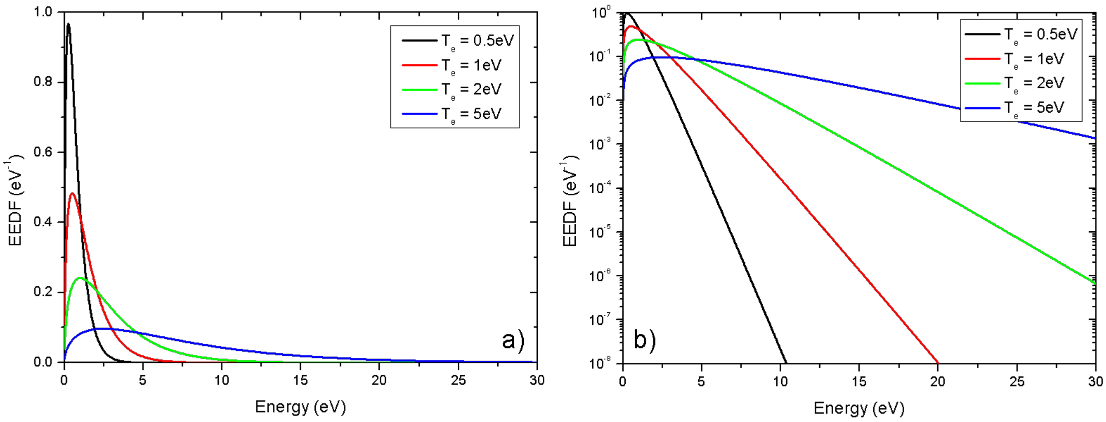

Figure 3.4: Maxwell EEDF at different electron temperatures, viewed in *(a)* linear and *(b)* logarithm scale.

The second type of distribution found in our experiment is a Maxwell distribution with an electron beam superimposed. As already mentioned (chapter 2), the proportion of primary electrons remaining in the measurement zone is between 2 and 3% of the total electron density, thus for all the caluclations in the modelling, it has been fixed at $p = 2.5\%$. The distribution function has the form

$$f(\varepsilon) = (1-p) \times 2\sqrt{\frac{1}{\pi}}\left(\frac{1}{T}\right)^{3/2}\sqrt{\varepsilon}\exp\left[-\frac{\varepsilon}{T}\right] + p \times \sqrt{\frac{2}{\pi}}\frac{1}{2\omega}\exp\left[-\frac{(\varepsilon - E_b)^2}{2\omega^2}\right] \tag{3.3}$$

where p is the proportion of primary electrons compared to the total electron density, ω the energy width of the Gaussian beam and E_b the mean energy of the electron beam. As mentioned before, the energy width of the electron beam could not be determined experimentally precisely, thus it has been fixed at $\omega = 1.5$ eV.

Figure (3.5) shows the beam-Maxwell EEDF, with a varying electron temperature of the Maxwellian part of the distribution and with a varying electron beam energy. Both charts are presented in logarithm scale, to better see the effect of the different parameters. The increase of temperature of the bulk Maxwellian part leads to a decrease of the effect of the electron beam, which tends to disappear in the Maxwellian high energy tail of the distribution. The electron beam can locally increase the proportion of electrons at this energy range, which could increase the reaction rate of a specific reaction.

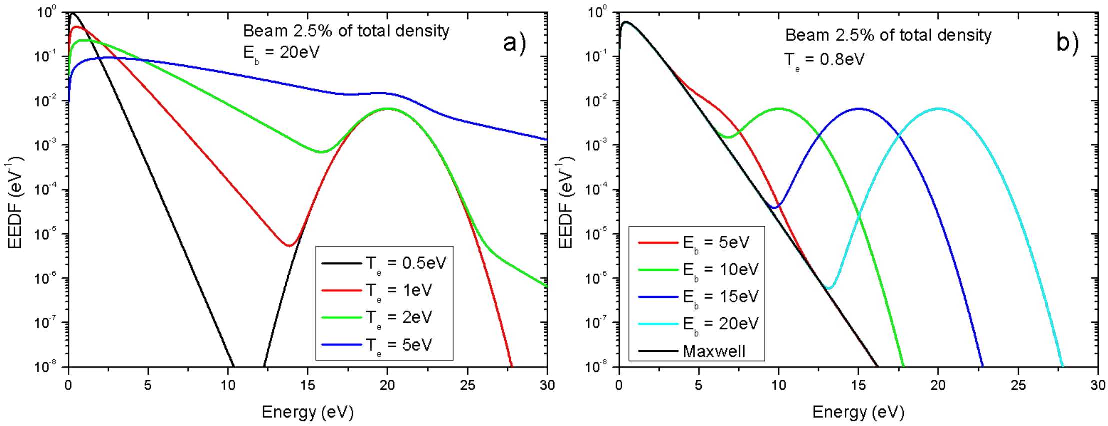

Figure 3.5: Maxwell with electron beam EEDF *(a)* with a fixed beam energy at different electron temperatures and *(b)* with a fixed T_e and different beam energies.

Figure (3.6) presents two calculated reaction rates as a function of the electron temperature of the Maxwellian, and for different beam energies. The part *(a)* shows the behaviour of the excitation reaction into the metastable N_2(A) from the ground state : $e{+}N_2(X) \rightarrow e{+}N_2(A)$. The threshold of this reaction is at 7.65 eV [80]. The curve with a pure Maxwell EEDF (in black) shows a global increase with the electron temperature, with a beginning of saturation above about $T_e = 3$ eV. The electron beam greatly influences the reaction rates and tends to flatten them at low electron temperatures.

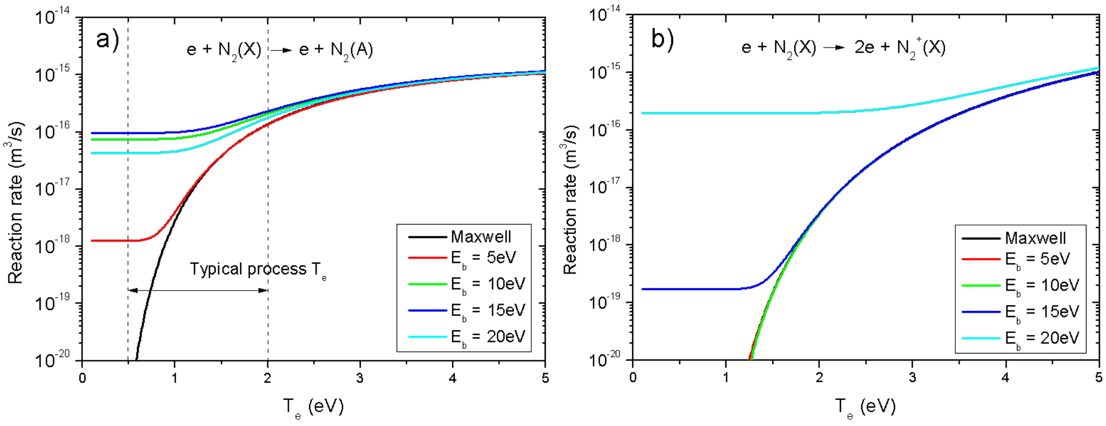

Figure 3.6: Reaction rates as a function of the electron temperature with pure Maxwell distribution and beam-Maxwell distributions with different beam energies of *(a)* N_2(A) excitation from ground state and *(b)* ionisation from ground state. Electron beam proportion is 2.5% of the total electron density.

At these low T_e, the excitation is only due to the presence of the beam. As the beam energy is increased, it passes by the maximal value of the cross section, then disappears in the tail of the Maxwellian part, thus reducing its effect. The picture is about the same in *(b)* for another reaction: $e + N_2(X) \rightarrow 2e + N_2^+(X)$. The threshold energy for this ionisation reaction is 15.6 eV [80], which explains the differences for these reaction rates. The electron beam starts to have an effect on the reaction rate for E_b close to the threshold energy.

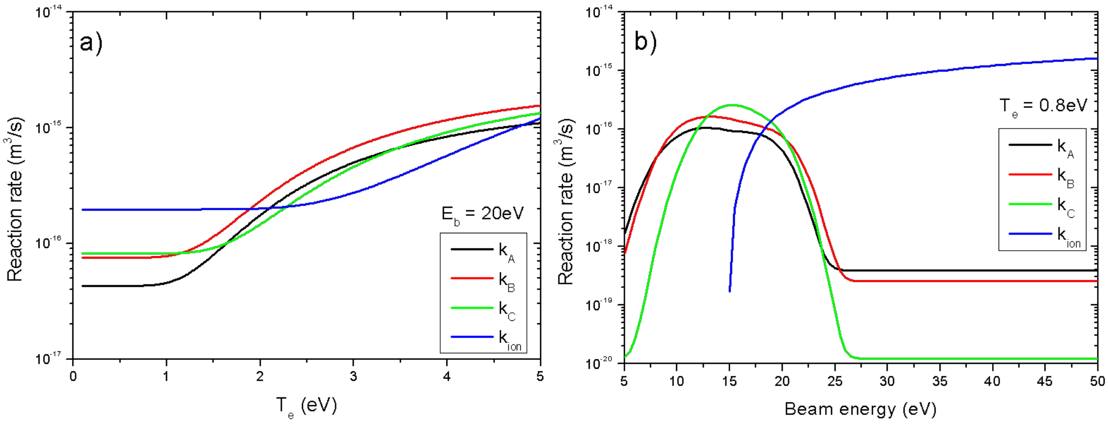

Figure 3.7: Reaction rates as a function of T_e and E_b with a beam-Maxwell distribution *(a)* with a fixed beam energy and *(b)* with a fixed T_e. Electron beam proportion is 2.5% of the total electron density.

The effect on different reaction rates of the two tunable parameters in the beam-Maxwell EEDF is presented in figure (3.7): *(a)* T_e at fixed electron beam energy and *(b)* electron beam energy at fixed T_e. At a fixed electron beam energy the reaction rates exhibit a plateau at low electron temperatures, because only the beam contributes to the excitation. The rise of the reaction rate values depends on the threshold energy. When the T_e of the Maxwellian part is fixed, the behaviour of the reaction rates is different with the increasing electron beam energy. Every reaction rate passes through a maximum before dropping to a constant value, at high electron beam energies, where only the Maxwellian part contributes and because of the drop of the cross section values. The excitation reaction rates have different maximum values due to the shape and the threshold energies of the cross sections. This allows to favour a reaction by tuning the electron beam energy.

From this last figure (3.7), it can be seen that the variation of the excitation reaction rates is globally the same for the different T_e and E_b and there are no large differences in the order of magnitude. This leads to the conclusion that the plasma composition will not exhibit drastic changes by the change of T_e.

3.2 Particle balance model

The particle balance model is used to predict the most important plasma parameters for process plasmas: the electron temperature and the plasma density. It is directly inspired from Lieberman [53] for nitrogen plasmas, supposing an uniform density in the reactor. This model was adapted to nitrogen, using both EEDFs presented earlier, and the evolution of the prediction of the model with the EEDF parameters will be presented as a function of the gas pressure.

The model described in [53] considers a nearly uniform density in the "bulk" plasma, with the density falling sharply near the edges. This is an approximation of a global model, where a profile is assumed. This model also assumes that the electrons absorb the electric power P_{abs}, set into the discharge.

3.2.1 Electron temperature determination

In the particle balance model, T_e is determined by equating losses of particles at the surface as given by the Bohm criterion to the total volume ionisation:

$$n_0 u_B A = k_{ion} n_g n_0 V \tag{3.4}$$

where n_0 is the plasma density, $u_B = \sqrt{\frac{eT_e}{M}}$ the Bohm speed with T_e in eV and M the ion mass, A the area for particle loss, k_{ion} the reaction rate for the ionisation, V the volume where the ionisation takes place and n_g the neutral gas density. Note that u_B and k_{ion} are dependent on T_e, and that the equation is independent of the plasma density. The neutral gas density is calculated from the perfect gas law $p = n_g k_B T_g$, with T_g arbitrary taken at 400 K. The source design determines the volume of creation of ions and the area of particle losses.

The RF plasma source with grid has two separated volumes and areas, and the EEDF is taken to be a Maxwellian distribution. The plasma expands into the chamber, increasing the area for the losses, keeping the same volume for ion creation. The equation (3.4) can thus be rewritten as:

$$n_0 u_B A_{source}\left(1 + \alpha \frac{A_{reactor}}{A_{source}}\right) = k_{ion} n_g n_0 V_{source} \tag{3.5}$$

with α represents the portion of the plasma density passing through the grid of the source, $0 \le \alpha \le 1$. The case $\alpha = 0$ corresponds to the plasma only located in the source, and the case $\alpha = 1$ corresponds to the case of the RF plasma source without a grid, where the density outside the source is the same as the one inside.

If electrons and ions are escaping the source, they can make ionisation outside the source. In this case, the proportion of charged particles escaping the source, $\alpha \cdot n_0$, contributes to the ionisation in the reactor volume. A term $k_{ion} n_g \alpha n_0 V_{reactor}$ in the right hand side of equation (3.5) needs to be added. This leads to

$$n_0 u_B A_{source}\left(1 + \alpha \frac{A_{reactor}}{A_{source}}\right) = k_{ion} n_g n_0 V_{source}\left(1 + \alpha \frac{V_{reactor}}{V_{source}}\right) \tag{3.6}$$

Both equations are rewritten to see the explicit dependence on T_e:

$$\frac{k_{ion}(T_e)}{u_B(T_e)} = \frac{k_B T_g\, A}{p\, V} \tag{3.7}$$

For pressures varying from 10^{-4} mbar to 10^{-1} mbar, an electron temperature is found by solving equation (3.7). A is replaced by $A_{source} + \alpha A_{reactor}$ and V can be either V_{source} or $V_{source} + \alpha V_{reactor}$, depending on the case examined.

Electron temperature as a function of the pressure at different α-values is shown in figure (3.8). In the case of the ion creation only in the source (figure (3.8a), equation (3.5)), when the proportion of the electrons escaping the source is increasing, T_e must increase for the same pressure. To sustain the plasma, the source needs to create more electrons, due to the increasing losses to the walls. On the contrary, in the case of ion creation in the reactor volume (equation (3.6)), T_e is decreasing for a given pressure, because the creation volume is larger than the loss area, for the same α-value. The ratio A/V is decreasing with increasing α.

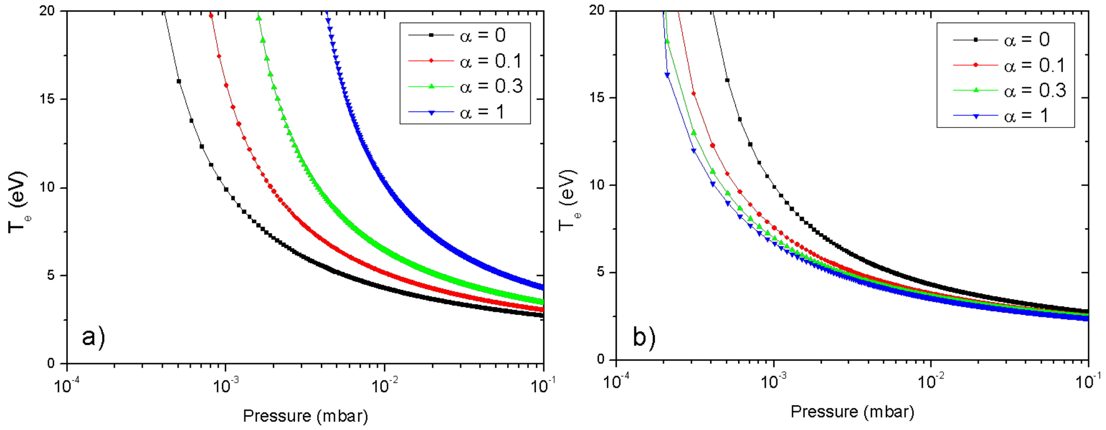

Figure 3.8: Electron temperature as a function of the pressure, for different proportion of plasma density escaping the source, *(a)* with only source volume creation (equation (3.5)) and *(b)* with reactor volume creation (equation (3.6)).

In the DC plasma source, the EEDF is a Maxwellian distribution with an electron beam superimposed, thus two parameters are needed to determine the EEDF: T_e of the bulk Maxwellian part and E_b of the electron beam.

Equation (3.7) has been solved with different E_b in the determination of k_{ion}, with the Bohm speed only depending on T_e, because it only concerns the ions. The figure (3.9) presents the results of the calculations with $E_b = 9, 10, 20, 25$ eV, with a constant proportion of 2.5% of electrons in the beam and an energy width of 1.5 eV.

The shape of the curve is similar to the ones with the Maxwell EEDF, and are even superposed for beam energies below the ionisation cross section threshold energy. For

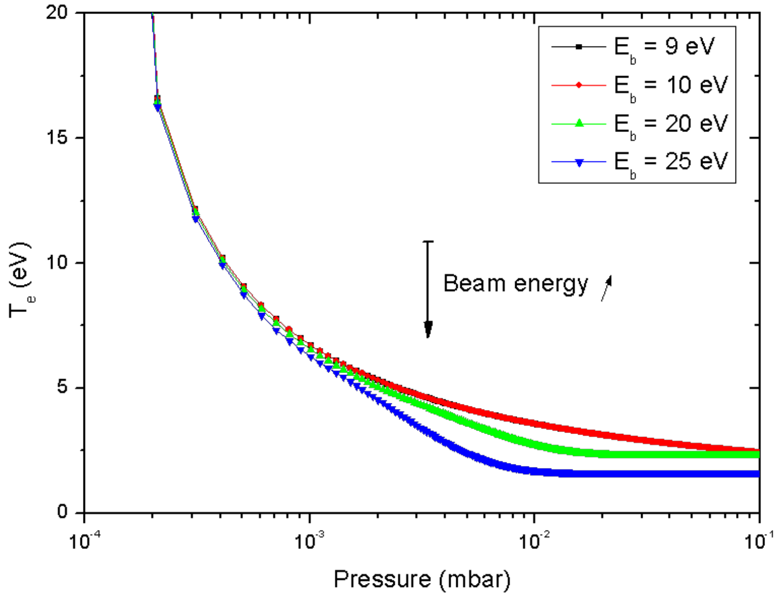

Figure 3.9: Calculated electron temperature as a function of the pressure with different electron beam energies E_b.

beam energies higher than the threshold energy (15.6 eV), T_e is decreased, because the electrons from the beam contribute to the ionisation.

Conclusion

T_e is determined by equating the particle loss at surfaces and volume ionisation, by solving the equation (3.7), with the ratio A/V depending on the configuration and the plasma source used. The evolution of T_e with pressure has globally the same shape for the configurations tested, and is almost independent on the EEDF used. In fact, the presence of the electron beam has only a low impact on the shape of the T_e curves, which is mainly dependent on the pressure, but decreases the values of T_e for $E_b \geq 16$ eV.

3.2.2 Plasma density determination

The plasma density n_0 in the equation (3.4) can be determined using the power balance, which equates the total power absorbed, P_{abs}, to the total power loss

$$P_{abs} = en_0 u_B A \mathcal{E}_T \qquad (3.8)$$

where e is the elementary charge, u_B the Bohm speed, A the area of particle loss and $\mathcal{E}_T$ the total energy lost per electron-ion pair lost.

This latter term describes the contribution of several phenomena. $\mathcal{E}_T$ contains the collisional energy loss, $\mathcal{E}_c$, the mean kinetic energy loss per electron, $\mathcal{E}_e$, and the mean kinetic energy loss per ion, $\mathcal{E}_i$. The total energy lost is then

$$\mathcal{E}_T = \mathcal{E}_c + \mathcal{E}_e + \mathcal{E}_i \tag{3.9}$$

The collisional energy loss per electron-ion pair created is defined as

$$k_{ion}\mathcal{E}_c = k_{ion}\mathcal{E}_{ion} + k_{exc}\mathcal{E}_{exc} + k_{elast}\frac{3m}{M}T_e \tag{3.10}$$

with $\mathcal{E}_{ion}$ and $\mathcal{E}_{exc}$ the threshold energies for the ionisation and excitation cross sections. The quantity $(3m/M)T_e$ is the mean energy lost per electron by elastic collision. The terms on the right hand side account for the loss of electron energy due to the ionisation, excitation and elastic scattering against neutral molecules. These are usually the dominant losses in weakly ionised plasmas. As seen in equation (3.10) $\mathcal{E}_c$ is dependent on the reaction rates, thus depending on T_e. The excitation rate constant is the sum of the rates for the electronic states excitation N_2(A), N_2(B) and N_2(C), and the threshold energies are taken at 15.6 eV and 7.65 eV respectively for $\mathcal{E}_{ion}$ and $\mathcal{E}_{exc}$. At high T_e, $\mathcal{E}_c$ tends asymptotically to about 20 V.

The mean kinetic energy loss per electron lost is found to be

$$\mathcal{E}_e = 2T_e \tag{3.11}$$

This relation comes from the calculation of the average energy flux in one direction, which is $S_z = 2kT\Gamma_z$ (in the z direction), with $\Gamma_z = \frac{1}{4}n\bar{v}$. The details of the calculation can be found in [53].

Finally, the mean kinetic energy loss per ion lost, $\mathcal{E}_i$, is the sum of the ion energy entering the sheath and the energy gained by the ion as it traverses the sheath. The ion velocity entering the sheath is u_B, corresponding to an energy of $T_e/2$. The sheath voltage, V_s, can be expressed as

$$V_s = T_e \ln\left(\frac{M}{2\pi m}\right)^{1/2} \tag{3.12}$$

or $V_s \approx 4.5T_e$ for nitrogen. Thus $\mathcal{E}_i = V_s + \frac{1}{2}T_e \approx 5T_e$.

Using the the total energy lost per electron-ion pair lost $\mathcal{E}_T$, the equation (3.8) can be solved for n_0, and the result is

$$n_0(P_{abs}, T_e) = \frac{P_{abs}}{eu_B(T_e)A\mathcal{E}_T(T_e)} \tag{3.13}$$

which gives n_0 for a specified P_{abs} and a given value for T_e. It can be noted that n_0 is determined by the total power balance in the discharge, and is a function of pressure only through the pressure dependence of T_e.

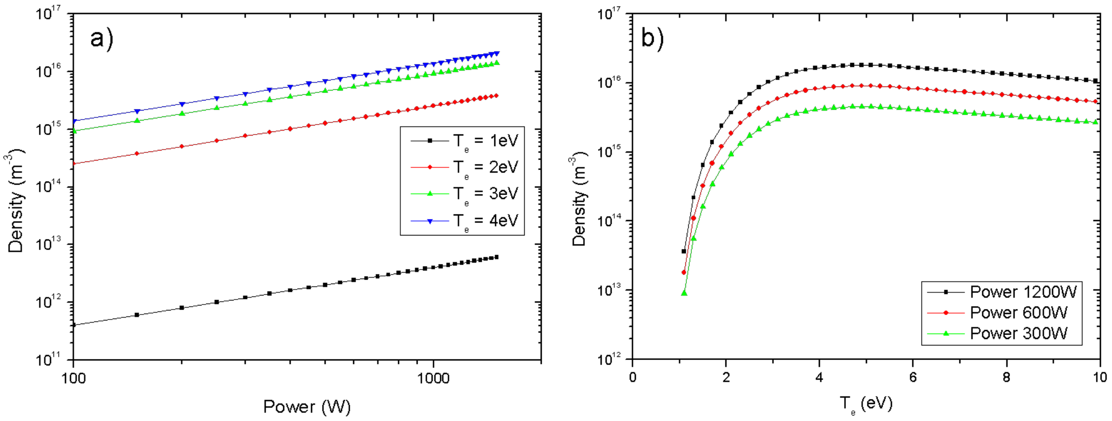

Figure 3.10: Calculated plasma density as a function of the power with *(a)* constant T_e and *(b)* constant power.

Figure (3.10) shows the plasma density as a function of the power calculated for nitrogen with equation (3.13) at fixed T_e and varying the absorbed power, and at constant power and varying the T_e. In the part *(a)*, the evolution at constant T_e is linear, as predicted by equation (3.13). The absolute density is determined by T_e, with a strong dependence at low temperature, due to the large variation of $\mathcal{E}_T$. This variation of the density with T_e is seen on the part *(b)* of figure (3.10). At high temperatures the contribution of $\mathcal{E}_c$ is lower than the other terms in the right hand side of equation (3.9). This leads to the slight decrease of the density at higher T_e. The maximal density is found around 5 eV for all the calculated powers.

With the DC plasma source, the calculation is the same, but the total energy lost per electron-ion pair lost $\mathcal{E}_T$ is changing because of the presence of the electron beam. In fact the reaction rates in equation (3.10) are modified, in particular the ionisation reaction rate.

Figure (3.11) shows $\mathcal{E}_c$ variation with T_e for different E_b, calculated with a beam-Maxwell EEDF. For low electron beam energies, the presence of the beam does not make the collisional energy loss per electron-ion pair created vary much from the pure Maxwellian distribution case, because the main reaction rate (ionisation) is not affected. The asymptotes for the curves with $E_b = 5$ eV and $E_b = 10$ eV are the same as with a pure Maxwellian distribution. For high electron beam energies, the shape of the curve is different at lower T_e because the ionisation is increased. For higher T_e the beam has no effect, because it is drowned in the Maxwellian part of the distribution.

In order to find the plasma density, equation (3.8) applied to the DC plasma source can

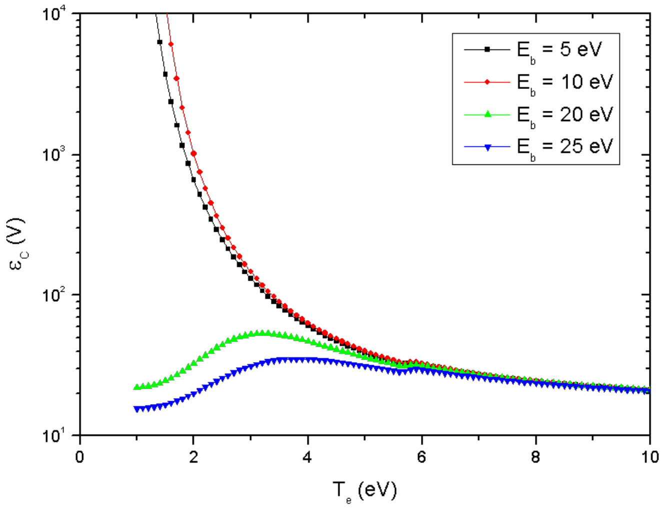

Figure 3.11: Collisional energy loss per electron-ion pair created in nitrogen, as a function of T_e for different E_b, in the case of a beam-Maxwell EEDF.

be rewritten as:

$$n_0(P_{abs}, T_e, E_b) = \frac{P_{abs}}{eu_B(T_e)A\mathcal{E}_T(T_e, E_b)} \tag{3.14}$$

because the reaction rates are depending on the electron beam energy, but not the Bohm velocity.

The plasma density has been calculated for different EEDF parameters, with a constant electron beam energy and various T_e, and for fixed T_e and increasing electron beam energies, shown in figure (3.12). With fixed E_b, the increase of T_e leads to a decrease in the density, because the mean energy carried by electrons is increased, thus less electrons are needed to sustain the discharge. The densities are one order of magnitude higher than in the case of a pure Maxwell distribution, for T_e values below 3 eV. At fixed T_e (part *(b)*), the increase of E_b leads to an increase of the density. The reason is that the behaviour of $\mathcal{E}_T$ is highly dependent on E_b through $\mathcal{E}_c$ (figure (3.11)). In fact with a fixed T_e, the Bohm speed is determined, and the density is directly linked to $\mathcal{E}_T$, which drastically decreases with E_b at $T_e = 1$ eV.

The absorbed power has then been fixed in equation (3.14) to study the effects of the EEDF parameters on the density. Figure (3.13) presents the evolution of the plasma density at fixed P_{abs} and *(a)* fixed E_b and *(b)* fixed T_e. At fixed E_b the density decreases with T_e, because the Bohm velocity increases and the collision losses also. Above $T_e \approx 3$ eV, the decrease is less marked because the collisional energy loss is reducing also. The cross section of the direct ionisation is rather constant above 20 eV, explaining the plateau of plasma density. The dependence on the beam energy is low because the reaction rate does not vary much above $E_b = 20$ eV (figure (3.7b)).

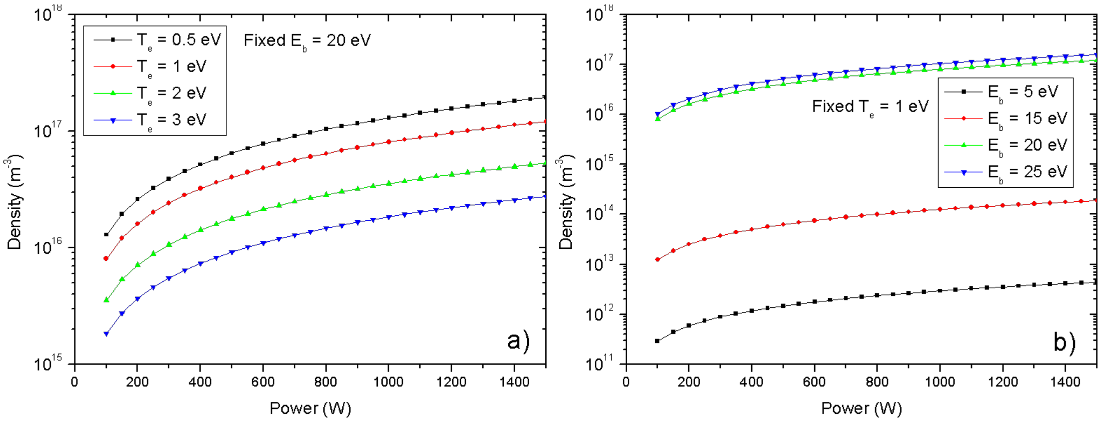

Figure 3.12: Evolution of the density with absorbed power with *(a)* fixed E_b and various T_e and *(b)* fixed T_e and various E_b.

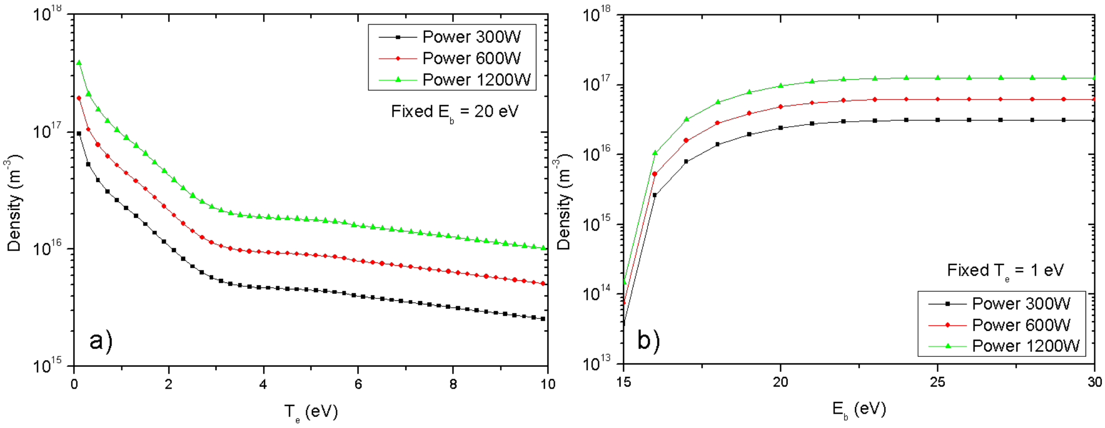

Figure 3.13: Evolution of the density at fixed absorbed power with *(a)* fixed E_b and various T_e and *(b)* fixed T_e and various E_b.

Conclusion

The plasma density is found by equating the power absorbed by the plasma to the power loss by collision, by solving either equation (3.13) or (3.14), depending on the plasma source used. Once the EEDF parameters are fixed (T_e and E_b), the power determines the plasma density. When the absorbed power is fixed, the behaviour of the density with T_e is dependent on the EEDF. In fact, the presence of the beam influences the ionisation, and thus the $\mathcal{E}_T$ value is tendentially low compared to the value without the beam, especially at lower T_e. At low T_e the plasma density is found to be one order of magnitude higher in presence of an electron beam.

3.3 Corona model

The corona model is a simple model widely used in literature [26, 40, 42, 86] to calculate the excited states density in a plasma. It is used to explain the spectral intensities or molecular bands, and consists of balancing the electron impact excitation by radiative decay for the different excited states. It is generally a simplification of more complex models, taking into account a lot more reactions for the excitation and de-excitation processes. The resulting balance equations are solved for each state.

In nitrogen the excited states are the electronic states N_2(A), N_2(B) and N_2(C). The radiative states of nitrogen are the N_2(B) and N_2(C), and another excited state is the metastable N_2(A) state. For the long life metastable state N_2(A), due to the low pressure regime in this work, the main loss is the diffusion to the walls, as the radiative decay time is much longer than the time needed to reach a surface. The resulting balance equations are, respectively for N_2(C), N_2(B) and N_2(A):

$$\begin{aligned} n_e n_g k_{exc,C} &= n_C \sum A_{C\to B} \\ n_e n_g k_{exc,B} + n_C \sum A_{C\to B} &= n_B \sum A_{B\to A} \\ n_e n_g k_{exc,A} + n_B \sum A_{B\to A} &= n_A \frac{D}{\Lambda^2} \end{aligned}$$

where $k_{exc,i}$ is the excitation reaction rate for the i state from the neutral gas, n_e the electron density, n_g the neutral gas density, n_i the i excited state density, $\sum A_{i\to j}$ the sum of the Einstein coefficients for spontaneous emission of the radiative state i to the state j, D the diffusion coefficient for nitrogen in nitrogen [87] and Λ the characteristic length of the reactor. The neutral gas density is calculated from the perfect gas law $p = n_g k_B T_g$. Einstein coefficients for spontaneous emission are the probability for an excited state to de-excite by emitting a photon [59]. The sum of the Einstein coefficients for a entire electronic state is the total probability for the state to de-excite by radiation. This corresponds to the inverse of the lifetime of the state, found in literature [59]. The characteristic length of the reactor is the smallest distance to the walls. As the reactor can be approximated to a cylinder, the characteristic length is $R/2.405$ [88], with R the radius of the reactor. The diffusion coefficient is found in transport theory [87] and can be written as

$$D = \frac{2}{3}\left(\frac{k_B^3}{\pi^3 M}\right)^{1/2} \frac{T_g^{3/2}}{d^2 p} \tag{3.15}$$

where k_B is the Boltzmann's constant, M the mass of the particle, d its diameter, T_g the gas temperature taken here arbitrary at 400 K and p the pressure.

The system of equations can be rewritten as

$$n_C = \frac{n_e n_g k_{exc,C}}{\sum A_{C\to B}} \tag{3.16}$$

$$n_B = \frac{n_e n_g \left(k_{exc,B} + k_{exc,C}\right)}{\sum A_{B\to A}} \tag{3.17}$$

$$n_A = \frac{n_e n_g \left(k_{exc,A} + k_{exc,B} + k_{exc,C}\right)}{D/\Lambda^2} \tag{3.18}$$

Using the plasma parameters determined from the previous described particle balance model, the reaction rates for excitation are calculated as described in equation (3.1), with the cross sections from Itikawa [80] (the more recent in literature) and a Maxwellian or beam-Maxwell distribution. For the pure Maxwellian distribution n_e is determined with an absorbed power $P_{abs} = 1200$ W (equation (3.13), typical RF power used with our RF plasma source), and for the beam-Maxwellian distribution, E_b is fixed at 20 eV and the absorbed power taken at $P_{abs} = 400$ W (typical experimental power for our DC plasma source).

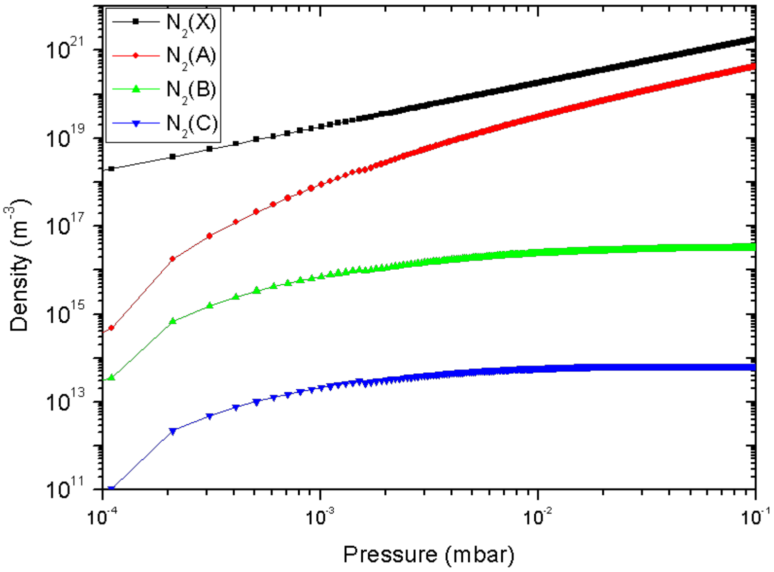

Figure 3.14: Excited states and ground state densities obtained with the corona model, with the electron densities and temperatures from the particle balance model (figures (3.8) and (3.10) respectively).

The the three excited states and the neutral gas density as a function of the pressure are shown in figure (3.14). The ground state density increases linearly with the pressure. At the lowest pressures in the regime, T_e is very high (figure (3.8)), thus the tail of the EEDF is large, leading to low excited state densities. When the pressure is increased, i.e. T_e decreased, the low energetic state (N_2(A)) is favoured, because the EEDF becomes more sharp and peaked at low energy. This also leads to a flattening of the other states N_2(B) and N_2(C) at higher pressure.

With the DC plasma source, the procedure and the system of equations to solve are the same, only the reaction rates are changed, due to the presence of the electron beam. The evolution of the densities of the neutral and excited states with pressure is shown in figure (3.15). The behaviour of the densities is very similar to the ones with pure Maxwellian distribution. The densities are also very close between both EEDFs. The composition of the plasma is unchanged with the pressure increase and the change of EEDF.

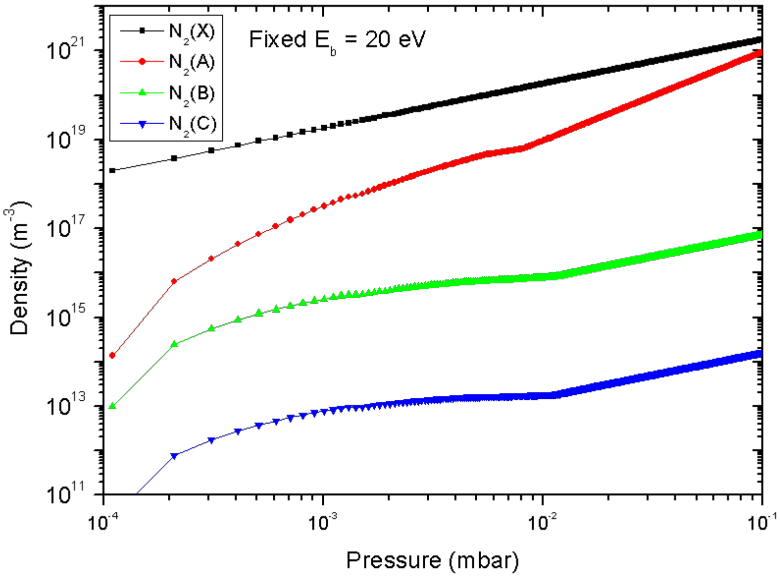

Figure 3.15: Excited states and ground state densities obtained with the corona model, with the electron densities and temperatures from the particle balance model at a fixed beam energy $E_b = 20$ eV (figures (3.9) and (3.12) respectively).

The ratio of the radiative states density $N_2(C)/N_2(B)$ is shown in figure (3.16) for the two different EEDFs, and will be compared with the experiment in the following chapters. Both EEDFs exhibit the same behaviour: with increasing pressure, the ratio decreases. This is due to the diminution of T_e, leading to an increase of the $N_2(B)$ state because the maximum of the cross section is at lower energy than the one of the $N_2(C)$ state (figure (3.2)). The value of the ratio is between 2 and $3 \cdot 10^{-3}$, indicating that the $N_2(C)$ is the lower density between the excited states.

Conclusion

The corona model is used to calculate the density of the radiative states considering one populating process (electron impact excitation) and one de-populating process (spontaneous radiative decay). The inputs of the model are the electron temperature and density. Using the evolution with pressure of T_e and n_e from the particle balance model, the densities of the three main electronic states of nitrogen were calculated, with

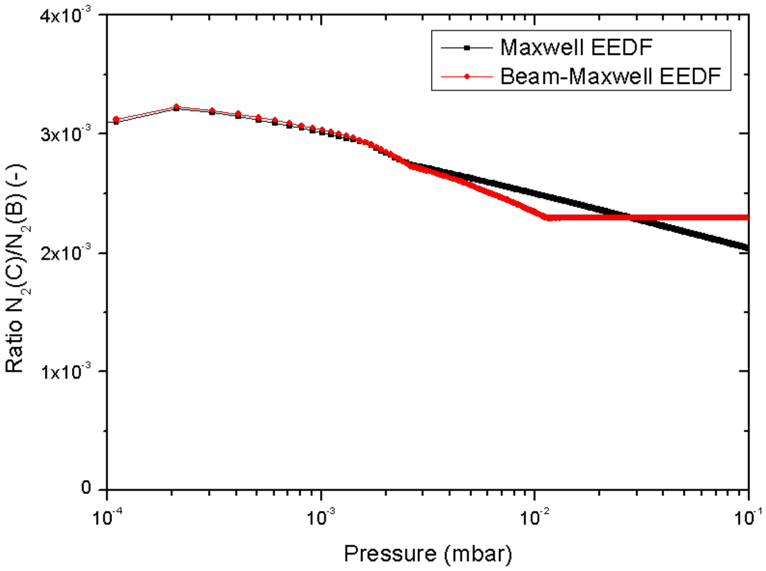

Figure 3.16: Ratio of the radiative states $N_2(C)$ and $N_2(B)$ as a function of the pressure, using both EEDFs.

both EEDFs. As T_e is lower in the case with the electron beam, the densities are slightly lower. The ratios between the radiative states exhibit the same behaviour with pressure.

3.4 Collisional-radiative model

The collisional-radiative (CR) model is an analytical model solving balance equations using more processes than the corona model. It permits also to calculate the densities of non radiative states, contrary to the corona model. In this work, it consists of taking into account possible reactions of the nitrogen molecule with electrons and of neglecting heavy particles collisions due to the low pressure regime. The rate constant of each reaction is calculated, using the cross sections found in literature [80–82] and a Maxwell or a beam-Maxwell EEDF. The balance equations are solved together using Mathematica™.

The complete set of reactions taken into account is shown in table (3.1). The reaction rates k, Einstein coefficient for spontaneous emission A and diffusion coefficients D (ambipolar for charged particles) also shown are calculated with a Maxwell EEDF at $T_e = 3$ eV and $p = 1.3 \cdot 10^{-3}$ mbar. The cross sections used are taken from the references given in the table (3.1).

Ambipolar diffusion results from the electric field created between the plasma potential and the grounded walls. The origin of the electric field is the difference of mass between the ions and electrons [53]. It arises to keep the electron and ion fluxes equal in the

#	Reactions	Threshold energy	k, A or D	Cross section reference
(1)	$e + N_2(X) \rightarrow e + N_2(A)$	7.65 eV	$4.393 \cdot 10^{-16}$ m^{3}s^{-1}	[80]
(2)	$e + N_2(X) \rightarrow e + N_2(B)$	8.55 eV	$5.738 \cdot 10^{-16}$ m^{3}s^{-1}	[80]
(3)	$e + N_2(X) \rightarrow e + N_2(C)$	11 eV	$3.531 \cdot 10^{-16}$ m^{3}s^{-1}	[80]
(4)	$e + N_2(X) \rightarrow 2e + N_2^+(X)$	15.6 eV	$6.666 \cdot 10^{-17}$ m^{3}s^{-1}	[80]
(5)	$e + N_2(A) \rightarrow e + N_2(B)$	1 eV	$4.078 \cdot 10^{-14}$ m^{3}s^{-1}	[82]
(6)	$e + N_2(A) \rightarrow e + N_2(C)$	5 eV	$2.599 \cdot 10^{-14}$ m^{3}s^{-1}	[82]
(7)	$e + N_2(B) \rightarrow e + N_2(C)$	3.5 eV	$3.426 \cdot 10^{-14}$ m^{3}s^{-1}	[82]
(8)	$e + N_2(A) \rightarrow 2e + N_2^+(X)$	10.5 eV	$9.659 \cdot 10^{-17}$ m^{3}s^{-1}	[82]
(9)	$e + N_2(X) \rightarrow e + 2N$	9.8 eV	$5.434 \cdot 10^{-16}$ m^{3}s^{-1}	[82]
(10)	$e + N_2(A) \rightarrow e + 2N$	5.5 eV	$5.666 \cdot 10^{-13}$ m^{3}s^{-1}	[82]
(11)	$e + N_2(B) \rightarrow e + 2N$	5.5 eV	$1.537 \cdot 10^{-13}$ m^{3}s^{-1}	[82]
(12)	$e + N_2(C) \rightarrow e + 2N$	1.5 eV	$1.663 \cdot 10^{-12}$ m^{3}s^{-1}	[82]
(13)	$e + N_2^+(X) \rightarrow 2N$	9 eV	$1.609 \cdot 10^{-15}$ m^{3}s^{-1}	[82]
(14)	$e + N_2^+(B) \rightarrow 2N$	9 eV	$3.024 \cdot 10^{-14}$ m^{3}s^{-1}	[82]
(15)	$e + N_2^+(X) \rightarrow e + N_2^+(B)$	3 eV	$2.341 \cdot 10^{-14}$ m^{3}s^{-1}	[82]
(16)	$e + N_2(X) \rightarrow 2e + N_2^+(B)$	19 eV	$3.970 \cdot 10^{-18}$ m^{3}s^{-1}	[82]
(17)	$e + N_2(A) \rightarrow 2e + N_2^+(B)$	14 eV	$4.536 \cdot 10^{-17}$ m^{3}s^{-1}	[82]
(18)	$N_2(C) \rightarrow N_2(B) + h\nu$	–	$2.603 \cdot 10^{7}$ s^{-1}	[59]
(19)	$N_2(B) \rightarrow N_2(A) + h\nu$	–	$1.565 \cdot 10^{5}$ s^{-1}	[59]
(20)	$N_2^+(B) \rightarrow N_2^+(X) + h\nu$	–	$1.538 \cdot 10^{7}$ s^{-1}	[59]
(21)	$N_2(A) \xrightarrow{wall} N_2(X)$	–	1372 m^{2}s^{-1}	[87]
(22)	$N_2^+(X) \xrightarrow{wall} N_2(X)$	–	$4.23 \cdot 10^{-2}$ m^{2}s^{-1}	[53]
(23)	$N_2^+(B) \xrightarrow{wall} N_2(X)$	–	$4.23 \cdot 10^{-2}$ m^{2}s^{-1}	[53]
(24)	$N \xrightarrow{wall} \frac{1}{2}N_2(X)$	–	$1.140 \cdot 10^{4}$ m^{2}s^{-1}	[87]

Table 3.1: Reactions taken into account in the CR model, for the reaction rates: $p = 1.3 \cdot 10^{-3}$ mbar and $T_e = 3$ eV (Maxwell EEDF).

plasma. By equating the fluxes, the ambipolar diffusion coefficient can be expressed as

$$D_a = \frac{\mu_i D_e + \mu_e D_i}{\mu_i + \mu_e} \tag{3.19}$$

with $\mu = \frac{|q|}{m\nu_m}$ the macroscopic mobility of ions and electrons and $D = \frac{kT}{m\nu_m}$ the diffusion constant, with ν_m the momentum transfer frequency. The ambipolar diffusion coefficient can usually be simplified by noting that $\mu_e \gg \mu_i$ in a weakly ionised plasma [53]. Using the Einstein relation between the transport coefficients ($D = \mu\frac{kT}{q} = \mu T$) one obtains for D_a

$$D_a \approx D_i\left(1 + \frac{T_e}{T_i}\right) = \mu_i T_i\left(1 + \frac{T_e}{T_i}\right) \tag{3.20}$$

with the temperatures expressed in eV.

From the set of reactions, the density of each state can be calculated by solving its balance equation, equating the creation processes to the destruction processes. The inputs of the models are the initial neutral density $N_2(X)$, determined by the gas inlet flow and the pumping speed, the electron density, determined by the previous described particle balance model, and the parameters of the desired EEDF.

The density of a precursor is also determinant for the effect of a reaction on the density of the final state, not only the reaction rate. In fact some reactions with high reaction rates reactions are negligible due to the very low density of the precursor, for example the dissociation from the excited molecular ion. The densities using Maxwellian distribution for a fixed $T_e = 3$ eV, $p = 10^{-3}$ mbar and $P_{RF} = 1200$ W is shown in table (3.2); and in table (3.3) using a beam-Maxwell distribution with: $T_e = 1.5$ eV, $E_b = 18$ eV, $p = 10^{-3}$ mbar and $P_{DC} = 400$ W (corresponding to an I_{ARC} of 10 A).

$N_2(X)$	$N_2(A)$	$N_2(B)$	$N_2(C)$
$2.06 \cdot 10^{19}$ m^{-3}	$3.90 \cdot 10^{16}$ m^{-3}	$1.48 \cdot 10^{15}$ m^{-3}	$3.51 \cdot 10^{12}$ m^{-3}
$N_2^+(X)$	$N_2^+(B)$	e^-	N
$9.83 \cdot 10^{15}$ m^{-3}	$2.22 \cdot 10^{11}$ m^{-3}	$1.00 \cdot 10^{16}$ m^{-3}	$4.97 \cdot 10^{16}$ m^{-3}

Table 3.2: Densities obtained with the reactions set of table (3.1) using a Maxwell EEDF, with $T_e = 3$ eV, $p = 10^{-3}$ mbar and $P_{RF} = 1200$ W.

$N_2(X)$	$N_2(A)$	$N_2(B)$	$N_2(C)$
$2.06 \cdot 10^{19}$ m^{-3}	$3.14 \cdot 10^{16}$ m^{-3}	$6.57 \cdot 10^{14}$ m^{-3}	$2.05 \cdot 10^{12}$ m^{-3}
$N_2^+(X)$	$N_2^+(B)$	e^-	N
$1.30 \cdot 10^{16}$ m^{-3}	$1.09 \cdot 10^{11}$ m^{-3}	$1.30 \cdot 10^{16}$ m^{-3}	$3.11 \cdot 10^{16}$ m^{-3}

Table 3.3: Densities obtained with the reactions set of table (3.1) using a beam-Maxwell EEDF, with $T_e = 1.5$ eV, $E_b = 18$ eV, $p = 10^{-3}$ mbar and $P_{DC} = 400$ W ($I_{ARC} = 10$ A).

Some reactions have been found to be negligible, for example the dissociation from the excited states (reactions number (11) and (12) in table (3.1)), and do not change the density of the final states more than 0.1%. The dominant reactions with their rates are summarised in table (3.4). Using the beam-Maxwell distribution, the reaction rates highlight that the excitations are less efficient due to the lowering of T_e and the electron beam at 18 eV, whereas the high energetic processes such as ionisation and dissociation are favoured.

Taking the supposed evolution with pressure of T_e and n_e from the particle balance model, the evolution of the densities of each states can be calculated, as for the corona model. However, with this method, it appears that the quasi-neutrality condition in a plasma is not respected with both EEDFs. In fact, due to the high T_e obtained from the particle balance model (figures (3.8) and (3.9)), the high energetic processes are favoured, leading to a high ionisation rate. The molecular ion density is then higher than the calculated electron density from the particle balance model. As another example, the densities

#	Reactions			k, A or D Maxwell	k, A or D beam-Maxwell
(1)	$e+N_2(X)$	$\rightarrow$	$e+N_2(A)$	$4.393\cdot10^{-16}$ m^{3}s^{-1}	$1.163\cdot10^{-16}$ m^{3}s^{-1}
(2)	$e+N_2(X)$	$\rightarrow$	$e+N_2(B)$	$5.738\cdot10^{-16}$ m^{3}s^{-1}	$1.503\cdot10^{-16}$ m^{3}s^{-1}
(3)	$e+N_2(X)$	$\rightarrow$	$e+N_2(C)$	$3.531\cdot10^{-16}$ m^{3}s^{-1}	$1.873\cdot10^{-16}$ m^{3}s^{-1}
(4)	$e+N_2(X)$	$\rightarrow$	$2e+N_2^+(X)$	$6.666\cdot10^{-17}$ m^{3}s^{-1}	$8.653\cdot10^{-17}$ m^{3}s^{-1}
(5)	$e+N_2(A)$	$\rightarrow$	$e+N_2(B)$	$4.078\cdot10^{-14}$ m^{3}s^{-1}	$2.591\cdot10^{-14}$ m^{3}s^{-1}
(6)	$e+N_2(A)$	$\rightarrow$	$e+N_2(C)$	$2.599\cdot10^{-14}$ m^{3}s^{-1}	$7.549\cdot10^{-15}$ m^{3}s^{-1}
(7)	$e+N_2(X)$	$\rightarrow$	$e+2N$	$5.434\cdot10^{-16}$ m^{3}s^{-1}	$6.068\cdot10^{-16}$ m^{3}s^{-1}
(8)	$e+N_2(A)$	$\rightarrow$	$e+2N$	$5.666\cdot10^{-13}$ m^{3}s^{-1}	$1.642\cdot10^{-13}$ m^{3}s^{-1}
(9)	$e+N_2^+(X)$	$\rightarrow$	$e+N_2^+(B)$	$2.341\cdot10^{-14}$ m^{3}s^{-1}	$8.110\cdot10^{-15}$ m^{3}s^{-1}
(10)	$e+N_2(X)$	$\rightarrow$	$2e+N_2^+(B)$	$3.970\cdot10^{-18}$ m^{3}s^{-1}	$1.310\cdot10^{-18}$ m^{3}s^{-1}
(11)	$N_2(C)$	$\rightarrow$	$N_2(B)+h\nu$	$2.603\cdot10^{7}$ s^{-1}	$2.603\cdot10^{7}$ s^{-1}
(12)	$N_2(B)$	$\rightarrow$	$N_2(A)+h\nu$	$1.565\cdot10^{5}$ s^{-1}	$1.565\cdot10^{5}$ s^{-1}
(13)	$N_2^+(B)$	$\rightarrow$	$N_2^+(X)+h\nu$	$1.538\cdot10^{7}$ s^{-1}	$1.538\cdot10^{7}$ s^{-1}
(14)	$N_2(A)$	$\xrightarrow{wall}$	$N_2(X)$	1372 m^{2}s^{-1}	1757 m^{2}s^{-1}
(15)	$N_2^+(X)$	$\xrightarrow{wall}$	$N_2(X)$	1372 m^{2}s^{-1}	1757 m^{2}s^{-1}
(16)	N	$\xrightarrow{wall}$	$\frac{1}{2}N_2(X)$	$1.140\cdot10^{4}$ m^{2}s^{-1}	$1.46\cdot10^{4}$ m^{2}s^{-1}

Table 3.4: Dominant reactions of the CR model, for the reaction rates using Maxwellian distribution: $p=1.3\cdot10^{-3}$ mbar and $T_e=3$ eV; and with the beam-Maxwell EEDF, with $T_e=1.5$ eV, $E_b=18$ eV and $p=1.3\cdot10^{-3}$ mbar.

calculated in table (3.2) were calculated with $T_e=3$ eV, obtaining the quasi-neutrality, but the particle balance model predicts a T_e of about 6 eV for this same pressure for a Maxwell distribution. In order to satisfy the quasi-neutrality condition, the T_e were determined using the reactions of the CR model for different pressures. The comparison between the particle balance model and the CR model predictions for T_e with a Maxwell EEDF is shown in figure (3.17a). The part *(b)* presents the results with a beam-Maxwell EEDF with $E_b=20$ eV.

The T_e found with the CR model are lower over the whole pressure range studied, but the shape of the curve is similar. The temperatures found with the particle balance model are thus overestimated and lead to the violation of the plasma quasi-neutrality when they are used in the CR model. With the beam-Maxwell EEDF, T_e are lower than the ones found with the particle balance model and with a Maxwell EEDF due to the strong ionisation coming from the high energetic electron beam, but the global shape of the temperature curve is similar. T_e giving the quasi-neutrality in the CR model will be used from now.

The densities of the different nitrogen species as a function of pressure are shown in figure (3.18), using Maxwellian EEDF. The evolution with pressure of almost all the species is the same as the electron density. In fact, only the atomic nitrogen and the metastable densities do not have their maximum at about $3-4\cdot10^{-4}$ mbar. The electron and ion

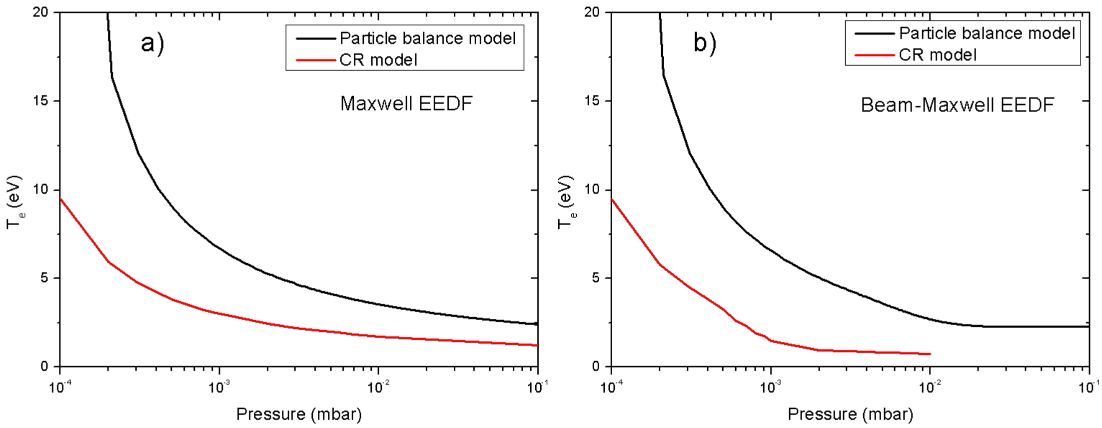

Figure 3.17: T_e comparison between the particle balance model and the CR model, when quasi-neutrality condition is fulfilled, with *(a)* Maxwell EEDF and *(b)* beam-Maxwell EEDF, $E_b = 20$ eV.

densities then decrease because of the decrease of T_e of the Maxwellian distribution. This is also favouring the low energetic states, such as the metastable N_2(A). As this latter is increased, the dissociation from this state is more efficient (reaction (8), table (3.4)), thus the density of the atomic nitrogen increases even if the electron density decreases.

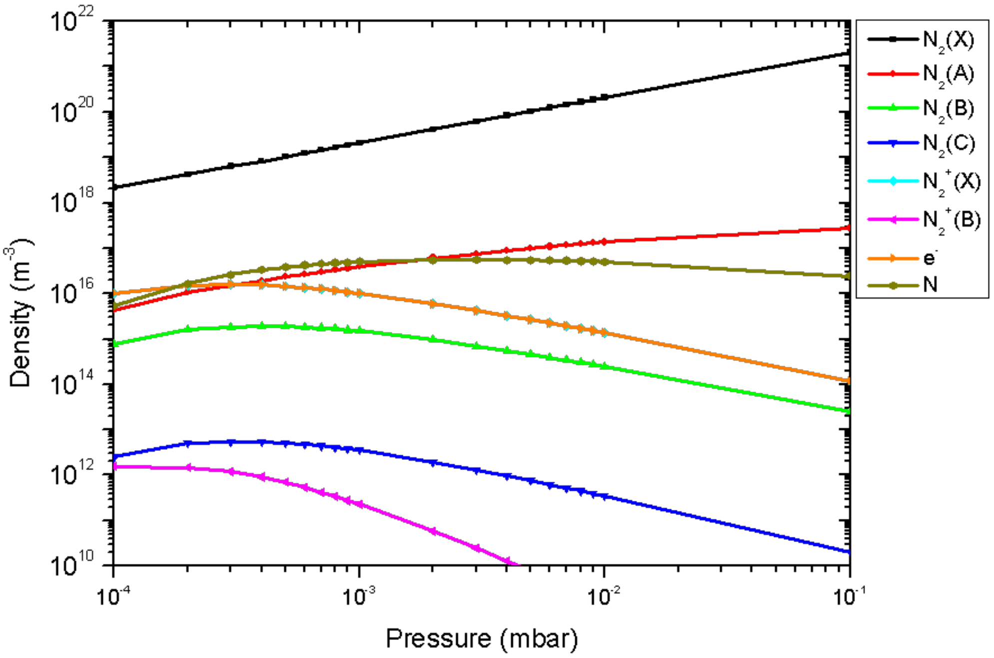

Figure 3.18: Density of the species as a function of the pressure from the CR model, using Maxwellian EEDF at T_e giving the quasi-neutrality.

Figure (3.19) shows the evolution of the ratio between the radiative states with the CR and the corona models, using in both models Maxwellian EEDF with T_e from the CR

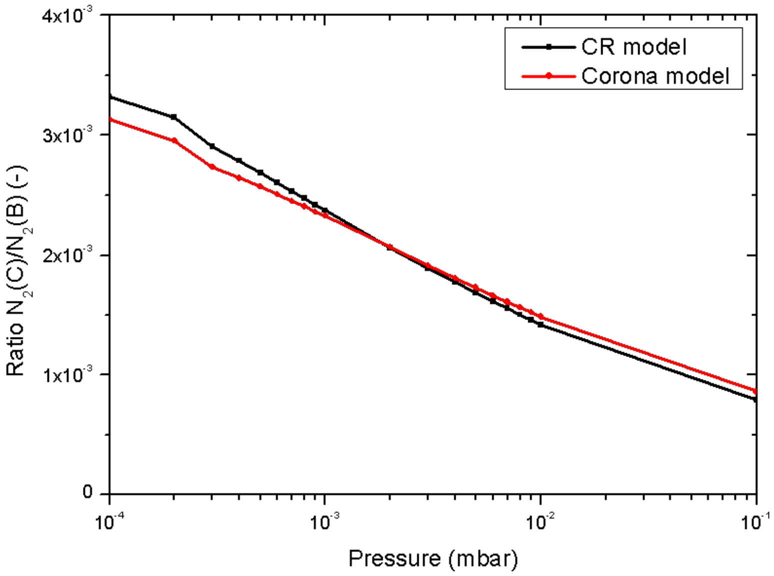

Figure 3.19: Ratio of the radiative states N_2(C) and N_2(B) as a function of the pressure with the CR and corona models with a pure Maxwellian distribution.

model. The curves are almost superimposed. The ratio decrease highlights the fact that T_e is decreasing, favouring the N_2(B) state.

For a Maxwellian EEDF, the CR and the corona models give the same conclusions for the radiative states, meaning that the electron impact excitation from the ground state and the radiative decays are the dominant processes for the production and the destruction of the radiative species, respectively. To get an estimation of the ratio between the states, the corona model is sufficient. If the density of other species in the plasma are needed, the CR model has to be used.

Using the beam-Maxwell EEDF, the densities of the nitrogen species as a function of the pressure were calculated and are presented in figure (3.20). The behaviour is very similar to the ones obtained with the Maxwell EEDF. The decrease of the electron and ion densities is more pronounced in the beam-Maxwell EEDF case, and the final plasma density approaches 10^{14} m^{-3}, at a pressure 10 times lower. The densities of the radiative states N_2(B) and N_2(C) are almost constant in the pressure range. At low pressure the high bulk T_e contributes to the excitation, then the lowering of the beam energy makes the excitation favourable from the electron beam. The fact that the densities evolve in the same manner and that the orders of magnitude are the same in both cases leads to the conclusion that the beam-Maxwell EEDF with a lower bulk T_e and a Maxwell EEDF at higher T_e are equivalent in terms of plasma composition, as highlighted by the evolution of the reaction rates with the EEDF parameters.

The ratio between the radiative states obtained with both models in the DC case is

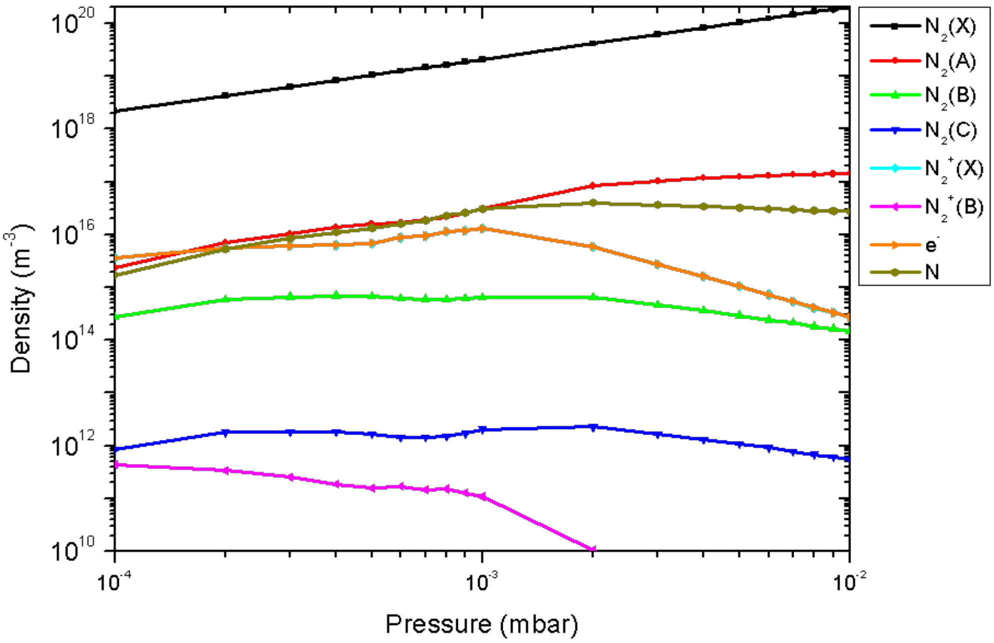

Figure 3.20: Density of the species as a function of the pressure from the CR model with a beam-Maxwell EEDF, using T_e from the CR model shown in figure (3.17b).

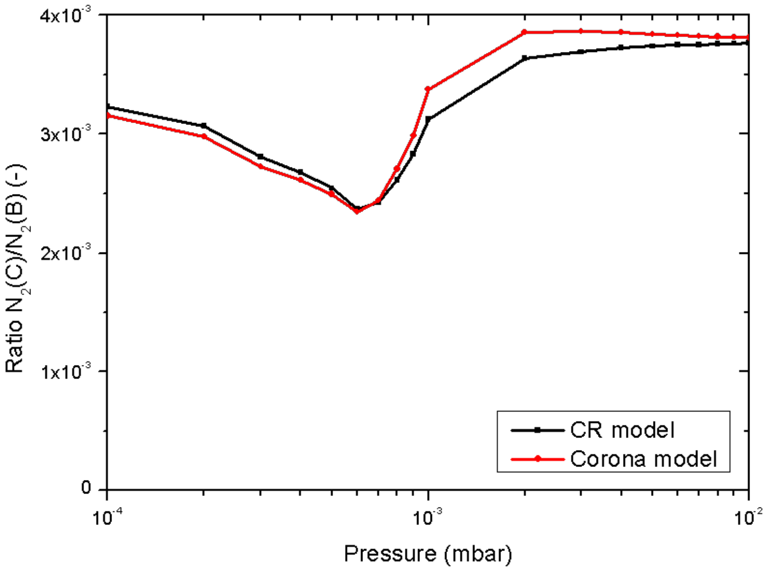

Figure 3.21: Evolution with pressure of the ratio of the radiative states $N_2(C)$ and $N_2(B)$ with the CR and corona models, with a beam-Maxwell EEDF.

shown in figure (3.21). Both models ratios, using T_e giving quasi-neutrality, highlight the favouring of the $N_2(C)$ state with a reduced electron beam energy. In fact, in the pressure range $10^{-4} - 6 \cdot 10^{-4}$ mbar, the beam energy is above 18 eV. The diminution of the ratio is the consequence of the diminution of T_e of the Maxwellian bulk. Then the electron beam energy approaches 15 eV, favouring more and more the reaction rate of reaction (3) of the table (3.4), increasing the ratio.

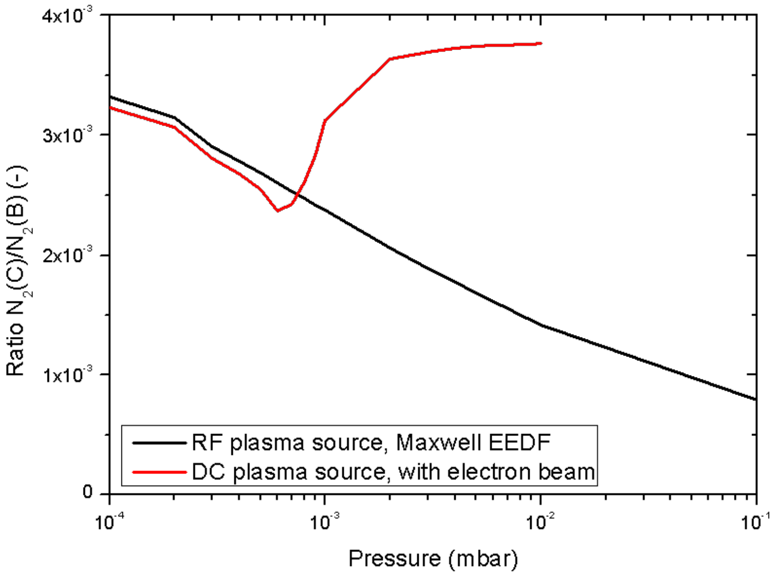

Figure 3.22: Comparison of the ratio between the two EEDFs with the CR model.

The figure (3.22) presents the comparison of the ratio $N_2(C)/N_2(B)$ using the CR model with both plasma sources, i.e. both EEDFs. The evolution with pressure in the range $10^{-4} - 6 \cdot 10^{-4}$ mbar is the same, as T_e decreases in both cases and the electron beam energy is above 18 eV. Above $p = 6 \cdot 10^{-4}$ mbar, in the DC case, the beam energy is favouring the $N_2(C)$ state excitation, leading to an increase of the ratio. At low pressures, due to the ionisation by the electron beam, the temperature of the bulk Maxwellian in the DC case is lower than the temperature in the Maxwell EEDF, this explains the slight difference on the ratio.

Conclusion

The CR model was implemented to calculate the densities of the non-radiative states. The reactions occurring in the low pressure range used in this work were listed and solved together to set balance equations for each state. It appears that the quasi-neutrality condition was not reached with T_e from the simple particle balance model, thus a new set of T_e was determined for both EEDFs, solving for self-consistent neutrality in the plasma. The density of atomic nitrogen is in the order of the one of the metastable $N_2(A)$, greater than the electron density. Both EEDFs give different results for the ratio between the radiative states because of the presence of the high-energy electron beam.

3.5 Adding gallium to both models

The models were modified to add reactions occurring with the admixture of Ga. The gallium is injected outside the plasma source, but due to the low pressure regime, there is no interaction between the nitrogen molecule and the Ga atoms. The Ga interacts with the electrons of the plasma, making excitation and ionisation of the Ga. The cross sections of these two processes are shown in figure (3.3). The threshold for electron excitation is 3.1 eV and for the ionisation 6 eV, meaning that the metastable $N_2(A)$ itself has enough energy to ionise Ga. The most part of the EEDFs is below 6 eV, leading to the excitation of the Ga. The principal interactions between Ga and nitrogen take place on the reactor surfaces.

In the corona model, the added balance equation for the Ga is

$$n_{Ga^*} = \frac{n_e n_{g,Ga} k_{exc,Ga}}{\sum A_{Ga^*}} \tag{3.21}$$

with $n_{g,Ga}$ the initial density of the Ga, fixed to correspond to a BEP of $2 \cdot 10^{-6}$ mbar, corresponding to typical experimental conditions, $k_{exc,Ga}$ the reaction rate for the excitation of Ga, calculated using equation (3.1), and $\sum A_{Ga^*}$ the sum of the Einstein coefficients for spontaneous emission of the Ga. The plasma parameters (n_e and T_e) are taken from the particle balance models and $E_b = 20$ eV (with the beam-Maxwell EEDF), as in figures (3.14) and (3.15).

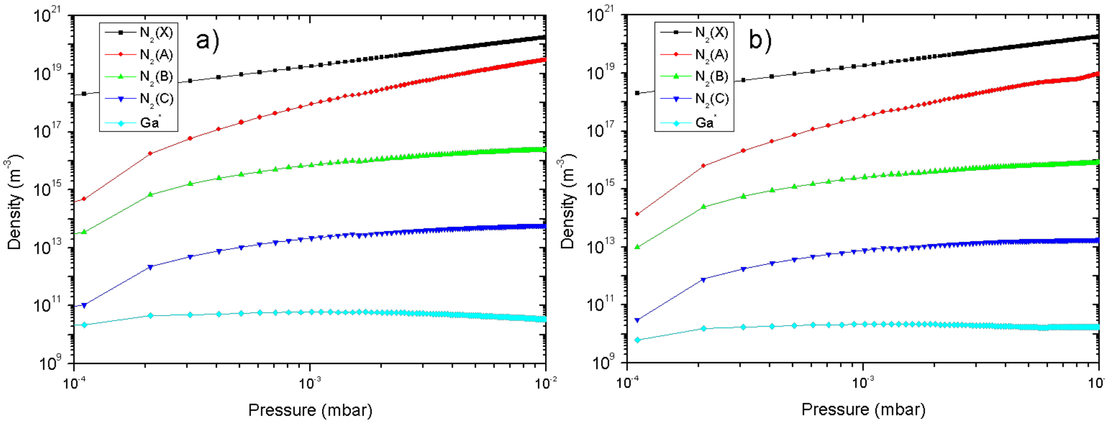

Figure 3.23: Excited states and ground state densities obtained by the corona model including the excited gallium, with the T_e and n_e from the particle balance models, with *(a)* Maxwell EEDF and *(b)* beam-Maxwell EEDF with $E_b = 20$ eV.

Figure (3.23) presents the evolution with the nitrogen pressure of the excited species, found with the corona model, with the two different EEDFs. As expected from the low proportion of Ga in the mixture, the excited gallium is found to be the lowest excited state density. The profile with increasing pressure is more flat, even decreasing because of the decreasing proportion of Ga in the mixture, due to the lowering of the mean free path of the fixed outcoming flux of Ga. The maximum of the density is reached at about 10^{-3} mbar of nitrogen, in both cases. This density is about three times lower with the beam-Maxwell EEDF, due to the lower T_e. The electron beam has no influence on the shape, nor on the density of the excited Ga, because the cross section for the electron impact excitation is relatively flat, even at low energy (see figure (3.3)).

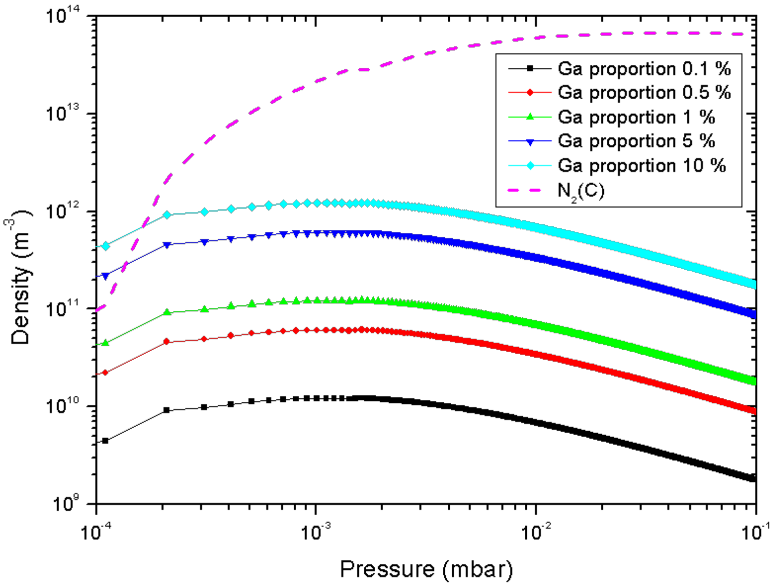

Figure 3.24: Excited Ga density with increasing proportion of neutral Ga in nitrogen, as a function of nitrogen pressure, using pure Maxwell EEDF.

The variation of the cell heating can be simulated by changing the initial amount of Ga in the mixture. The figure (3.24) presents the evolution of the excited gallium density with pressure, with increasing the proportion of Ga in the nitrogen. As the initial density of neutral Ga increases, the density of excited Ga increases also keeping the same shape. On the chart, the N_2(C) density is also shown to demonstrate the gap between nitrogen and Ga excitations. The nitrogen excited state is higher than the excited Ga, except for low nitrogen pressure and high Ga proportion, even if the cross section of the excitation of Ga is greater than the one of the nitrogen. This highlights the importance of the density of the precursor.

#	Reactions	k, A or D Maxwell	k, A or D beam-Maxwell
(1)	$e+Ga \rightarrow e+Ga^*$	$1.507\cdot10^{-14}$ m^{3}s^{-1}	$5.893\cdot10^{-15}$ m^{3}s^{-1}
(2)	$e+Ga \rightarrow 2e+Ga^+$	$1.422\cdot10^{-14}$ m^{3}s^{-1}	$5.442\cdot10^{-15}$ m^{3}s^{-1}
(3)	$Ga^* \rightarrow Ga+h\nu$	$7.15\cdot10^{7}$ s^{-1}	$7.15\cdot10^{7}$ s^{-1}
(4)	$Ga^+ \xrightarrow{wall} Ga$	1643 m^{2}s^{-1}	1643 m^{2}s^{-1}

Table 3.5: Reactions with Ga added to the CR model, with the corresponding k's with both EEDFs, same as in table (3.4).

In the CR model, some reactions were added in order to simulate the collisions of the Ga with the electrons. The reactions added are shown in table (3.5) with the reaction rates of both EEDFs considered. The balance equations resulting from the 20 reactions composing the CR model have been solved for each state of nitrogen and gallium, and the evolution with nitrogen pressure is shown in figures (3.25) and (3.26), in the case of a Maxwellian and beam-Maxwellian EEDF, respectively. As no reaction including nitrogen has been added, the nitrogen species densities are the same as before, as the reactions linking N_2 and Ga occur on the surfaces. The excited gallium density is the lowest, showing a similar profile as for the corona model, but the absolute density is reduced. The neutral Ga density increases linearly because the losses by diffusion increase with the nitrogen pressure (scattering), reducing the diffusion coefficient. The ionised Ga density shows a different evolution than the excited one. From about $6 \cdot 10^{-4}$ mbar, the increase of the ionised Ga density is reduced, due to the lowering of the T_e and n_e. The ion composition of the plasma is not influenced by the presence of the gallium, as it can seen on the figure. In fact, at the minimum of n_e, the Ga ion density is more than two orders of magnitude lower, which represents less than 1%. With the DC plasma source EEDF, the picture is identical, with a stabilisation of the Ga ion density from about 10^{-3} mbar of nitrogen, due to the stabilisation of the plasma parameters.

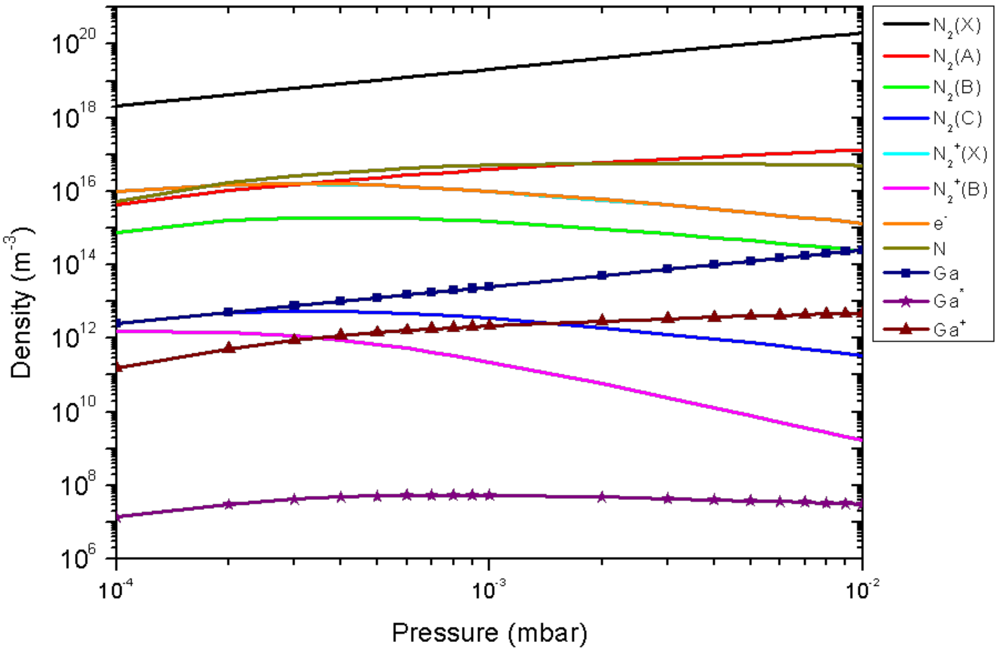

Figure 3.25: Evolution with pressure of the species from the CR model, including the gallium, with a pure Maxwell distribution.

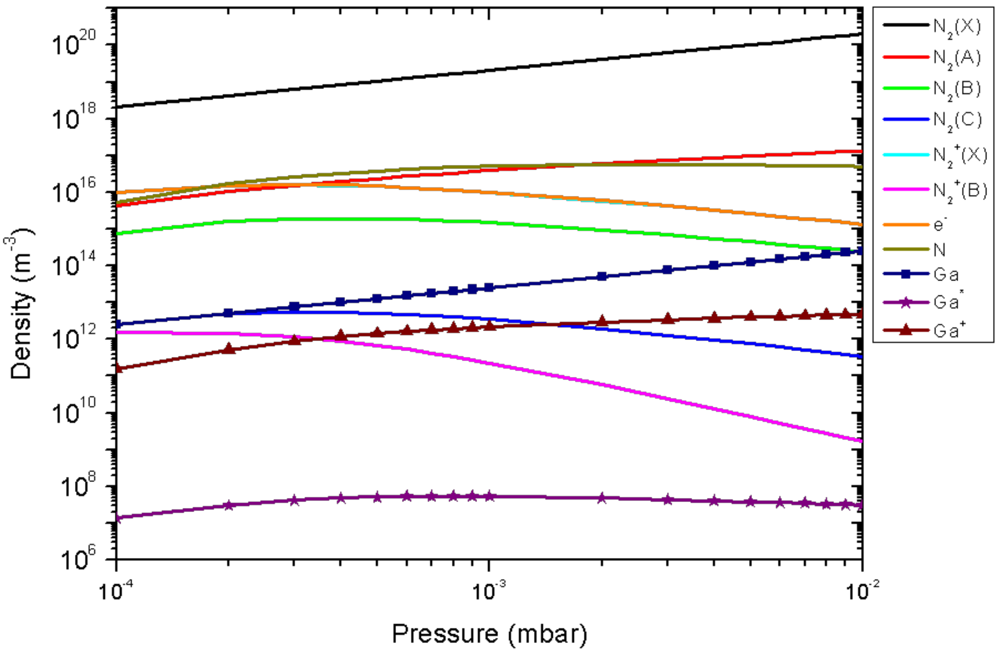

Figure 3.26: Evolution with pressure of the species from the CR model, including the gallium, with a beam-Maxwell distribution.

3.6 Conclusion

Three models were developed to increase the knowledge of the plasma parameters (particle balance model) and to obtain the plasma composition (corona and CR models). A preliminary discussion on the reaction rates and EEDF has been made, in order to explain the underlying physics occurring in a plasma. Due to the low pressure regime imposed by the use of effusion cells for the evaporation of Ga, only electron impact processes contribute to the change in composition of nitrogen plasma. Maxwellian EEDF are seen with the RF plasma source whereas a beam-Maxwellian distribution is found with the DC plasma source, as it will be highlighted in the next chapters.

The presence of the electron beam has only an effect on the plasma density, because the energy of the beam is generally much higher than the maximum of the cross section of the electronic states excitation. It is predicted in the models that the composition of the plasma is similar with both EEDFs and the evolution with pressure has the same trend, because the reaction rates evolve the same with the EEDF parameters and are similar for every excitation. The plasma composition is robust in this pressure range, because the cross sections for the excitation of the states are very similar (figure (3.2)), only the threshold energies vary. The electron temperatures found with the CR model are not varying much over 10^{-3} mbar, explaining also the unchanging composition.

The electron temperatures found with the particle balance model and used with the CR model showed that the quasi-neutrality condition for a plasma is not respected, with both EEDFs. This led to a new set of T_e, based on the reactions occurring in low pressure plasmas. The temperatures determined in this way are lower over the pressure range, due to the other channels leading to the ionisation of the molecule and requiring lower energy, such as the ionisation from the metastable state. However, the evolution with pressure is similar.

The Ga cross sections exhibit a different order of magnitude and a different shape, allowing a change in behaviour with the electron beam. Even with a tunable EEDF, such as the beam-Maxwell distribution, it has been shown that the composition of the nitrogen in the plasma is not changed. This can make such plasmas interesting for industrial applications, where the plasma is used as a tool, with a robust behaviour of the composition. However this also means that the technique is not flexible; it is not suitable for optimisation.

4 RF plasma source: Experimental results

This chapter is devoted to the experimental characterisation of nitrogen plasmas created with the RF plasma source in the deposition reactor using two configurations, with and without the extraction grid. The effect of the grid removal is to increase the plasma density, without changing the composition. The plasma behaviour will be discussed in view of the nitrogen pressure and RF power applied, the two major external parameters. The plasma parameters will be compared to the predictions of the models presented in the previous chapter. Langmuir probe measurements will give the behaviour of the electron temperature (T_e) and plasma density (n_i) with the external parameters, and optical emission spectroscopy (OES) is used to analyse the plasma composition. Both configurations will be compared in order to determine which one is the more adapted to obtain the optimal plasma composition for the deposition of GaN.

4.1 RF plasma source with extraction grid

The plasma generation is made in a small volume with close grounded walls. The gas flow and low pressure lead to a high diffusivity, and the plasma expands in the chamber through the grid holes. Typical spectra in these conditions are presented in figure (4.1). To cancel the effects of the different integration times, the spectra are normalised to the intensity of the 747.5 nm line, corresponding to a first positive band (arbitrary chosen wavelength). The figure shows the optical spectrum for *(a)* a pure nitrogen plasma and *(b)* a plasma used to grow GaN with the same nitrogen flow, and a Ga beam equivalent pressure (BEP) of $2.07 \cdot 10^{-6}$ mbar.

It is seen that the excitation pattern of the nitrogen is similar in both plasma conditions, and that the spectrum is dominated by the light emission of the Ga if it is present in the mixture. The light emission from the N_2(C) states, below 400 nm, is also slightly lower with respect to the one from the N_2(B) state in presence of Ga.

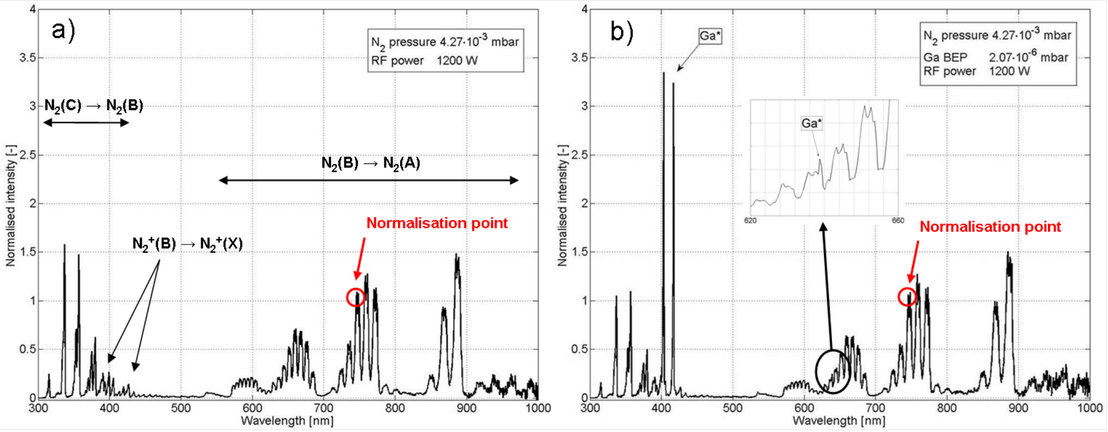

Figure 4.1: Spectra of the plasma near the substrate in *(a)* a pure nitrogen plasma at $4.27 \cdot 10^{-3}$ mbar and *(b)* a plasma with the same nitrogen pressure, but with Ga added. Both spectra are normalised at the 747.5 nm wavelength (indicated with red circles).

4.1.1 Evolution with pressure

To investigate changes in the plasma composition, the first parameter which was varied is the gas pressure, as its impact on the reaction rates is supposed to be high through T_e variation. As mentioned in chapter 1 the work pressure regime is limited by the use of effusion cells. To obtain sufficient Ga atoms for the growth on the substrate, the gas pressure must be maintained between 10^{-4} and 10^{-2} mbar. Figure (4.2) presents the evolution with pressure of *(a)* the total emission light intensities of the electronic states of nitrogen and *(b)* the ratio $\mathrm{I}_C/\mathrm{I}_B$. This figure shows that most of the light intensity is coming from the N_2(B) state. The observed low total light intensity of the excited molecular ion is caused by the low ionisation generally found at such pressures. In fact the plasma density is in the order of 10^{15} m^{-3} (see below Langmuir measurements, figure (4.3)), whereas the neutral gas density is around 10^{19} m^{-3}. The high energy threshold of the cross section for direct ionisation from the ground state (19.2 eV, figure (3.2)) and the low ion density with respect to the neutral gas density leads to the observed weak light intensity.

The composition does not vary much over the pressure regime, as the total light intensities are quite stable above $8 \cdot 10^{-4}$ mbar. The plasma is mainly composed of the metastable state N_2(A), due to de-excitation from the N_2(B) state. Atomic nitrogen is not seen with this technique, because the light intensity is very small for this specie, within the noise of the measured signals. From the evolution of the radiative states, in particular from the ratio $\mathrm{I}_C/\mathrm{I}_B$, it can be seen that T_e decreases with pressure. In fact the fast decay of the ratio indicates that the N_2(B) state is favoured above $8 \cdot 10^{-4}$ mbar, and that T_e remains about stable, as indicated by the ratio.

Langmuir probe I-V curve analysis has been presented earlier (chapter 2), and showed a

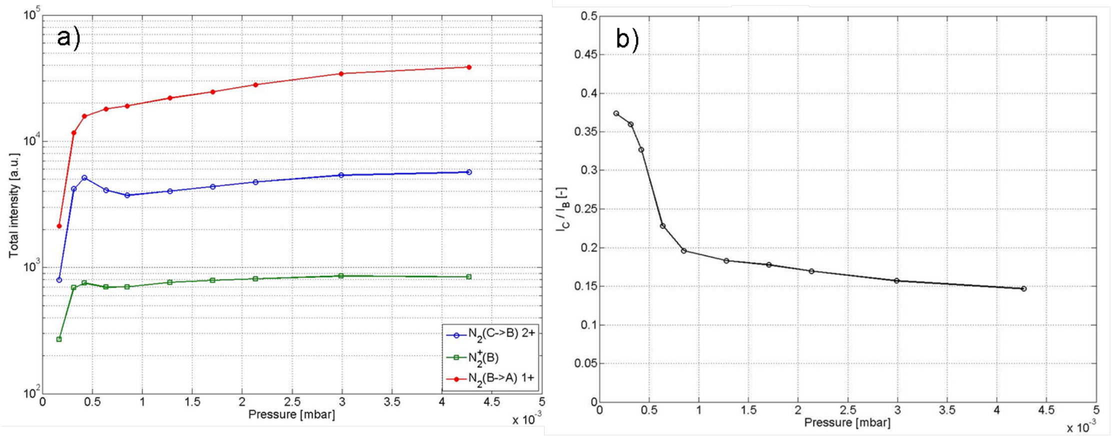

Figure 4.2: Behaviour as a function of the pressure in the deposition reactor of *(a)* the total emission intensities of the main electronic nitrogen states and *(b)* the ratio I_C/I_B, RF power 1200 W.

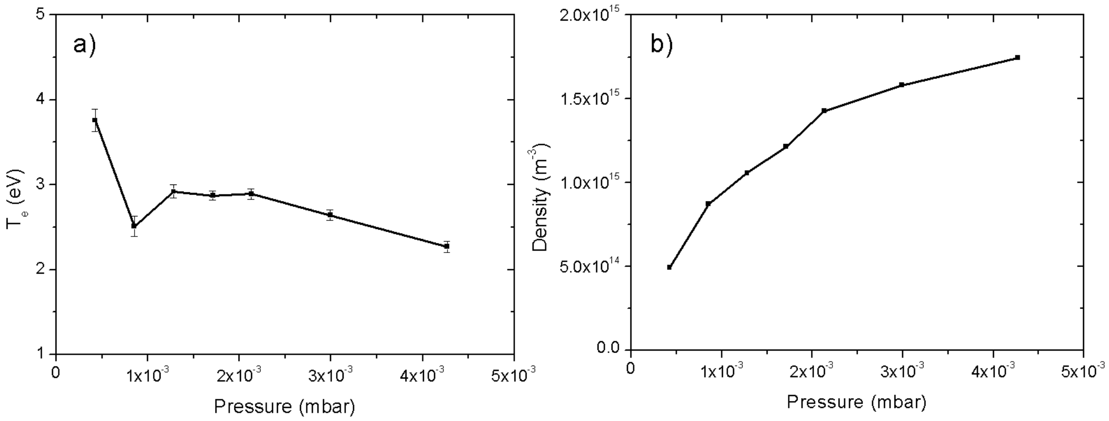

Figure 4.3: Behaviour as a function of the pressure in the deposition reactor of *(a)* the electron temperature of the Maxwell distribution and *(b)* the plasma density outside the source, from the ion saturation current, RF power 1200 W.

Maxwell EEDF with this plasma source. The behaviour of the two extracted parameters (T_e and n_i) as a function of the pressure are shown in figure (4.3). As predicted by the particle balance and CR models and seen by the total light intensity ratio, T_e decreases with pressure. The values of T_e are below 4 eV and the pressure regime used here leads to a slow decrease of T_e, and a plasma density varying by a factor of 3 over a pressure range increasing by one order of magnitude. The total light intensities of N_2(C) and N_2^+(B) at $5 \cdot 10^{-4}$ mbar and $4 \cdot 10^{-3}$ mbar are similar, whereas the N_2(B) light intensity increased by a factor of 3. The variation of T_e and n_i can explain this behaviour of the light intensities. It can also be noticed that the error bars on T_e are small.

The experimental T_e can be compared with the predictions of the particle balance and CR models. Langmuir measurements show that the EEDF is within the experimental error a Maxwell distribution, as seen on figure (2.3). T_e comparison between the models and the experiment is shown in figure (4.4). The models predict a decreasing T_e with the pressure, which is also the case experimentally. The three curves (lines) shown in the figure represent the models. The two lines in solid are the particle balance models, assuming the creation of the ions in the source volume, separated from the reactor volume by the grid, and the losses by Bohm flux to the source walls (blue, equation (3.5)), and assuming ion creation in the whole reactor volume (source and chamber) with losses to all the walls of the reactor (red, equation (3.6)). The dashed line represents the CR model T_e leading to the quasi-neutrality.

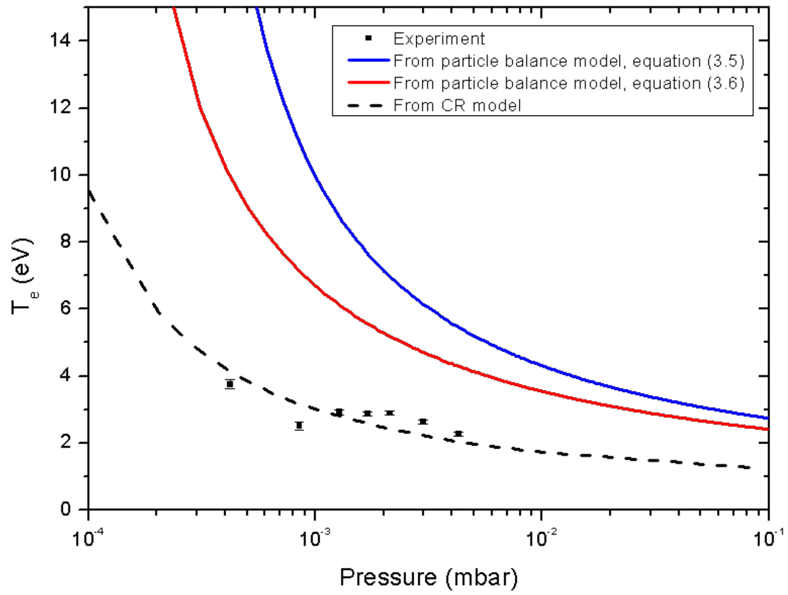

Figure 4.4: Comparison of T_e found with the different models and the experimental ones.

The particle balance model predicts a higher temperature than the measured one, with both creation volumes tested. The CR model T_e fits the measured ones pretty well. The good agreement between the measurements and the CR model highlights that the relevant processes occurring in the plasma have been identified, to explain the T_e pressure behaviour.

The plasma composition is compared to the models through the ratio of density of N_2(C) and N_2(B) states in figure (4.5). Also shown is the ratio with T_e found with the CR model (dashed line). To pass from the total light intensity to the density of the state, the use of the lifetime of the state is needed. The corona model uses only the most relevant populating and de-populating processes, whereas the CR model has an exhaustive list of reactions occurring at such low pressures, detailed in the chapter 3.

The first observation on the graph is that the corona and CR models with experimental T_e curves are almost superposed. This suggests that the populating and de-populating processes in the corona model are the dominating ones, and that in the pressure range

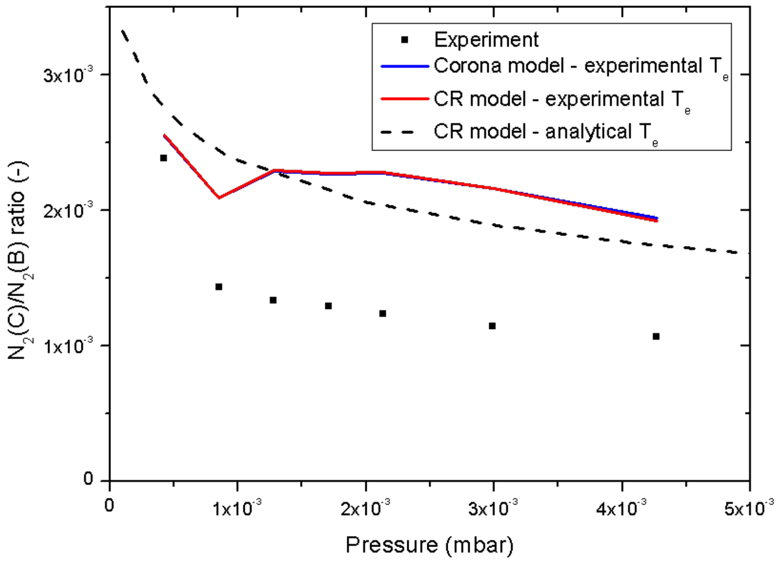

Figure 4.5: Comparison of the $N_2(C)/N_2(B)$ ratio calculated with the different models and the experimental one.

considered, all others can be neglected for the radiative states. The measured ratio $N_2(C)/N_2(B)$ is lower than the ones calculated by the models, indicating that either the measured temperatures are still too high to make the models fit the experimental ratio, or that some errors on the cross sections have been made. However, the pressure dependence of the ratio follows that of the experimental T_e, an indication that the error is more likely in the cross sections. Another source of error can be that the optical fibre collects reflected light from the walls. The Langmuir probe measures a local T_e which is not the case with the optical fibre, because of the aperture angle and because the OES is line-averaged in the reactor.

To test the sensibility of these results on the cross sections, the CR model has been run with an ionisation cross section multiplied by a factor of 3 and with an excitation cross section of the $N_2(C)$ state divided by a factor of 2. These variations of the cross sections values can be found in the literature, depending on the authors, as highlighted in section 3.1. The results on T_e with another ionisation cross section are shown in figure (4.6a) and on the ratio $N_2(C)/N_2(B)$ in figure (4.6b).

The increasing of the ionisation cross section reduces slightly the electron temperature found with the set of reactions, because of the increased ionisation rate. However, the reduction is less marked than the increase of the cross section values. On the contrary, the diminution of the excitation cross section values has a large effect on the density ratio, which is more accurate with this lowering. In this case, the density ratio is about 1.5 times lower than with the cross section from Itikawa, whereas the cross section has been divided by a factor of 2.

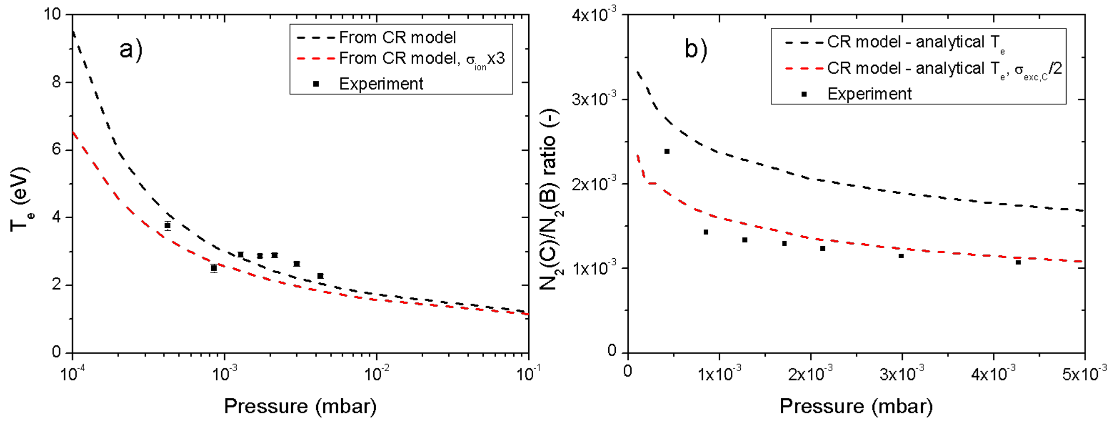

Figure 4.6: *(a)* Effect of the ionisation cross section on the T_e predictions from the CR model, and *(b)* effect of the excitation cross section of the N_2(C) state on the density ratio N_2(C)/N_2(B).

4.1.2 Evolution with power

As the pressure has only a limited effect on the plasma composition and density, the variation of the RF power was probed in order to increase the dissociation of the nitrogen molecule.

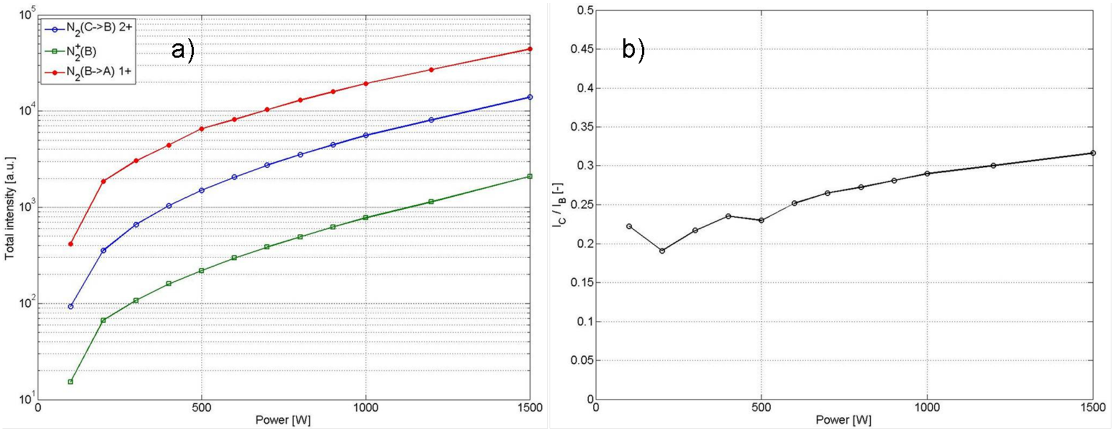

Figure 4.7: Behaviour as a function of the RF power in the deposition reactor of *(a)* the total light intensities of the main electronic nitrogen states and *(b)* the ratio I_C/I_B, pressure $4 \cdot 10^{-4}$ mbar.

The behaviour as a function of the RF power of the total light intensities is shown in figure (4.7). The plasma composition remains unchanged, as the power increase does not affect a particular state; it leads to a global increase of density, confirmed by Langmuir measurements (see figure (4.8)). This let conclude that the shape of the EEDF is not changed by the power increase. The ratio I_C/I_B sightly increases with the RF power, indicating that T_e increases also, but not significantly to modify the plasma composition.

Hardly of these observations, neither the gas pressure nor the RF power has an influence on the plasma composition, only the plasma density is varying with these parameters.

The electron density as a function of the RF power can be seen in figure (4.8a). It is seen that the increase of the plasma density is linear. The increase of the plasma density with power explains the increase of all total light intensities (figure (4.7)).

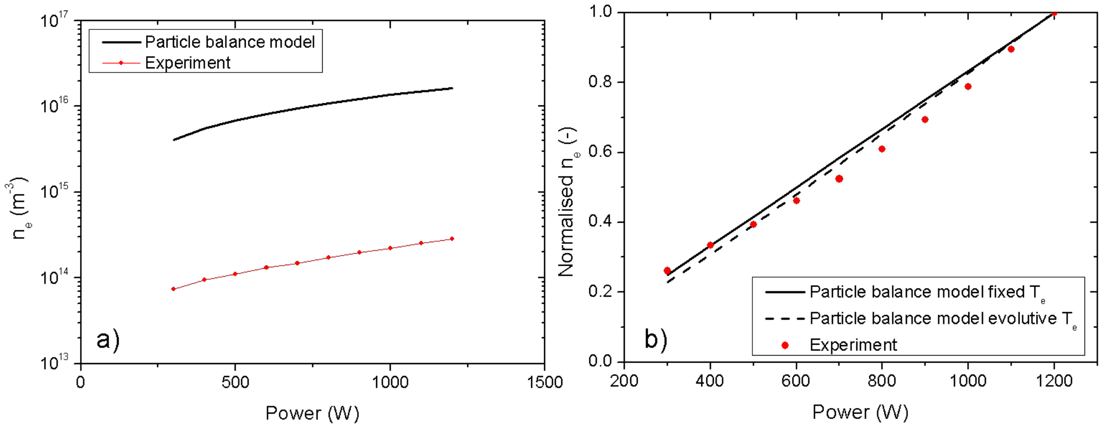

Figure 4.8: Comparison between the particle balance model and the experiment: *(a)* absolute value of n_e and *(b)* evolution of the density with power (normalised to the maximal value). T_e in the model with fixed temperature 3.9 eV, N_2 pressure $4 \cdot 10^{-4}$ mbar.

The experimental plasma density is also compared with the particle balance model in figure (4.8a). The absolute value determined by the model is 100 times higher than the measured one. This difference can be explained by the presence of the grid, which has an optical transparency of about 30% (chapter 1) and by the high diffusivity of the electrons in the chamber. The input of the model is the absorbed power in the discharge, which is different than the RF power set in the plasma source, which also may be a source of error. Nevertheless, the evolution of the plasma density with power shows a good agreement with the particle balance model (figure (4.8b)). The increasing ratio of the light intensities is represented with calculation with an increasing temperature, from 3.9 to 5 eV, and shown in dashed line. The slope of the linear increase is not very different, meaning that T_e has only a low effect on the plasma density in this model.

4.1.3 Uniformity

The gas pressure and the RF power input to the discharge do not influence the plasma composition but only the plasma density. One of the determinant parameter for industrial use of this deposition technique is the uniformity of the plasma. Ion saturation current profiles have been performed using the movable Langmuir probe and are shown in figure (4.9) as a function of the RF power and the gas pressure, normalised to the value of the central point. It can be seen that the uniformity of the ion saturation current along the wafer size is better than 5%. This conclusion is independent of the pressure and the power. Nevertheless the behaviour of the ion saturation current is not symmetrical out of the limits of the wafer, but seems to change slightly with pressure.

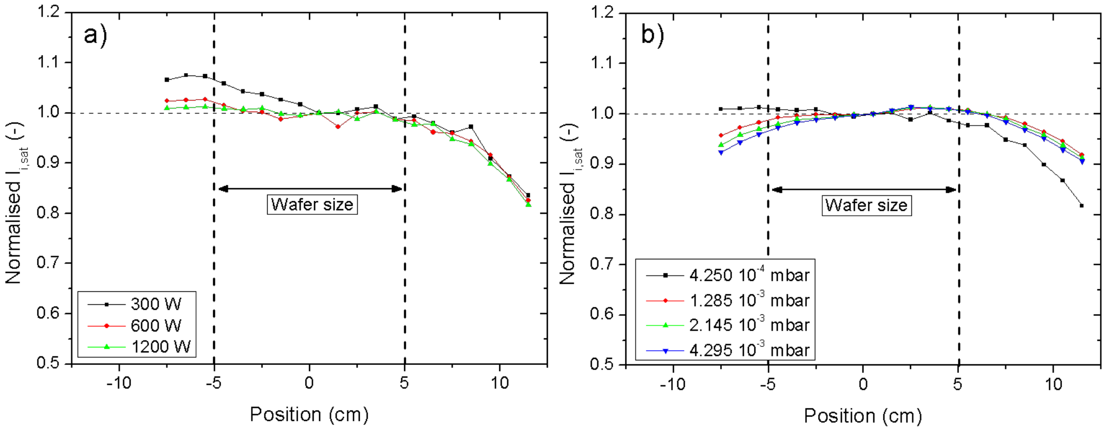

Figure 4.9: Langmuir measurement showing the uniformity of the ion saturation current: *(a)* power scan at a fixed pressure of $4.25 \cdot 10^{-4}$ mbar and *(b)* pressure scan at 1200 W of RF power.

The other plasma parameters, such as electron temperature, plasma and floating potentials, are also quite uniformly distributed over the wafer dimension. The uniformity can be explained by the plasma expansion in the chamber. In fact the diameter of the source is 250 mm, the dimension of the grid is about the same and the holes of the grid are uniformly distributed, leading to an uniform expansion into the chamber.

4.2 RF plasma source without grid

Plasma characterisation has also been made without the extraction grid, allowing an easier transport of the species into the process chamber. This suggests that the electron density must be higher, and thus different densities of the different nitrogen states are expected. The plasma composition could also be different, because more energetic electrons can be brought outside the source volume. As for the configuration with the grid the different plasmas have been characterised by means of OES and Langmuir probe measurements. The analysis of the I-V curves showed a Maxwell EEDF as well. The results in terms of T_e, n_i and plasma composition are compared with the ones using the extraction grid. The predictions of the models are compared with the measurements at the end of this section.

4.2.1 OES comparison

The first comparison is the optical light emission of pure nitrogen, allowing to discuss the composition of the plasma. Figures (4.10) and (4.11) show normalised spectra (to the 747.5 nm wavelength) in both configurations and the evolution with pressure of the main radiative states. The spectra are quite similar but some differences can be seen. A comparison of the low pressure spectrum (figure (4.10a)) indicates that T_e is higher in the configuration without the grid, because the N_2^+(B) bandhead light intensity is greater and the second positive system is lower, with respect to the first positive system. Some excited atomic nitrogen lines are also clearly seen at 750 nm, 800 − 830 nm and 860 nm, indicating a high dissociation degree followed by an excitation of the dissociated molecules.

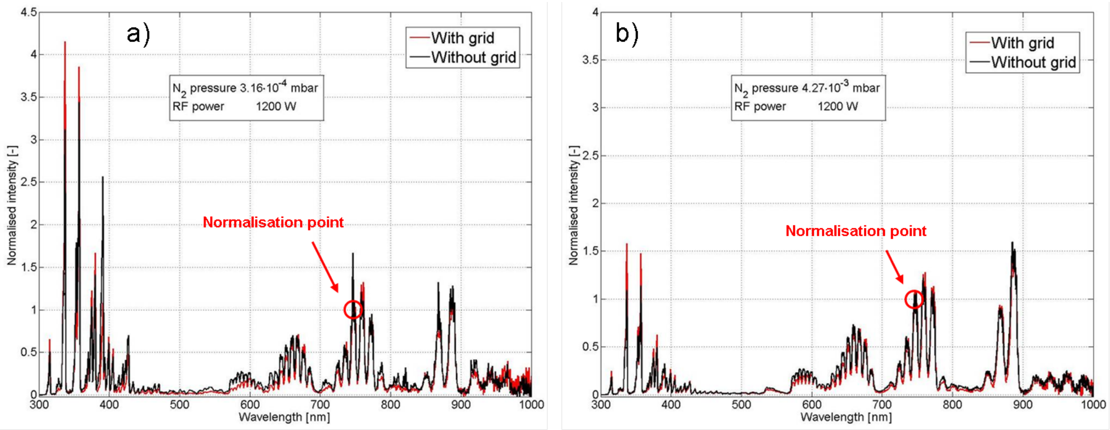

Figure 4.10: Comparison of the emitted light of pure nitrogen plasmas in the configurations with and without the extraction grid at *(a)* $3.16 \cdot 10^{-4}$mbar and *(b)* $4.27 \cdot 10^{-3}$mbar. Both spectra are normalised at the 747.5 nm wavelength (indicated with red circles).

At higher pressures the spectra show less differences, due to the increased neutral gas density. The second positive system light intensity is lower without the grid, indicating a lower T_e. The conclusion out of the comparison of two spectra is that T_e might be greater at low pressure without the grid and lower at high pressure, with respect to the configuration with the grid.

The total light intensities presented in figure (4.11a) as a function of the pressure are one order of magnitude higher than in the configuration with the grid. As the composition is almost the same as in the configuration with the grid, the higher densities of the states are explained by a higher plasma density. The total light intensities have the same evolution with pressure than in the configuration with the grid. Regarding the ratio I_C/I_B, the trend is the same in both configurations. The value of the ratio is in the same order, and the reduction of ratio in the pressure range is also seen without the grid. The transition is less marked, stretched in pressure. T_e seems to be in the same order in both configurations.

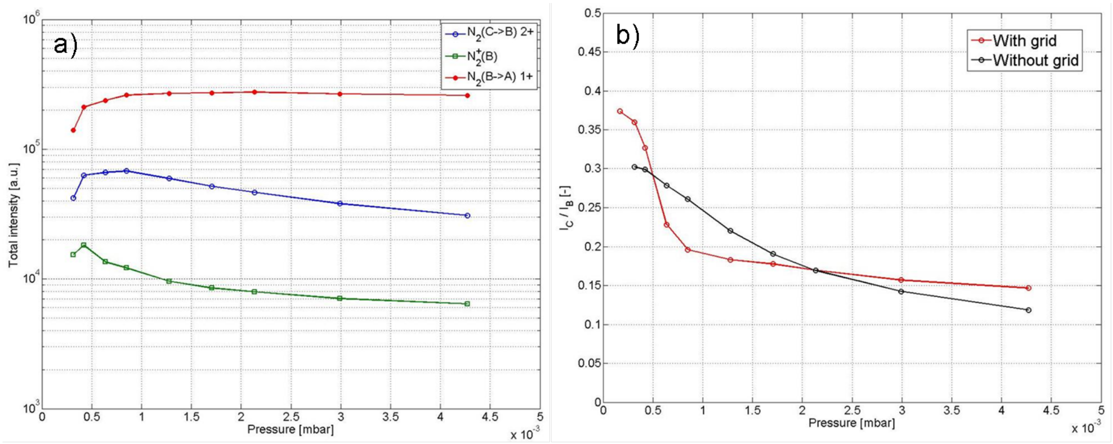

Figure 4.11: *(a)* Radiative states intensities as a function of the pressure in the configuration without the grid and *(b)* comparison of the ratio I_C/I_B with and without the extraction grid. RF power 1200 W.

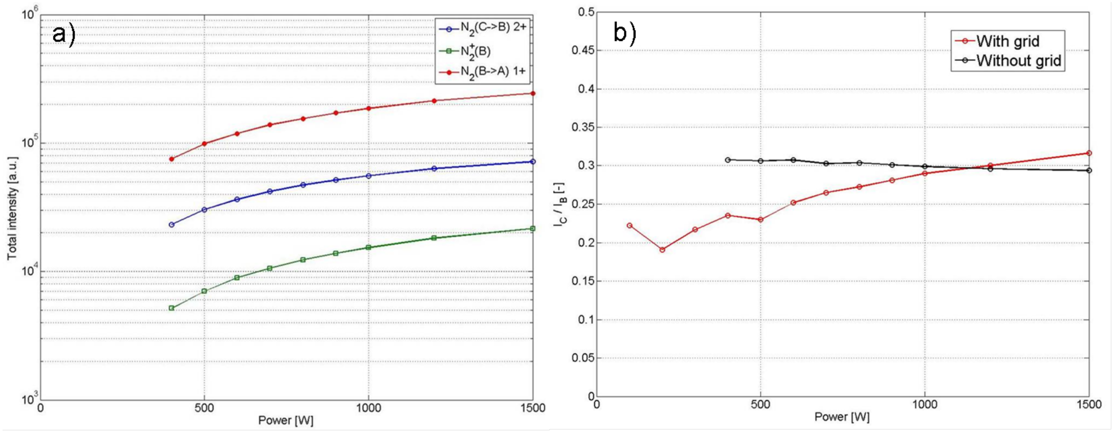

Figure 4.12: *(a)* Total light intensities as a function of power of the radiative states without the extraction grid and *(b)* comparison of the ratio I_C/I_B in both configurations with increasing RF power, N_2 pressure $4 \cdot 10^{-4}$ mbar.

The behaviour as a function of the RF power of the total light intensities and the ratio I_C/I_B is shown in figure (4.12). The total light intensities all increase with the power, indicating that the plasma density is increasing. In fact no particular state seems to be preferred with increasing RF power. This is confirmed by the evolution of the ratio I_C/I_B, which is constant in the power range scanned, a different evolution than with the extraction grid. The reason for this may be that the plasma is not confined in the plasma source because of the grid. The removal of the grid changes the way the plasma expands into the chamber and thus the plasma density, not the plasma composition.

4.2.2 Langmuir probe measurements comparison

The OES comparison showed that the plasma composition is not changed by the removal of the grid. Langmuir probe measurements have been performed to investigate the changes in the EEDF parameter (T_e) and in the plasma density due to the removal of the extraction grid. Figure (4.13) exhibits the variation of T_e and the ion saturation current as a function of the pressure, compared to the configuration with the grid.

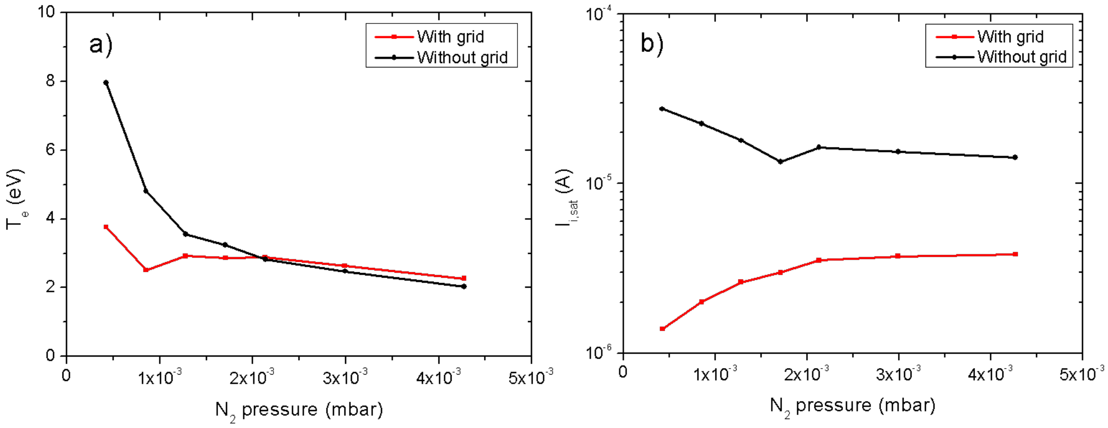

Figure 4.13: Behaviour with pressure and comparison with the configuration with the grid of *(a)* electron temperature and *(b)* ion saturation current, RF power 1200 W.

The behaviour of T_e (figure (4.13a)) follows the same trend as the one with the grid. Below $p = 10^{-3}$ mbar, the temperature is about two times higher without the extraction grid, due to the higher diffusion in the reactor, and T_e are very similar at high pressure. The plasma density is changed with the removal of the grid (figure (4.13b)). The ion saturation current is one order of magnitude higher without the grid below $p = 10^{-3}$ mbar. The evolution with pressure is not the same in both configurations: without the grid, the density decreases with the pressure. At low pressure T_e is high, thus making direct ionisation from the neutral ground state nitrogen molecule. When the pressure is increased, the plasma is confined closer to the source because of the lowered diffusion of the electrons, reducing T_e and thus the ionisation rate at the measurement point. The removal of the grid permits nevertheless to have a higher density, over the all range of pressure, without changing the plasma composition. This feature can be interesting to increase the growth rate of the deposition, or to change the morphology of the layer (see chapter 7).

Ion saturation current as a function of the power in both configurations is shown in figure (4.14). The increase of the light intensity with power is due to the increase of the electron density, not from a change of T_e. The values of the ion saturation current shows that without the grid, the density is higher, about one order of magnitude, over all the RF power range tested. The evolutions shown in figure (4.14b) indicate that the mechanisms of increase in densities are the same in both configurations, and that they

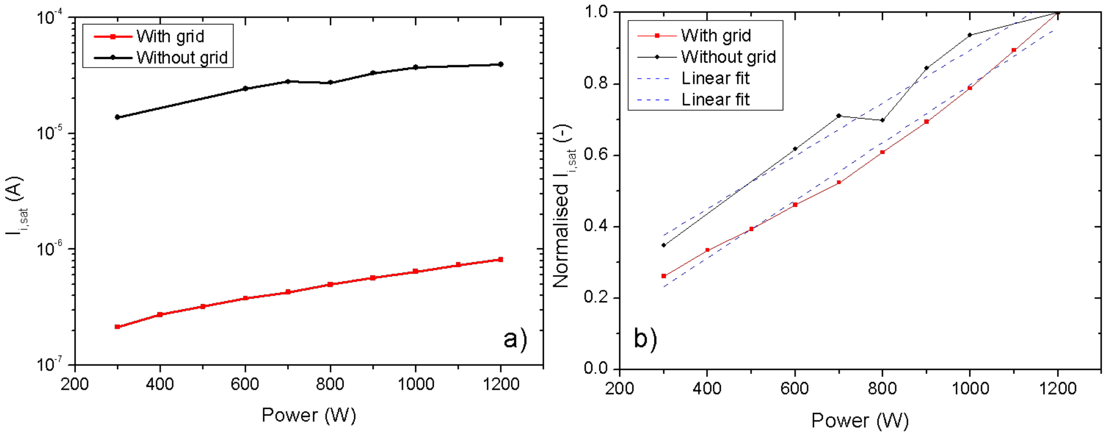

Figure 4.14: Comparison of the ion saturation currents between both configurations *(a)* absolute values and *(b)* normalised evolution, N_2 pressure $4 \cdot 10^{-4}$ mbar.

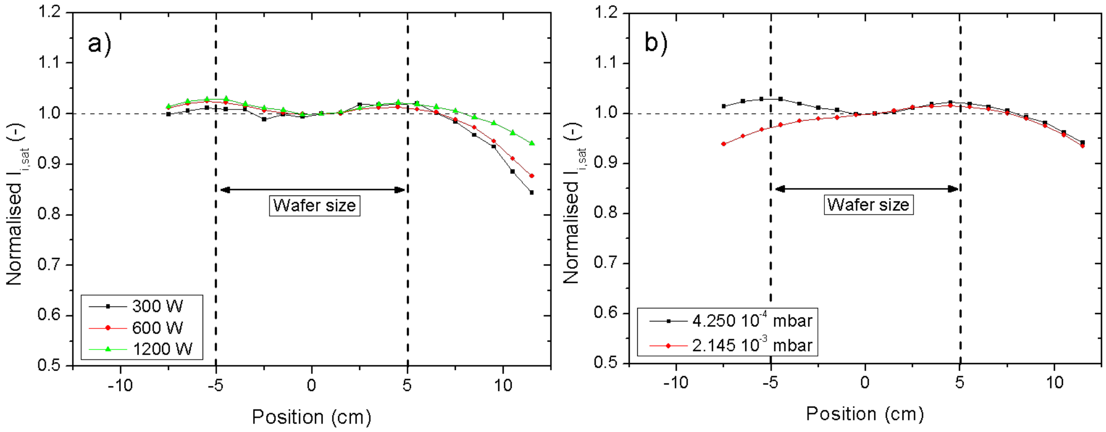

Figure 4.15: Density uniformity, and evolution with *(a)* RF power at $p = 4.25 \cdot 10^{-4}$ mbar and *(b)* pressure with RF power of 1200 W.

are about linear with the RF power. The grid does not affect the density evolution, only the absolute density.

The uniformity of the plasma density in the configuration without the grid has also been probed and the results are shown in figure (4.15), as a function of the RF power and the gas pressure. In both cases the homogeneity is better than 5% over the wafer size, and is not dependent on the gas pressure nor on the power. At low pressure there are two maxima at the edges of the wafer. The shape of the profile might to be the image of the distribution of density inside the plasma source, with maxima on the top of the antenna. The removal of the grid does not affect the uniformity of the density at the height of the substrate. The profile is relatively flat over the source diameter, then the density drops fast. The plasma density is thus increased without changing the plasma composition and uniformity, which is interesting for the industrial application.

4.2.3 Modelling this configuration

The shape of the Langmuir I-V curves indicated a Maxwell EEDF in this configuration. The particle balance model predictions for T_e and n_e will be compared to the experimental values, and they will be used as inputs for the corona model. As in the configuration with the grid, the CR model will be used to determine a set of T_e, guaranteeing the neutrality of the plasma. The second necessary input for this model is n_e, which will be taken from the particle balance model. The plasma composition will be compared with the experiment through the ratio between the N_2(C) and N_2(B) states.

The T_e extracted from the I-V Langmuir probe curves are compared with the particle balance and the CR models in figure (4.16). The shape of the curves is the same, but the predictions of the particle balance model values are still higher than the measured ones. Removing the grid permits to get a better match between the particle balance model hypotheses and the experiment, which is seen by the better match of T_e. The CR model predicts lower temperatures than the measured ones, for $p < 10^{-3}$ mbar, and the match between the predictions and the measurements is good for $p > 10^{-3}$ mbar. Both models give the range for the values of T_e in the pressure range $10^{-4} - 10^{-2}$ mbar.

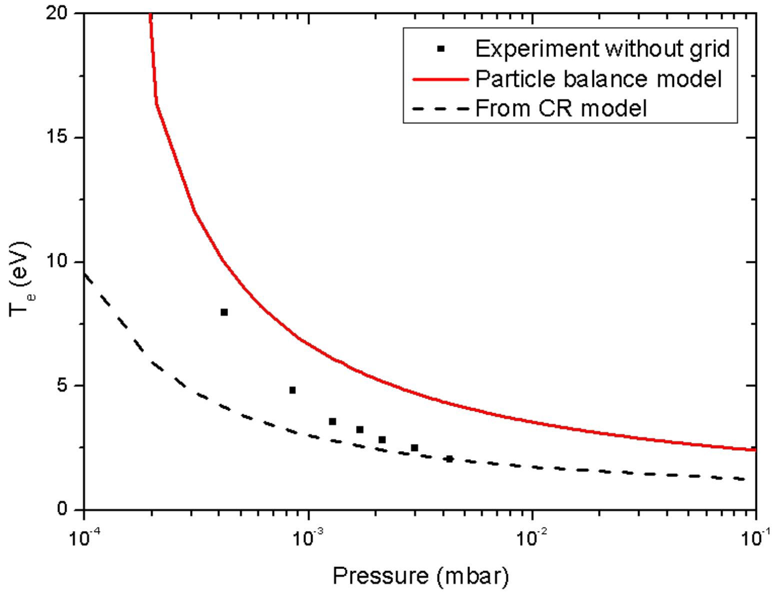

Figure 4.16: Comparison of the electron temperature as a function of the gas pressure obtained with the particle balance and the CR models and the measurements without the extraction grid.

The evolution with pressure of the experimental ratio of the radiative states N_2(B) and N_2(C) and the results of the corona and the CR models are shown in figure (4.17). As in the configuration with the grid, both models using the experimental inputs show identical results, indicating again that the selected processes in the corona model are the dominating processed for the radiative states. The order of magnitude of the ratio

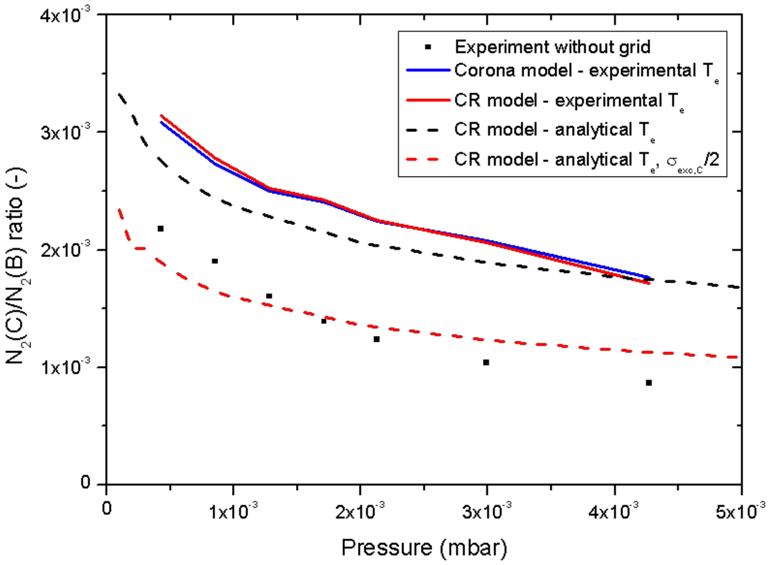

Figure 4.17: Comparison of the ratio $N_2(C)/N_2(B)$ as a function of the gas pressure between the experiment and the models.

is reproduced in this configuration. The global shape of the curve is better reproduced than in the configuration with the grid. This is due to the better match between the evolution of T_e. Nevertheless the models predict a higher ratio, indicating that the $N_2(C)$ is overestimated or the $N_2(B)$ state is underestimated in the models. On the other hand the fibre can collect reflections coming from the walls, leading to a lowering of the experiment ratio. The CR model used with the temperatures giving the quasi-neutrality in the CR model reproduces also the global shape of the ratio, but the absolute value of the ratio still do not match. The values are lower than with the experimental T_e because the found T_e with the model are lower. This suggests that the cross sections for the different excitations may have some error. As found in literature the excitation of the $N_2(C)$ state cross section can be lower by a factor of 2. The curve with these cross section values is also presented in figure (4.17), showing that the ratio is very sensitive to the variations of the cross sections, and that in this case, the modelled ratio is more accurate to fit the experimental ones.

The last plasma parameter which is extracted from the experiment is the plasma density. The evolution with RF power is shown in figure (4.18) in two ways: *(a)* absolute values and *(b)* normalised evolution, with linear fits for the experiment and the model. As the ratio I_C/I_B is constant over the power range (figure (4.12)), T_e has been set constant at $T_e = 8$ eV, the temperature found with the Langmuir probe at the pressure used. The absolute value of the density found with the model is close to the experimental one, better than in the configuration with the grid. The normalised values highlight the linear increase with RF power verified experimentally, as the slopes are close to each other. This justifies *a posteriori* the choice of a constant T_e in the model, and that the ratio

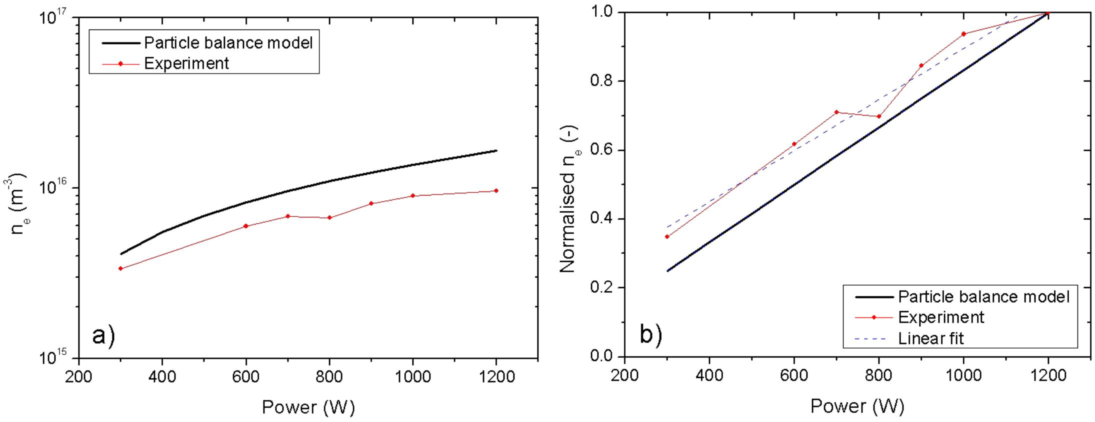

Figure 4.18: Power evolution with comparison between experiment and model of *(a)* absolute electron density with a N_2 pressure of $4.25 \cdot 10^{-4}$ mbar and *(b)* normalised evolution.

I_C/I_B gives a good estimation of the evolution of T_e.

The good agreement between the models and the experiment is again seen in figure (4.19), which compares the evolution with gas pressure of the measured total light intensities of the radiative states, and the densities found with the CR model. The shape of the density curves is well reproduced, except for the excited molecular ion density. The difference of the absolute values of the densities is in the good order of magnitude (factor 10^3 between $N_2(B)$ and $N_2(C)$ densities), confirming that the CR model takes into account the dominant reactions occurring in the plasma.

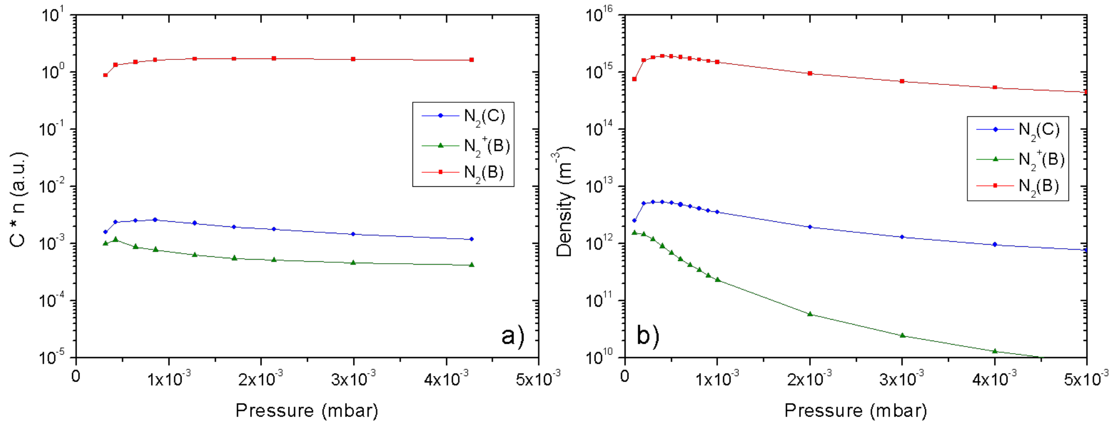

Figure 4.19: Comparison of the evolution with pressure between *(a)* experimental densities through total intensities ($C \cdot n$ in equation (2.5)) and *(b)* modelled densities obtained with the CR model.

4.3 Conclusion

This chapter described the evolution of pure nitrogen RF plasma parameters with the changes of the gas pressure and power, in two source configurations. Due to the effusion cells used to evaporate gallium, the gas pressure regime is restricted to $10^{-4} - 10^{-2}$ mbar. This has a great influence on the plasma: The energy distribution remains close to a Maxwellian one, with a varying electron temperature, as predicted by the developed particle balance model. Nevertheless, the plasma composition is almost unchanged in the gas pressure range, even if the grid is removed. At low gas pressure, the reaction rates are high but the neutral gas density is low and the inverse is found at high gas pressure. The power has only a very small influence on the electron temperature, and thus on the plasma composition. The plasma density outside the source is one order of magnitude lower with the extraction grid and shows a very good uniformity at the substrate height (better than 5%), in both source configurations. The plasma density varies linearly with the RF power, as described by the particle balance model. A way to change the plasma composition would be to increase the gas pressure up to the millibar range, to have some heavy particles collisions, as N_2-N_2 collisions. This would then limit the density of Ga reaching the substrate because of its screening.

The comparison between the experiment and the models highlights that the main processes occurring in the plasma have been identified. The particle balance model predictions in terms of electron temperature are overestimated, but the plasma density predictions are more accurate, at least for the configuration without the grid. The corona and CR models show good agreement in terms of ratio $N_2(C)/N_2(B)$, and the electron temperatures from the CR model are in very good agreement with the measurements in the configuration with the grid.

5 DC plasma source: Experimental results

The previous chapter showed that the plasma composition could not be changed with the variation of the gas pressure or the RF power using the RF plasma source in two different configurations. To try to influence the plasma composition, the plasma source was changed to a DC plasma source (see chapter 1 for details), because it can create a different resulting EEDF. The effects on the new EEDF and the plasma density on the nitrogen plasma will be investigated. The use of the DC plasma source adds also a new external parameter, the magnetic field. This chapter will present the plasma characterisation results obtained with the two reactors running with a DC plasma source. A large part of the chapter will be devoted to the uniformity of the plasma, an important issue for industrial use of the deposition technique, for which the different anode concepts were developed (see figure (1.8)).

Figure (5.1) shows an example of OES spectra, from *(a)* pure nitrogen plasma and *(b)* GaN growth plasma at a different nitrogen pressure, in the deposition configuration: grounded circular anode close to the plasma source (number 2. in figure (1.8)). A difference between the two spectra is the nitrogen pressure, which is higher in the case with Ga, explaining the reduction of the N_2(C) emission intensity and the change in the band emission pattern. Note also that the Ga BEP in this example is two times lower than with the RF plasma source example. The spectrum from pure nitrogen plasma is very similar with the one with the RF plasma source, but has some differences due to the presence of the electron beam. This latter makes the molecular ion (N_2^+(B)) and N_2(C) emission bands more pronounced. Adding the Ga leads to a different pattern compared to the RF plasma source. In fact the light emission bands from the N_2(B) state are different, due to the pressure increase, and there is a large reduction of the high energetic radiative states (N_2^+(B) and N_2(C)). The molecular ion density is reduced by the presence of the Ga, due to the low ionisation energy of the Ga, there is a partial replacement of the ion density by Ga^+ ions. The two visible lines of Ga^* in the spectrum are not dominating the spectra anymore. This can be due to presence of the high energy electron beam, which lowers the bulk T_e and thus not favouring the Ga excitation.

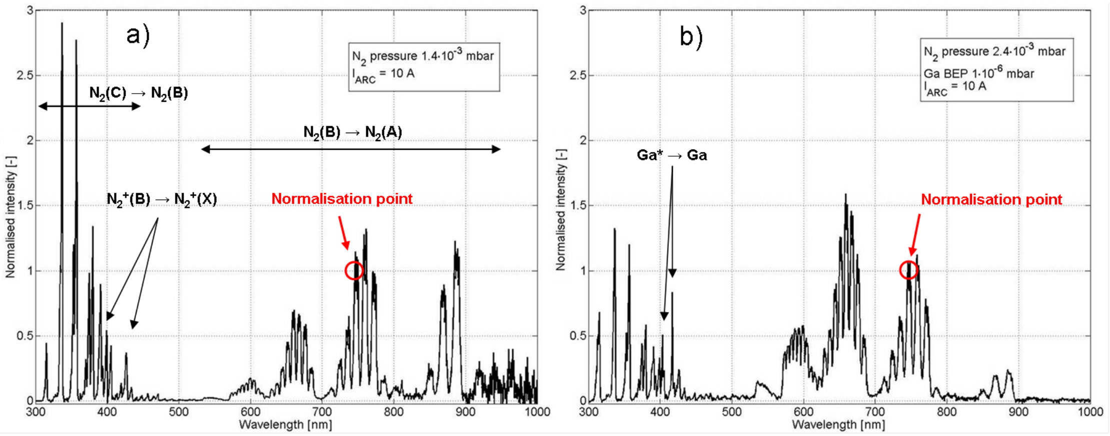

Figure 5.1: Spectra of the plasma near the substrate with a DC plasma source in *(a)* pure nitrogen plasma and *(b)* a growth plasma without argon and a Ga BEP of 10^{-6} mbar, B= 0 G. Both spectra are normalised to the 747.5 nm wavelength.

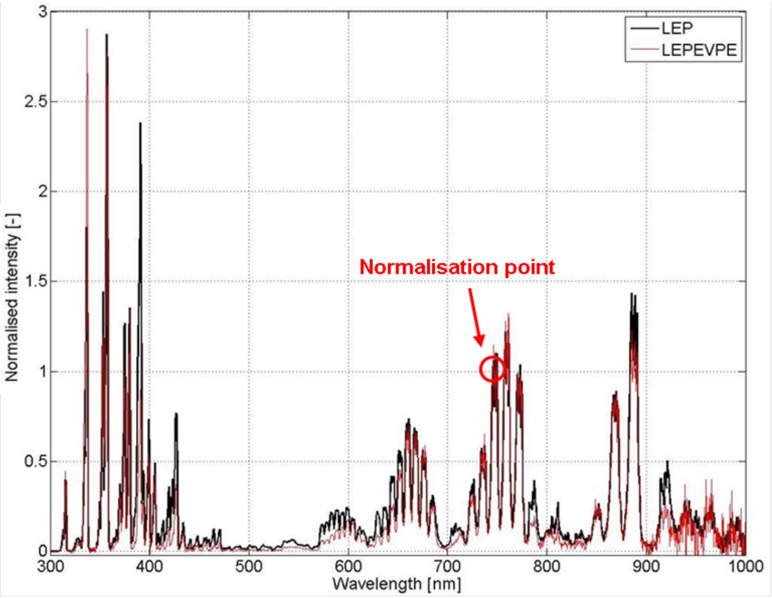

Figure 5.2: OES comparison of the two DC plasma sources: LEPEVPE (deposition system) and LEP device, normalised to the 747.5 nm wavelength.

As the LEP device is more convenient for the characterisation of the plasma and the change of electrical configurations, it is important to see if the two DC plasma sources lead to the same plasma. Figure (5.2) presents a comparison of two plasmas made with the same parameters (gas pressure, magnetic field and discharge current) in both systems using the same electrical configuration. The composition is very similar, some variations are seen due to a difference in the electron beam energy, because of different separation plates hole diameter and accelerating voltages. In fact, the LEP spectrum presents higher intensities for the $N_2^+(B)$ and lower $N_2(C)$ bands, which can indicate that the electron beam energy is slightly higher in the LEP, favouring the highest energetic state. This observation has been made for some other parameters, but the evolution of the plasma parameters and light intensity with the external parameters is the same (not shown). Therefore it is concluded that the results of the LEP device are applicable for the LEPEVPE deposition system.

5.1 Evolution of the plasma parameters

5.1.1 Evolution with pressure

As with the RF plasma source, the neutral gas pressure is the main parameter which can lead to a change in plasma composition, as it influences the EEDF and with it the plasma plume. The same pressure range than with the RF plasma source will be investigated, as the use of effusion cell limits the pressure range. Figure (5.3) shows the behaviour with pressure of *(a)* the total light intensities of the radiative electronic states and *(b)* the ratio I_C/I_B. The dominant light intensity is the one of the N_2(B) state, as with the RF plasma source.

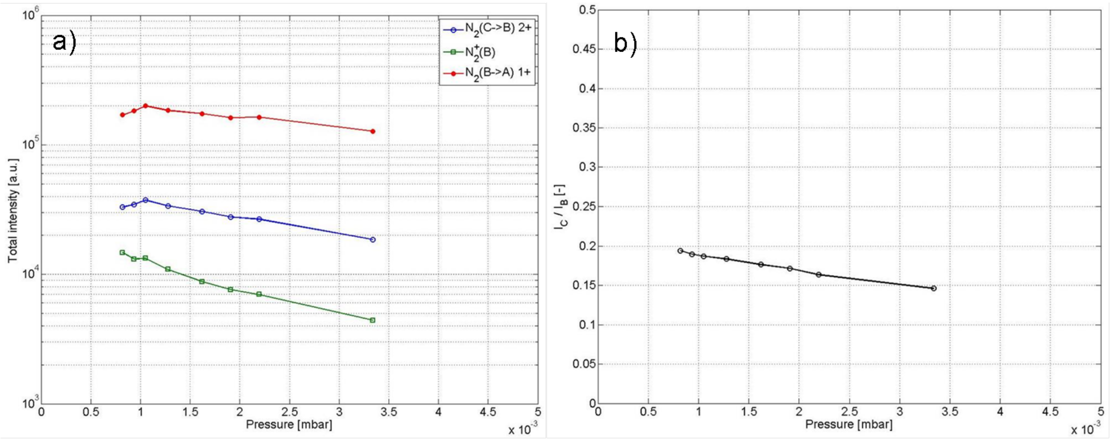

Figure 5.3: Behaviour with pressure of *(a)* total intensities of the main electronic nitrogen states and *(b)* the ratio I_C/I_B, $I_{ARC} = 10$ A, B $= 0$ G.

Another similarity with the RF plasma source is the fact that the plasma composition does not vary in the pressure regime. This is indicated by the total light intensities arrangement: N_2(B), N_2(C) and N_2^+(B) (from most intense to the lowest intensity). The total light intensities of the excited states remain relatively constant in the pressure regime, whereas the one of the molecular ion bands decreases. The decrease can be explained by the fact that the plasma plume (hot dense plasma) is damped quickly with the increase of the neutral gas density (see figure (1.7)). Thus at the measurement zone, there are less energetic electrons making direct ionsiation to the excited molecular ion. The ratio I_C/I_B confirms that T_e decreases with pressure. The ratio is in the same order of magnitude than with the RF plasma source $(0.2-0.15)$, indicating that the DC plasma source leads to about the same plasma composition as the Maxwellian distribution present in the RF plasma source. The pressure seems to be the major factor determining the plasma composition, independently of the plasma source.

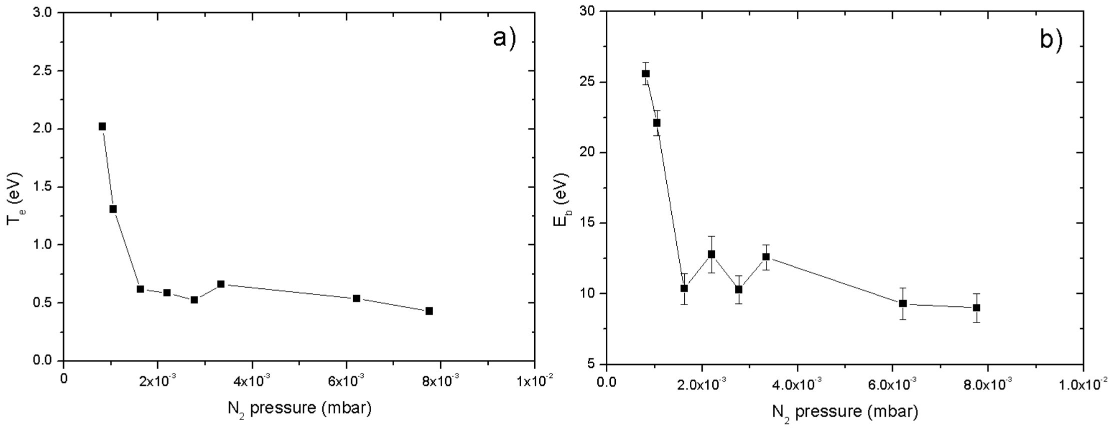

Figure 5.4: Behaviour with pressure of *(a)* the electron temperature of the bulk Maxwellian distribution, with error bars lower than the point size, and *(b)* the electron beam energy. LEP device, grounded circular anode, $I_{ARC} = 10$ A, B $= 0$ G, measured in the centre of the reactor.

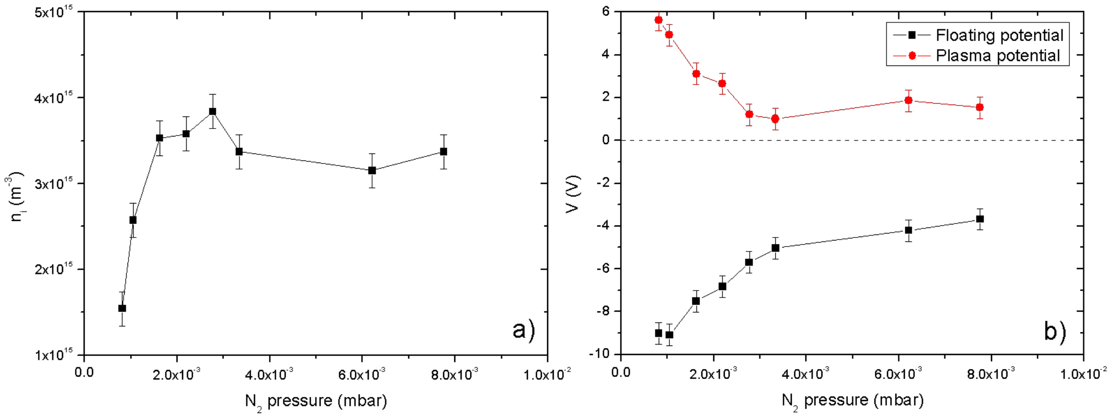

Figure 5.5: Behaviour as a function of the pressure of *(a)* the plasma density, calculated with the T_e of the figure (5.4a), and *(b)* the plasma and floating potentials, extracted from the I-V curves of the Langmuir probe. LEP device, grounded circular anode, $I_{ARC} = 10$ A, B $= 0$ G, measured in the centre of the reactor.

T_e of the bulk Maxwellian distribution and E_b as a function of the pressure are shown in figure (5.4). T_e of the bulk Maxwellian is smaller than with the RF plasma source due to the electron beam and decreases fast with pressure, as well as the electron beam energy. Both plasma parameters are almost constant above a gas pressure of $1.5 \cdot 10^{-3}$ mbar, with a slight decrease, which explains the behaviour of the light intensity ratio I_C/I_B. The electron beam energy is constant at about 10 eV, which corresponds to the maximum of the $N_2(B)$ excitation cross section, and at this energy the value of the cross sections for the excitation of N_2(B) and N_2(C) are similar. The stability of these plasma parameters explain the very similar composition of the plasma in the considered pressure range.

The other parameters that can be extracted from the I-V curve of the Langmuir probe are shown in figure (5.5). The plasma density as a function of the pressure is the same as with the RF plasma source, an increasing density until reaching a saturation. The plasma density is however about three times higher than with the RF plasma source with grid, and in the same order than without the grid. The saturation of the density occurs above a gas pressure of $1.5 \cdot 10^{-3}$ mbar, as also noticed with the other parameters. The floating potential is always negative, indicating that there are energetic electrons present. It is seen that the absolute value of this potential decreases with pressure, which is consistent with the electron beam energy evolution.

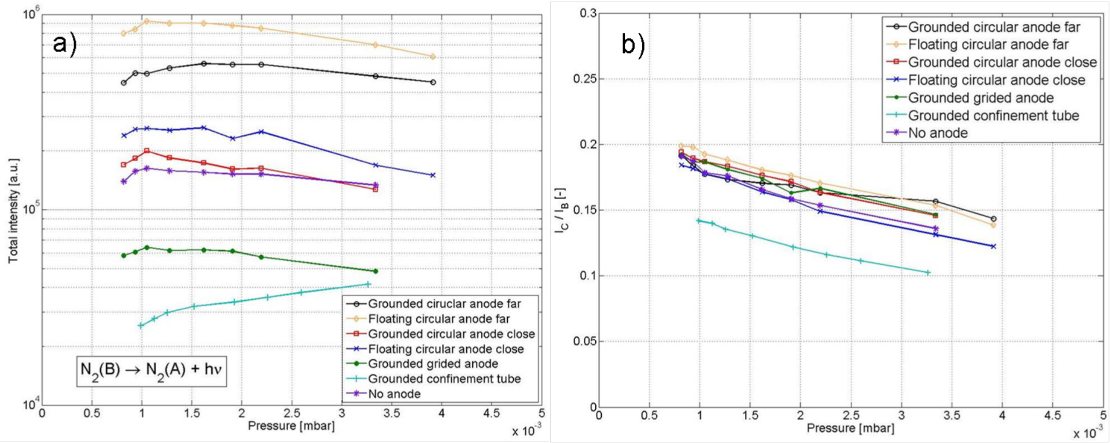

Figure 5.6: OES comparison of the different electrical configurations through *(a)* total light intensity of the N_2(B) state and *(b)* the ratio I_C/I_B, $I_{ARC} = 10$ A, B = 0 G.

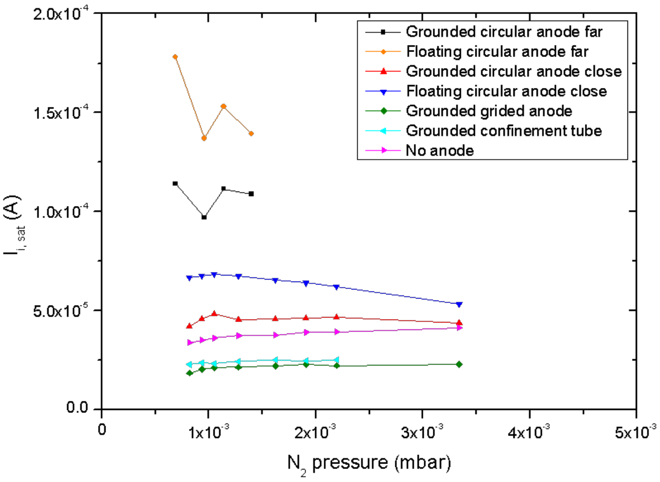

Figure 5.7: Comparison of $I_{i,\, sat}$ evolution with pressure in the different electrical configurations tested in the LEP device, $I_{ARC} = 10$ A, B = 0 G.

The figures (5.6) and (5.7) give a comparison between the electrical configurations tested in the LEP device, through the total light intensity of the N_2(B) state and ion saturation currents, to see changes in plasma density with increasing pressure, and the ratio I_C/I_B, to probe variations of T_e. The behaviour of the light intensity from the N_2(B) state is globally the same with the increasing pressure, except for the configuration with the confinement tube. The variation of the total light intensities between the electrical configurations can be explained by the change in plasma density in the different configurations, as confirmed by the ion saturation current measurements (figure (5.7)). On the ratio chart (figure (5.6b)), only the confinement tube configuration seems to be slightly different. The conclusion from the OES measurements is that the plasma composition is very similar, independently of the electrical configuration or the plasma source, in this pressure range.

In correlation with the figure (5.6), the plasma composition is independent of the electrical configuration, because both EEDF parameters (T_e and E_b) are identical and the evolution with pressure is the same, but the plasma density is sensitive to the electrical arrangement. In fact, the confinement tube and the grid lower the plasma density with respect to the other electrical configurations. Setting the anode floating slightly increases the density, in comparison with the same arrangement with the anode grounded. The discharge current is forced to pass through the anode, whereas if it is grounded, all the chamber acts as an anode and the current can be drawn by the walls, which can be closer than the anode, reducing the plasma density in the centre of the reactor. The ion saturation current and OES measurements permit to draw identical conclusions, thus only OES measurements will be shown up to now.

5.1.2 Evolution with power (discharge current)

The plasma composition cannot be changed with the gas pressure, even with the change of the plasma source. The input power has been varied in order to try to change the electron beam energy, to be able to tune the plasma composition. The important parameter is the discharge current, because the DC voltage applied to sustain the discharge is approximately constant at $40-45$ V. Figure (5.8) presents the behaviour of the total light intensities and the ratio I_C/I_B as functions of I_{ARC}. The increase of the total light intensities is the same for the radiative states, indicating that the plasma composition remains the same. The total light intensities increase linearly with the discharge current, and the ratio I_C/I_B indicates a slight increase of T_e (figure (5.8b)). Increasing the discharge current increases the plasma density but does not change significantly the EEDF.

The increase of the plasma density with the discharge current is confirmed by Langmuir probe measurements (not shown here). The plasma composition is again unchanged by the variation of the input power, even with the presence of the electron beam. The plasma density, as with the RF plasma source, is linearly dependent on the current.

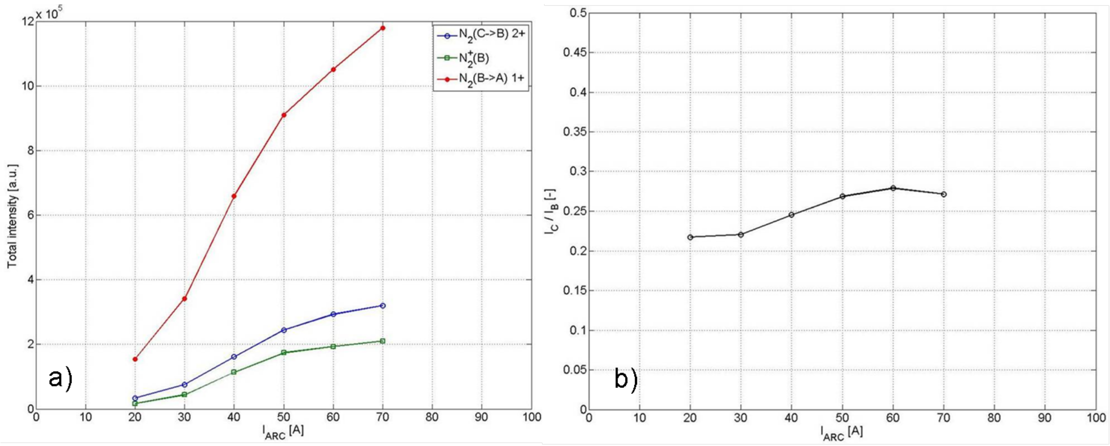

Figure 5.8: Behaviour with I_{ARC} of *(a)* total light intensities of the main electronic nitrogen states and *(b)* the ratio I_C/I_B, LEP module, grounded circular anode, N_2 pressure $1.4 \cdot 10^{-3}$ mbar, B $= 0$ G.

5.1.3 Evolution with magnetic field strength

Using the DC plasma source adds another external parameter which can influence the plasma composition, the magnetic field. The use of the magnetic field is to increase the length of the plasma plume into the chamber, which may have an effect on the EEDF in the measurement zone. The behaviour of the total light intensities with the magnetic field strength of the main radiative electronic states of nitrogen and the ratio I_C/I_B are shown in figure (5.9).

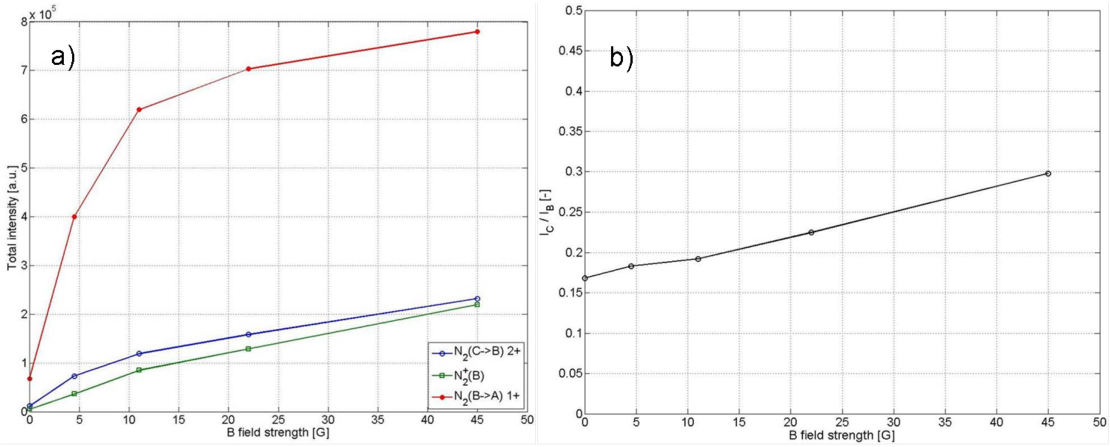

Figure 5.9: Behaviour with the magnetic field strength of *(a)* total light intensities of the main electronic nitrogen states and *(b)* the ratio I_C/I_B, $I_{ARC} = 10$ A, N_2 pressure $1.4 \cdot 10^{-3}$ mbar.

The light intensities exhibit a fast increase in the range B$= 0 - 10$ G, then they saturate. T_e increases also with the magnetic field strength, seen by the increasing ratio I_C/I_B. The magnetic field increases the path of the electrons into the chamber from the ionisation source. This can explain also the faster increase of the N_2(B) state with respect to the other states, because the main part of the electrons are low energetic. The magnetisation of the electrons, which are magnetised above a magnetic field strength of 10 G, leads to the global increase of the light intensities. Above this magnetic field strength, T_e starts to rise (figure 5.9b), indicating that energetic electrons are brought to the measurement zone. As with the power increase, Langmuir probe measurements confirm the increase of the plasma density in the centre of the reactor.

5.1.4 Conclusion

The change of the plasma source has an effect on the EEDF, as shown by the Langmuir probe measurements. The presence of the electron beam lowers the electron temperature of the bulk Maxwellian distribution, because the ionisation is made by the energetic electrons of the electron beam. The plasma composition is very similar to the one found with the RF plasma source, and cannot be changed with the variation of the gas pressure, discharge current or the magnetic field strength. The plasma density is sensitive to these external parameters, and is found to be in the same order as the RF plasma source without the extraction grid. The magnetic field has an effect on the plasma plume, which is extended into the chamber.

5.2 Uniformity of the plasma

The plasma composition is relatively constant in the pressure range, and is similar in both plasma sources. The plasma density can be tuned, depending on the external parameters. But these parameters have an impact on the plasma uniformity along the wafer, important parameter for the deposition, which becomes the determinant condition for the choice of the plasma source. The uniformity of the plasma parameters is evaluated with movable Langmuir probe and by moving the OES fibre along the horizontal window, in the configuration with the grounded circular anode close to the plasma source.

The plasma uniformity measured by the total light intensities of the main electronic nitrogen states is presented in the figure (5.10). The behaviour is a bell shape with a maximum at the electron beam location. All the radiative states follow the same profile, indicating that the plasma is more intense within the electron beam than outside, without changing the plasma composition. The uniformity is about 15%, which is about three times worse than with the RF plasma source. The ratio I_C/I_B indicates that T_e is slightly higher in the electron beam, where more energetic electrons are remaining from the initial plasma plume. As the radial behaviour of all radiative states is the same, from now only the uniformity of the total light intensity of the N_2(B) state will be presented. To probe T_e changes, the ratio I_C/I_B will also be shown as a function of the external parameters.

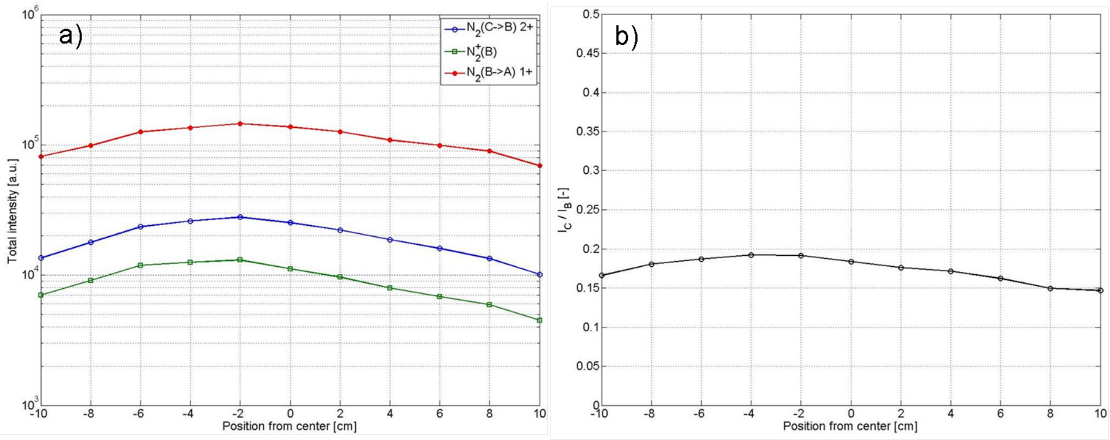

Figure 5.10: Plasma uniformity seen in terms of *(a)* total light intensities of the main electronic nitrogen states and *(b)* the ratio I_C/I_B, $I_{ARC} = 10$ A, N_2 pressure $8.2 \cdot 10^{-4}$ mbar, $B_{\text{field}} = 0$ G.

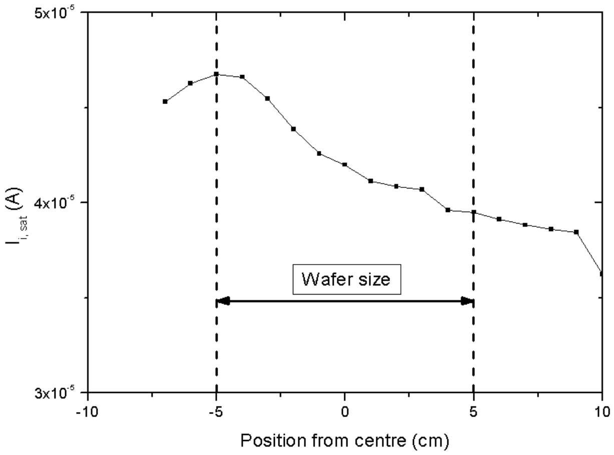

Figure 5.11: Plasma uniformity shown in terms of variation of ion saturation current, $I_{ARC} = 10$ A, N_2 pressure $8.2 \cdot 10^{-4}$ mbar, $B_{\text{field}} = 0$ G.

Figure (5.11) shows the ion saturation current profile obtained in the same experimental conditions with the Langmuir probe. The uniformity obtained with the ion saturation current is about 8% along the wafer size, better than with OES. The reason is that the excitations are more sensitive to energetic eletrons than to the bulk Maxwellian, which participates to the plasma density measured by the Langmuir probe. This configuration however (anode close to source) leads to the best uniformity profile.

The Langmuir probe has also been installed closer to the plasma source, between the source and the anode (see figure (1.6)). Figure (5.12) compares the ion saturation current profiles close and far from the plasma source. The electron beam coming out of the plasma source is clearly visible close to it (figure (1.4)), with an about three times higher plasma density in the electron beam than outside of it. As the distance between the plasma source and the measurement point increases the profile flattens and the density decreases. To avoid a high non uniformity on the wafer, a certain distance to the plasma source must be taken, as shown by this measurement.

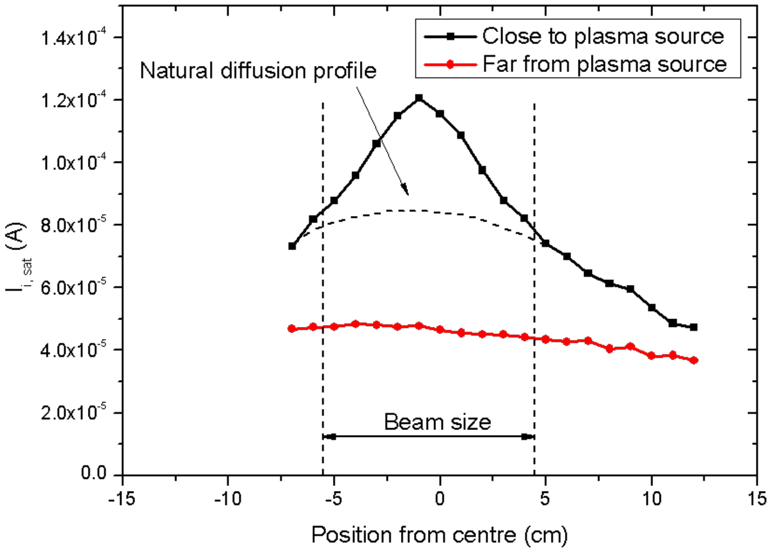

Figure 5.12: Uniformity along the reactor chamber by comparing the ion saturation current close and far from the plasma source, $I_{ARC} = 10$ A, N_2 pressure $8.2 \cdot 10^{-4}$ mbar, $B_{\text{field}} = 0$ G.

The profile close to the plasma source seems to be a combination of two shaped profiles: the first one, with the largest radius, is the natural diffusion density profile coming out a single hole and the second shape is the electron beam, with a sharper profile. These latter electrons are stopped by collisions in the space between the plasma source and the substrate and are almost no more present far from the plasma source.

5.2.1 Evolution with pressure

The total light intensity of the $N_2(B)$ state at different nitrogen pressures and the ratio I_C/I_B are shown in figure (5.13). It is seen that the pressure increase does not affect the bell shaped profile, and that the plasma density is similar. The ratio I_C/I_B decreases with the increasing pressure, indicating a colder plasma at the same point, but keeping the same bell shape. The ion saturation current measurements confirm the trends highlighted by the OES, showing profiles similar to the one seen on figure (5.12) far from the plasma source. The gas pressure has thus no impact on the plasma composition and on the uniformity of the plasma at the substrate, under the given geometrical conditions.

Figure (5.14) presents measurements of the floating potential profiles with the anode grounded and floating. The floating potential is linked to the electron beam energy. With the grounded anode, V_f is always negative, and the evolution with pressure indicates

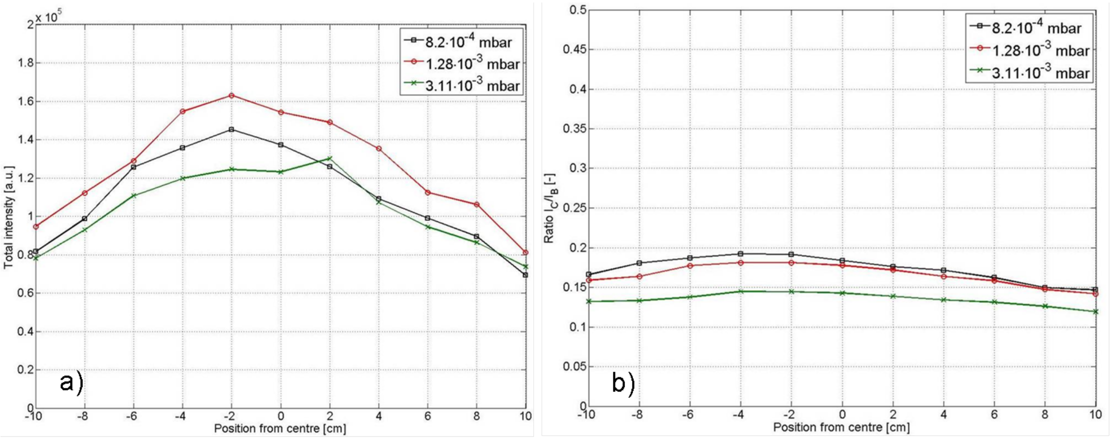

Figure 5.13: Effect of the pressure on the plasma uniformity seen in terms of *(a)* total light intensity of the N_2(B) state and *(b)* ratio I_C/I_B, $I_{ARC} = 10$ A, $B_{\text{field}} = 0$ G.

that the beam energy is higher at low pressures. The increase of pressure makes also the plasma plume being confined closer to the plasma source exit, reducing the electron beam density far from the plasma source. The profiles are relatively flat for every pressure, meaning that the electron beam is flared. With the anode floating with respect the to walls the profiles are more shaped with the electron beam more marked, because the discharge current is forced to pass through the anode, and V_f is always positive. At low pressure the profile of the electron beam is a bell shape, which flattens with the increasing pressure. The maximal energy that ions can have is higher with the anode floating, and the uniformity is worse at low nitrogen pressures than with the anode grounded.

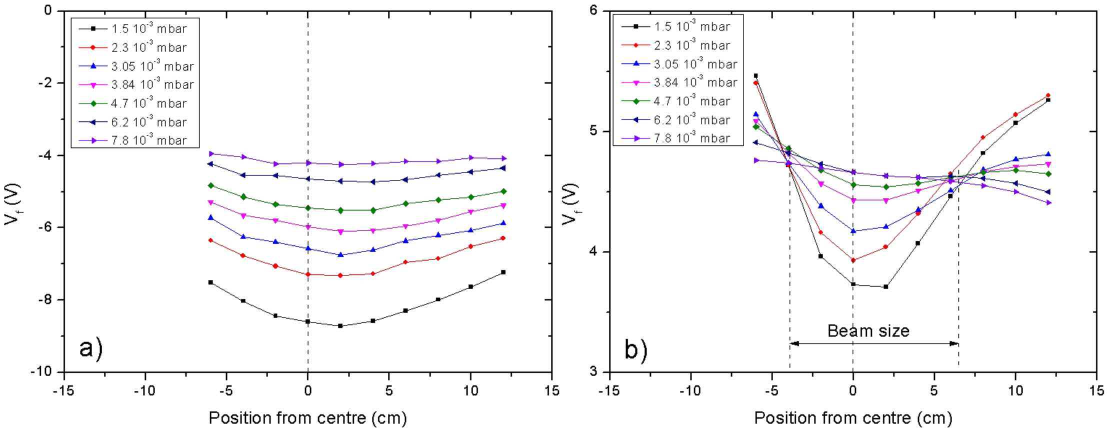

Figure 5.14: Floating potential profiles as a function of the pressure with the circular anode *(a)* grounded and *(b)* floating, $I_{ARC} = 10$ A, $B_{\text{field}} = 0$ G.

5.2.2 Evolution with power and magnetic field strength

The influence on the plasma uniformity of the two external parameters modifying the plasma plume shape is presented in this section, in terms of OES measurements. Increasing the discharge current increases the accelerating voltage needed to sustain the discharge, whereas the magnetic field forces the electrons to follow the magnetic field lines, setting the plasma in a columnar shape.

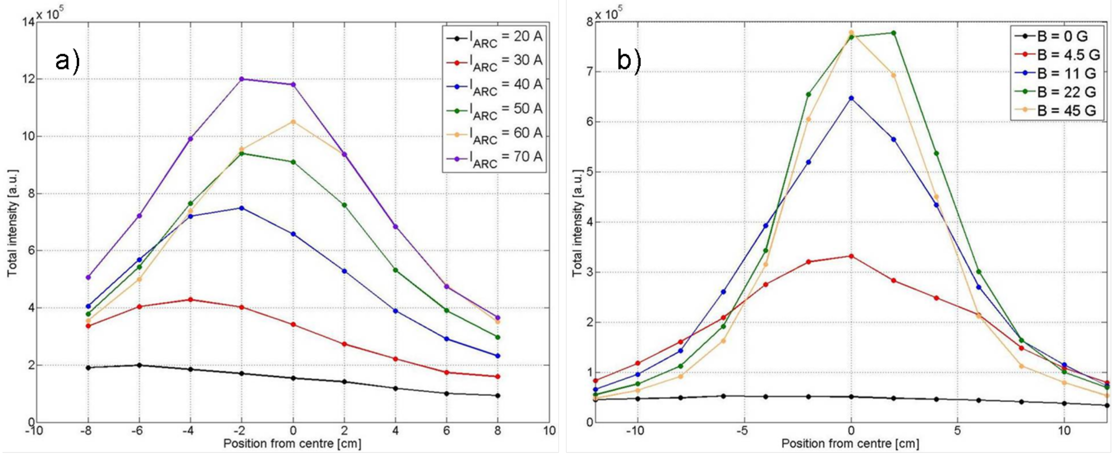

Figure 5.15: Effect on the plasma uniformity shown in terms of *(a)* increasing discharge current with $\mathrm{B_{field}} = 0$ G and *(b)* increasing magnetic field strength with $\mathrm{I}_{ARC} = 10$ A, N_2 pressure $1.4 \cdot 10^{-3}$ mbar.

The effect of the discharge current on the plasma uniformity is shown in figure (5.15a). Increasing the discharge current leads to an increase of the electron beam energy, thus it propagates more into the chamber. The beam energy shows a saturation for $I_{ARC} > 20$ A, determined by floating potential measurements. A pronounced bell shape profile arises, with a peak sharper with higher discharge currents. The single hole separation plate leads to an increased density in the centre with a radial diffusion. The total intensity ratio $\mathrm{I}_C/\mathrm{I}_B$, not shown, indicates that T_e is not varying with I_{ARC}. T_e is determined by the pressure, constant in this particular study, thus the plasma composition remains the same, only the plasma density is increased with increasing discharge current. Ion saturation current measurements confirm the OES conclusions, with a plasma density more peaked in the centre of the reactor.

The magnetic field showed to have the highest effect on the plasma density, in the centre of the reactor. The magnetisation of the electrons is very effective, until reaching a saturation above 10 G (see figure (5.9)). Figure (5.15b) presents the effect of the magnetic field strength on the profile of the total light intensity of N_2(B). The plasma is confined into a column and the light intensity at the centre increases rapidly then saturates, above a magnetic field strength of about $B = 10$ G. The width of the column remains more of less constant. T_e increases with the magnetic field in the centre of the column (as in figure (5.9b)), but it decreases outside the column, because the radial diffusion is largely reduced. The beam energy increases with the magnetic field strength, as the plume propagates into the process chamber.

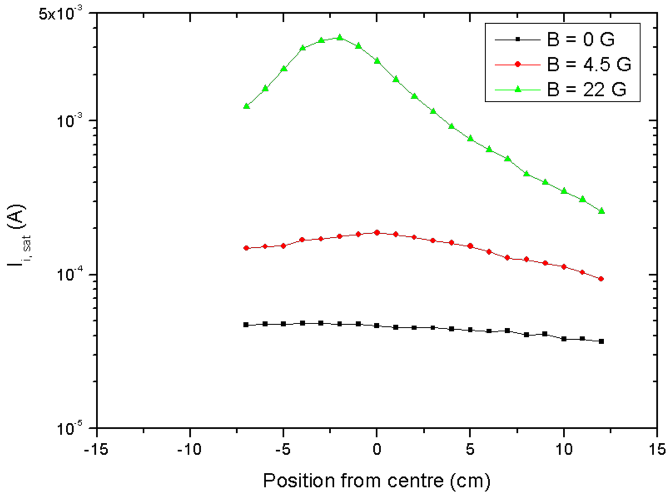

Figure 5.16: Effect of the magnetic field strength on the plasma uniformity seen through ion saturation current profiles, N_2 pressure $1.4 \cdot 10^{-3}$ mbar, $I_{ARC} = 10$ A.

The effect of the magnetic field on the ion saturation current profiles is shown in figure (5.16). Ion saturation current measurements not only show that the plasma density increases rapidly in the centre of the reactor but that it increases in the whole reactor. This was not seen with the OES measurements. This difference can be explained by the fact that the radiative states are excited by high energetic electrons, and are less sensitive to the bulk Maxwellian electrons, which participates to the density measured by the Langmuir probe.

5.2.3 Comparison with other electrical configurations

The effect of the external parameters on the uniformity of the plasma in terms of light intensity, plasma density and floating potential has been shown, in the particular electrical configuration of the grounded circular anode close to the plasma source. Changing the electrical connections can lead to a change of the attachment point of the plasma in the chamber, which will affect the plasma uniformity, as briefly seen when the anode was set floating. In this section the comparison between all the electrical configurations tested will be shown in terms of total light intensity of the N_2(B) state and ion saturation current. The multi-hole separation plate (figure (1.3)) will be compared with the single hole separation plate in terms of ion saturation current profiles.

The uniformity pattern with OES was probed with all electrical configurations presented in figure (1.8) with the single hole separation plate, and the figure (5.17) shows the results. The profiles are very similar, with a slightly higher light intensity in the centre.

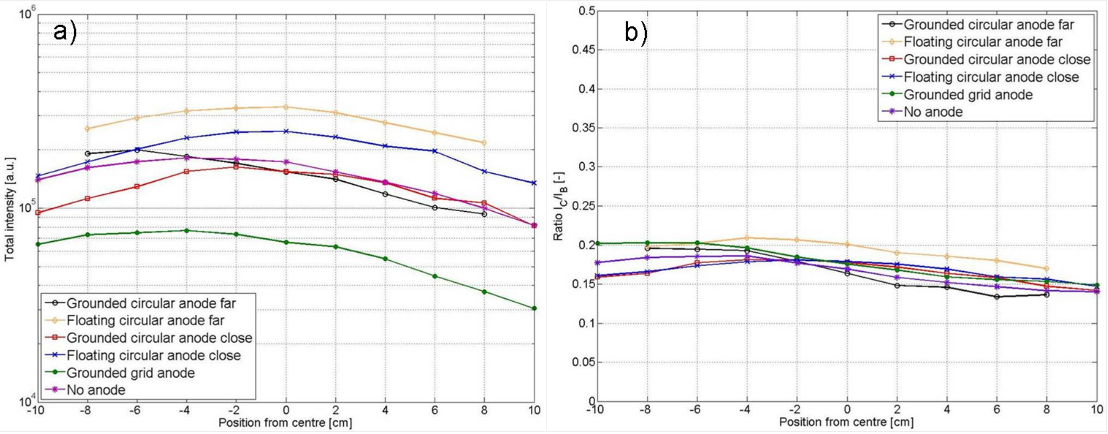

Figure 5.17: OES uniformity comparison of the different electrical configurations through *(a)* total light intensity of the N_2(B) state and *(b)* the ratio I_C/I_B, N_2 pressure $1.4 \cdot 10^{-3}$ mbar, $I_{ARC} = 10$ A, $B_{\text{field}} = 0$ G.

The total light intensity with grid configurations is lower than the others because the plasma density is reduced. T_e profiles are very similar for all the electrical configurations tested, confirming that T_e only depends on the gas pressure and not on the electrical configuration. The profiles are relatively flat, with a small higher temperature in the electron beam still present in the measurement zone.

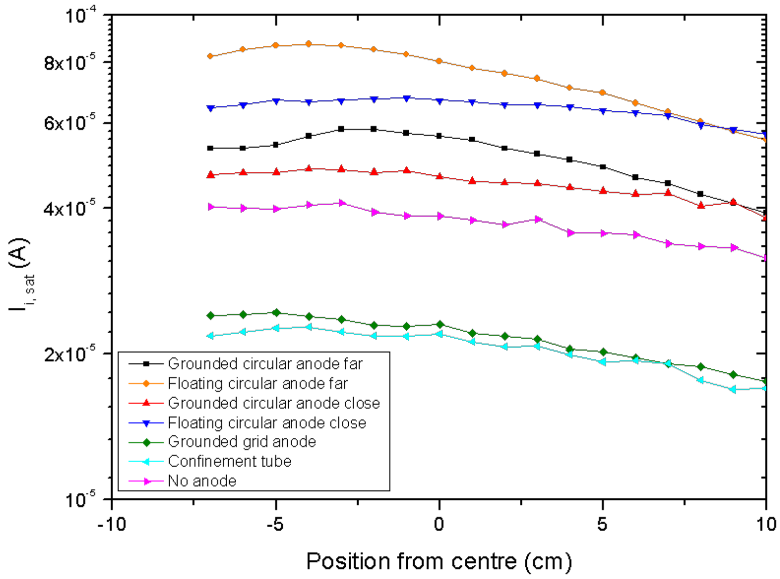

Figure 5.18: $I_{\text{i, sat}}$ profiles comparison of the different electrical configurations tested in the LEP device with the single hole separation plate, N_2 pressure $1.4 \cdot 10^{-3}$ mbar, $I_{ARC} = 10$ A, $B_{\text{field}} = 0$ G.

Ion saturation current profiles shown in figure (5.18) confirms the trends drawn with OES. The plasma uniformity is not affected by the electrical configurations, the profiles are relatively flat with a slight peak at the electron beam location.

To increase the growth rate of the deposition, the plasma density should be as high as possible (see chapter 7). Thus, to increase it efficiently, a magnetic field is used, and as seen above in a particular configuration, this creates a highly non uniform density profile. In order to increase the plasma uniformity when using the magnetic field, other anodes and a different separation plate were tested. The uniformity of the plasma is independent of the gas used and in this study argon was used. The figure (1.4) shows pictures of both separation plates with both gases. The multi-holes separation plate exhibits a multiplicity of small electron beam showers, uniformly distributed on the source exit, which may influence the uniformity beyond the anode. The different configurations with the multi-holes separation plate are shown in figure (1.8).

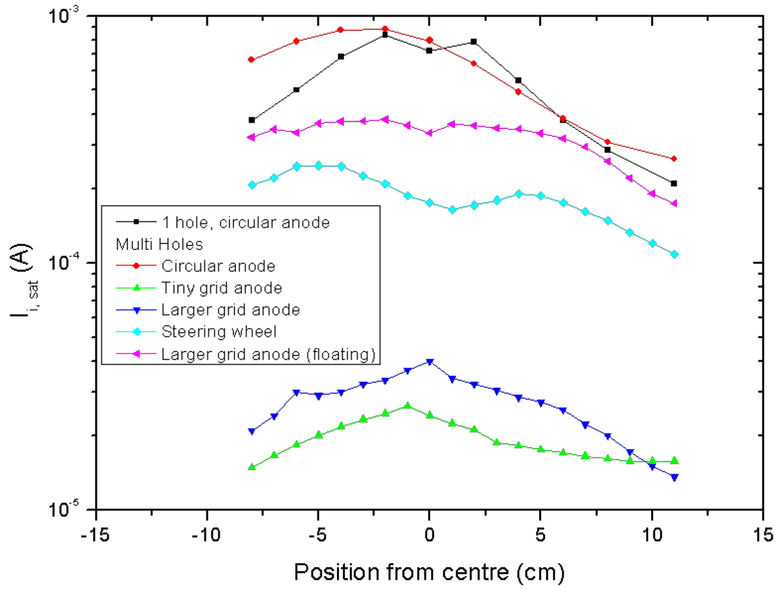

Figure 5.19: $I_{i,\ sat}$ profiles comparison between the single and multi-holes separation plates with the different anodes tested, Ar pressure $1.4 \cdot 10^{-3}$ mbar, $I_{ARC} = 10$ A, $B_{\text{field}} = 22$ G.

Figure (5.19) presents the ion saturation current profiles measured in the different electrical configurations with the multi-holes separation plate. These are compared with the single hole separation plate with the grounded circular anode close, with a magnetic field strength of 22 G. The effect of the magnetic field on the plasma density with the single hole separation plate is seen on figure (5.16) in nitrogen. The single hole and the multi-holes separation plates used with the circular anode give very similar density profiles, better seen in figure (5.20). The plasma uniformity when using a magnetic field cannot be improved by simply changing the separation plate.

Two electrical configurations show a density one order of magnitude lower than the others: both grid anodes set grounded, but the plasma uniformity is improved. The multi-hole separation plate gives a slightly better plasma uniformity with respect to the single hole one, with the same anode. This is due to the multiplicity of small electron showers instead of only one large. The two best electrical configuration in terms of plasma uniformity are the grid anode with the big holes, set floating and the steering wheel anode, which cuts the electron beam with the central discus, thus leading to a "M" pattern. The plasma uniformity with these two configurations is about 10% and 20% respectively, on the wafer size. This is in the order of uniformity obtained with the single hole separation plate without magnetic field. Therefore, relatively uniform profiles can be obtained with the use of magnetic field with a higher plasma density (factor 10). The circular anode shows the worse uniformity pattern using magnetic field.

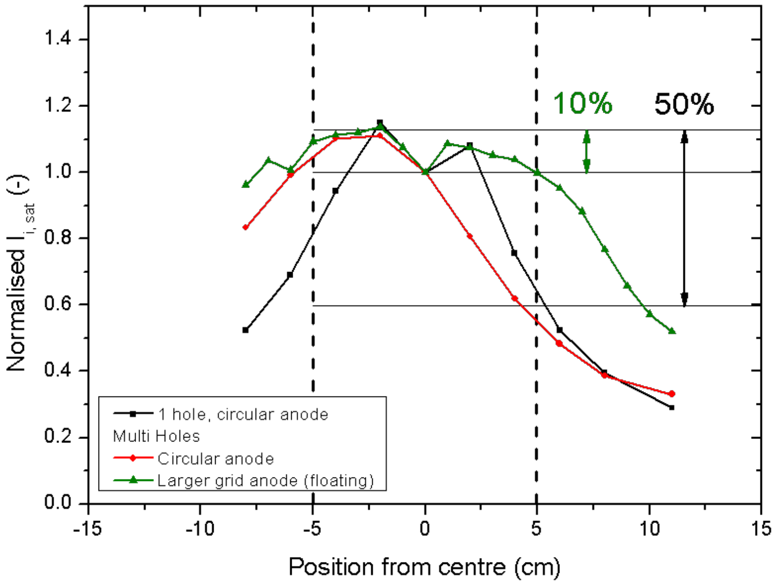

Figure 5.20: Normalised ion saturation current profiles comparison between the grounded circular anode and the large holes grid anode floating, Ar pressure $1.4 \cdot 10^{-3}$ mbar, $I_{ARC} = 10$ A, $B_{\text{field}} = 22$ G.

5.2.4 Conclusion

The plasma uniformity was discussed in terms of plasma density, light intensity and floating potential profiles, in a particular configuration as a function of the external parameters, and compared to different electrical configurations. The pattern of uniformity is not affected by the gas pressure, but with the discharge current and the magnetic field. These latter parameters influence the energetic electrons path in the reactor, leading to an increase of density in the center, creating a bell-shaped profile. Using a magnetic field, different anode concepts were tested in order to increase the plasma density. The steering wheel anode and the grid anode with large holes set floating with respect to the walls showed a similar uniformity than the circular anode without magnetic field, with an increased plasma density. The atomic nitrogen density can thus be increased with the use of the magnetic field, without changing the distribution on the wafer.

5.3 Comparison with the models

As it has been shown in chapter 2 and in this chapter, the EEDF is a Maxwell distribution with an electron beam superimposed. The models presented in chapter 3 were run with this type of EEDF, and the results of the calculations will be compared with the experiment. Again the electron density and temperature (n_e, T_e) will be taken from the experiment as inputs for the corona and CR models.

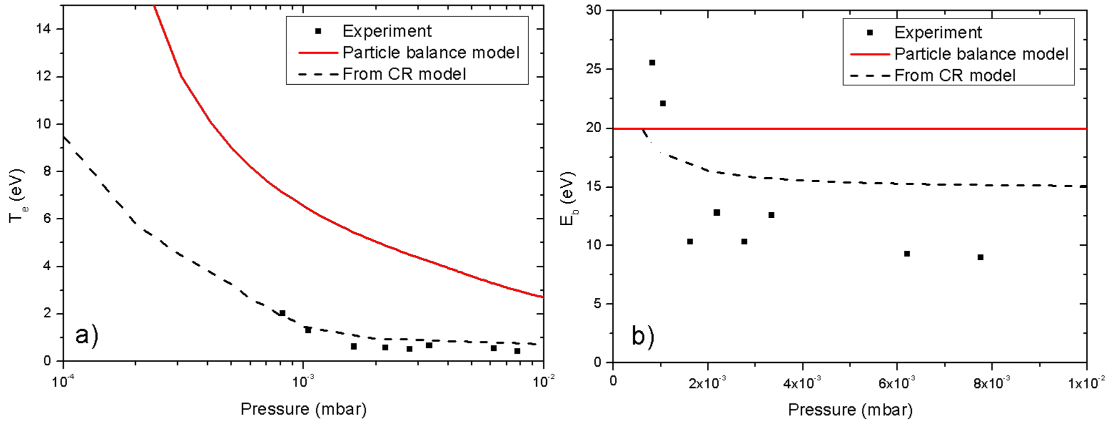

Figure 5.21: Comparison between the experiment and the models of *(a)* the electron temperature and *(b)* the electron beam energy, measured and used in the models.

The first plasma parameter modelled is T_e. The particle balance and the CR models, with the quasi-neutrality problem solved, are compared to the experimental ones in figure (5.21). The particle balance model uses a constant electron beam energy, whereas the CR model needed an adaptation of the electron beam energy to guarantee the quasi-neutrality (figure (5.21b)). T_e comparison between the particle balance model prediction with the electron beam energy constant overestimates T_e with respect to experiment. As with the RF plasma source modelling, the hypothesis of uniform density might be the reason for that. In fact the losses at surfaces forces the temperature to be high to counterbalance the ionisation due to the electron beam. The CR model T_e, with a progressive reduction of the electron beam energy, are in very good agreement with the measured ones (figure (5.21a)), which confirms that the selected processes incorporated in the CR model are the dominating ones, and describe well the experiment.

Figure (5.22) shows the comparison of the ratio between the radiative states from the experiment and calculated with both models using T_e, n_e and E_b from the Langmuir probe measurements and determined analytically by the CR model. Using the experimental data, the calculated ratios are very similar to each other, and the trend is well reproduced compared with the experimental one. The order of magnitude is good, and the match

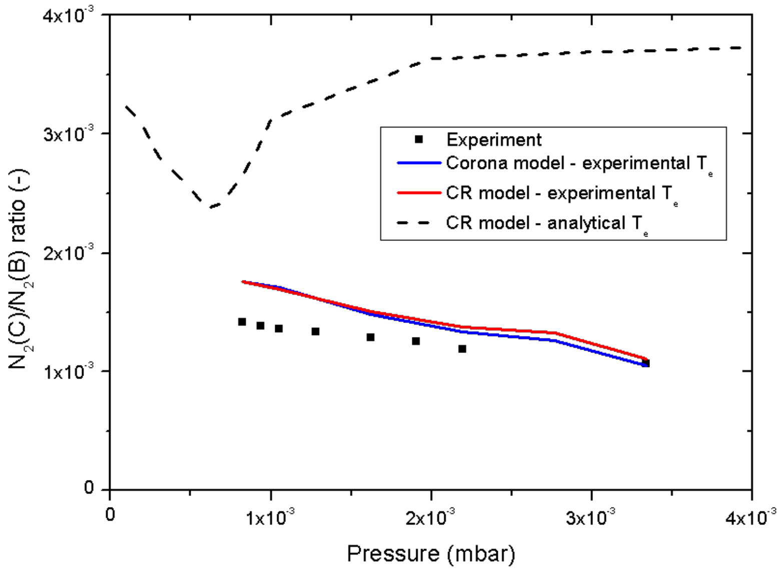

Figure 5.22: Comparison of the $N_2(C)/N_2(B)$ ratio calculated with the corona and CR models and the experimental one.

between models and experiment is better than with the RF plasma source EEDF. The corona and the CR models give almost identical results, meaning that the main populating and de-populating processes are the electron impact and radiative decay, respectively. Using the CR model T_e and E_b, the ratio is greater than with the experimental data. This is due to the higher electron beam energy obtained with the model than measured in the experiment (figure (5.21)b). Moreover the ratio increases above $6 \cdot 10^{-4}$ mbar because the electron beam energy approaches more and more 15 eV, corresponding to the maximum of the cross section for the excitation of the $N_2(C)$ state (figure (3.2)).

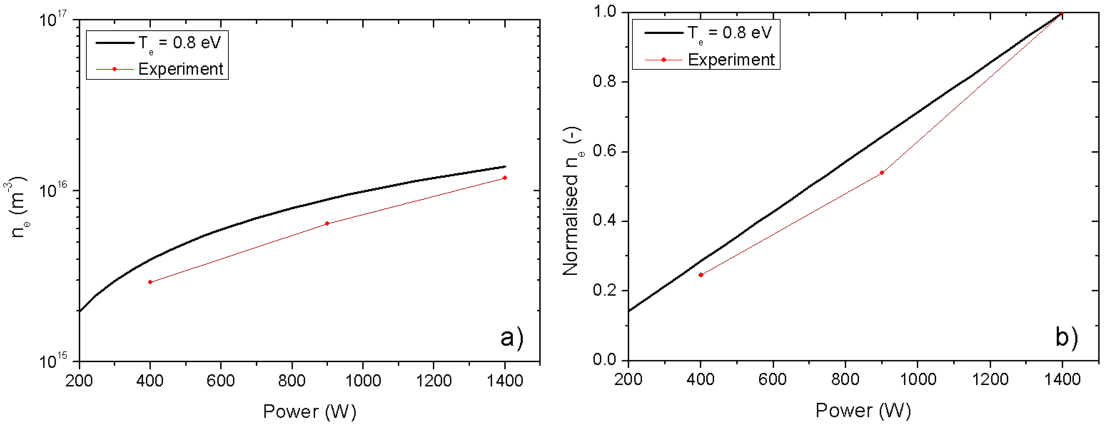

Figure 5.23: *(a)* Plasma density with increasing power comparison between experiment and particle balance model and *(b)* normalised evolution with power.

The last comparison with the models is shown in figure (5.23). The graph presents the comparison of the plasma density between the experiment and the model in two ways: *(a)* absolute values and *(b)* normalised evolution. T_e has been fixed to the one found with the Langmuir probe at this pressure, 0.8 eV, and the electron beam energy at 16 eV. The absolute value of the density found with the model is close to the experimental one, as with the RF plasma source without the grid. This indicates that the uniform density model is more accurate when there are energetic electrons at the measurement zone, which is not the case with the RF plasma source with the grid. The normalised values highlight the linear increase in the model, and show that the experimental densities increase also linearly. The slopes of the evolution are close, justifying *a posteriori* the constant T_e used in the model.

5.4 Conclusion

This chapter has shown the evolution of the plasma parameters using a DC plasma source of pure nitrogen with the change of gas pressure, discharge current and magnetic field in the centre of the reactor, with different anode configurations and different anodes. A large part was dedicated to the uniformity pattern due to the same external parameters variation. As the pressure regime is limited, the EEDF type (Maxwell distribution with an electron beam superimposed) remains the same, but the electron temperature and the electron beam energy are dependent on the gas pressure. The plasma is confined closer to the source if the pressure is increased. The plasma composition could not be changed by the variation of the parameters and the electrical configurations. Higher power increases the plasma density without changing the plasma composition, but influences the uniformity of the plasma. The magnetic field carries energetic electrons at the substrate height, which greatly influences the plasma density. The disadvantage is that the uniformity is drastically reduced, which would lead to a non uniform deposition. The other parameters have only a small impact on the plasma uniformity. To obtain the most uniform plasma density, the discharge current and the magnetic field should be as low as possible.

The plasma composition is unchanged with the change of the plasma source, even with the presence of an electron beam. The gas pressure used in the work determines the plasma composition, independently on the plasma source. Differences in composition could be found if the pressure is increased to the millibar range, due to the different EEDFs.

6 Plasma sources comparison and plasmas with gallium

In the two previous chapters efforts have been made in order to change the plasma composition, with a change of the plasma source. Each source was investigated separately, and the behaviour of the plasma parameters was probed in terms of the external parameters, such as the gas pressure, electric power or magnetic field. In this chapter both plasma sources in nitrogen will be compared. Until now, only pure nitrogen were investigated, to probe the density of nitrogen species. The injection of gallium will be discussed using the RF plasma source. The possible interactions between the Ga and the nitrogen in the plasma will be discussed, as a function of the different external parameters, with some limiting parameters imposed by the Ga effusion cell.

6.1 Comparison between RF and DC plasma sources

In this section the two plasma sources will be compared in terms of the main plasma parameters. Both plasma sources were studied individually in detail as a function of the external parameters in the previous chapters. The main plasma parameters as a function of the pressure and the power are shown on the same graphs in figures (6.1) and (6.2). They show respectively an OES spectrum of nitrogen plasma at the same pressure, $1.3 \cdot 10^{-3}$ mbar, the density ratio $N_2(C)/N_2(B)$ as a function of the pressure, obtained from the OES measurements, the T_e as a function of the pressure, and the plasma density as a function of the increasing power.

The spectra comparison shows that there are only small differences in the spectra. In fact the first positive systems are identical in the three configurations using both plasma sources, except for the atomic nitrogen lines at 821 nm seen in the DC plasma source. The direct dissociation of the nitrogen molecule requires an electron energy of at least 10 eV, which is more probable with the DC plasma source. The second positive systems exhibit also some differences, in particular the band distribution, and the DC plasma source shows higher bands for the excited molecular ion, due to the higher plasma density.

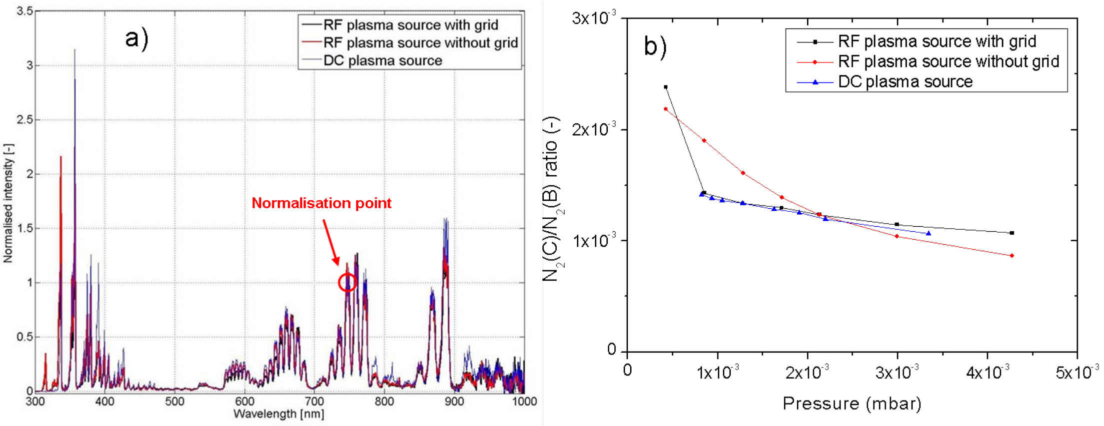

Figure 6.1: Plasma parameters comparison between the RF and DC plasma sources through OES measurements: *(a)* emission spectrum at $1.3 \cdot 10^{-3}$ mbar normalised to the 747.5 nm wavelength, and *(b)* $N_2(C)/N_2(B)$ ratio.

Similar spectra lead to very similar ratios between the radiative states. In fact the density ratios $N_2(C)/N_2(B)$ have the same order of magnitude, and are even superimposed for the RF plasma source with grid and DC plasma source. This confirms the statement that the pressure determines the plasma composition, and not the way the plasma is made, in this pressure regime. Only the RF plasma source without the grid shows a different pattern for this ratio. This is due to higher light intensities of the second positive system, as seen in figure (6.1a). The identical ratios lead to the conclusion that both EEDFs lead to the same excitations of the nitrogen molecule, which are mid-energetic processes ($6-12$ eV threshold energies). The Maxwell EEDF of the RF plasma source leads to the same excitation pattern as the beam-Maxwell with a lower T_e but with an energetic electron beam. The differences arises from the high energetic processes, as the ionisation.

The CR model used with both plasma sources showed a good agreement in terms of radiative states densities and T_e predictions with both EEDFs. As the model describes well the experiment in terms of excitations and plasma density, the atomic nitrogen density predictions can be taken into account. The model predicts a higher N density with the Maxwell EEDF, even if the electron beam in the DC source is at an energy higher than the dissociation threshold energy. This comes from the higher $N_2(A)$ density, from which the dissociation requires less energy. However, if the DC plasma source is used with magnetic field, the plasma density is increased, favouring every reactions, even the dissociation.

The extracted parameters from the Langmuir probe signals (figure (6.2)) show also similar trend with the increasing pressure. T_e as a function of the pressure is shown in *(a)*. The trend is very similar with both RF plasma source without the grid and the DC plasma source, as both sources lead to energetic electrons in the measurement zone. T_e as a function of the RF gridded plasma source is different because the generation of the

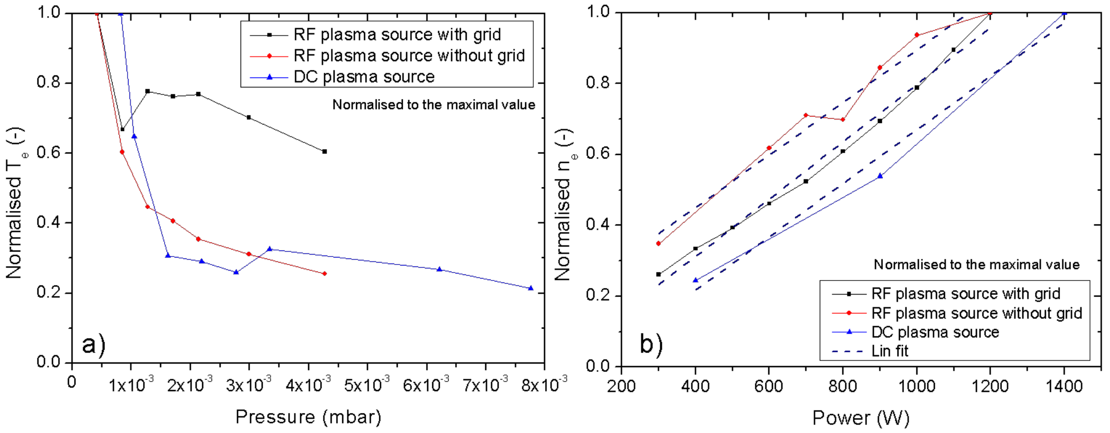

Figure 6.2: Plasma parameters comparison between the RF and DC plasma sources through Langmuir probe measurements: *(a)* normalised T_e evolution with pressure (normalisation to maximal value), and *(b)* normalised n_e evolution with power (normalisation to maximal value).

plasma is separated from the measurement zone. Finally the density increase with the power in the three cases is shown in *(b)* shows a quite linear behaviour. The absolute values of the density differ from each other, as already mentioned, but the evolution is similar.

6.2 Nitrogen plasmas with gallium

The nitrogen plasmas created using both plasma sources exhibit the same composition, only the plasma density is different. Therefore, experiments with gallium were performed with the RF plasma source in both configurations: with and without the extraction grid, because the plasma density in the configuration with the grid is similar to the one using the DC plasma source without magnetic field, and without the grid, the plasma density is similar to the one in the plasma column. The behaviour with the Ga BEP and plasma RF power will be shown with the RF plasma source in both configurations, and compared to the CR model predictions.

The Grotrian diagram of the gallium atom has been presented in chapter 2, figure (2.6). Most of the radiative transitions are below 300 nm, thus absorbed by the windows of the reactor and not detected by the diagnostic setup. The two emission lines captured by the fibre are indicated with a red circle, and are lying near 400 nm. All the excited states of the Ga are lying under 5 eV, with the lowest excited states at 3 eV, the ones visible, and the ionisation of the Ga atom occurs at 6 eV. The cross sections for excitation and ionisation are presented in figure (3.3).

The gallium is evaporated outside the RF plasma source, which influences the interaction with the nitrogen plasma depending on the plasma source configuration. With the extraction grid, the plasma density and T_e are lower than if the plasma source is in the configuration without the grid (figure (4.13)). In this case, energetic electrons are present in the evaporation zone of the gallium (figure (1.10)).

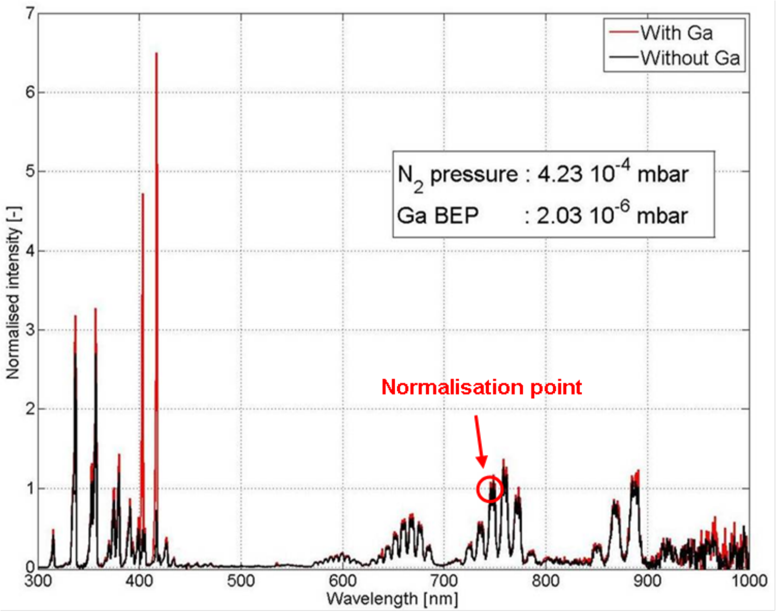

Figure 6.3: OES spectrum comparison of a pure nitrogen plasma and a nitrogen plasma with gallium. RF plasma source with grid, RF power 1200 W, normalised spectra to the 747.5 nm wavelength.

The figure (6.3) presents OES spectra of pure nitrogen plasma and a nitrogen plasma with the evaporation of gallium. Both emission spectra are normalised to the same wavelength, in order to probe changes in the plasma composition. The N_2 excitation pattern is only slightly affected by the evaporation of the gallium, due to the reactions with the Ga, which pumps electrons for the excitation of the first positive system. The very similar N_2 pattern indicates also that no interactions occur between the N_2 and the Ga. Even if the proportion of Ga in the mixture is 0.5%, the Ga light emission dominates the spectrum. This is due to the large Einstein coefficients for spontaneous emission of the Ga excitation, about 3 times higher than the ones from the nitrogen molecule. The RF plasma source with the grid configuration leads to a low T_e Maxwell EEDF and low plasma density. These plasma parameters lead to a high proportion of low energetic electrons, favouring the excitation of the gallium with respect to its ionisation. This is confirmed by the calculated reaction rates given in table (3.5) for low T_e and in table (6.1) below. The low proportion of Ga only changes slightly the N_2 emission pattern, which indicates that the plasma parameters are unchanged, thus the measured plasma parameters in chapter 4 are the same in presence of Ga.

The gallium proportion in the mixture was then varied by changing the effusion cell

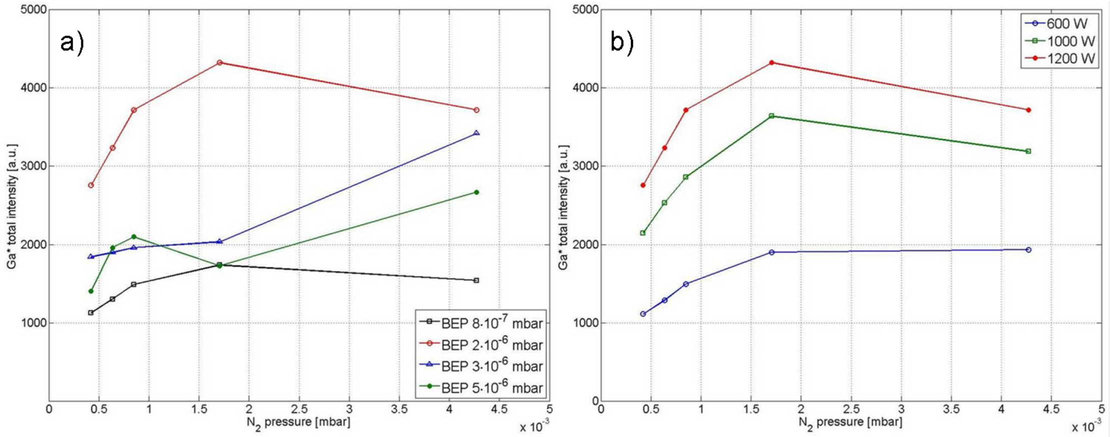

Figure 6.4: Excited gallium light intensity variation with increasing nitrogen pressure with *(a)* variation of Ga BEP with 1200 W of RF power and *(b)* variation of the plasma RF power with a fixed Ga BEP of $2 \cdot 10^{-6}$ mbar; RF plasma source with grid.

temperature. This leads to a change of the BEP of the Ga, and the results on the excited gallium total light intensity are shown in figure (6.4a). The part *(b)* presents the Ga* total light intensity as a function of the RF power of the nitrogen plasma. As the BEP increases, the total light intensity of the excited gallium passes by a maximum (BEP of $2 \cdot 10^{-6}$ mbar), and then decreases again. This is in contradiction with the predictions of the model, shown in figure (3.24), showing a linear increase with increasing BEP. A possible reason is that there are only few energetic electrons outside the plasma source, because of the absorption of the grid and the very low T_e of the EEDF.

The behaviour with the increasing nitrogen pressure below $1.5 \cdot 10^{-3}$ mbar is linked to the plasma density. The further decrease of the Ga* light intensity can be explained by the elastic collisions of the Ga by the increasing density of nitrogen molecules. In fact a higher background pressure the mean free path of the Ga atoms in the mixture is reduced, thus lowering the density of neutral Ga in the measurement zone. Thus an optimal nitrogen pressure for the Ga excitation is existing, and stands around $1.5 \cdot 10^{-3}$ mbar. In the nitrogen pressure range, T_e remains close to 3 eV. At this temperature the reaction rates for the excitation and ionisation are close (table (3.5)). This suggests that the density of ionised gallium is in the same order than the excited one. This suggestion cannot be confirmed by OES measurements, as no excited ion are seen on the spectrum, nor by Langmuir probe measurements, to avoid GaN contaminating coating on the probe tip.

The RF power of the nitrogen plasma has also been varied, to probe the changes on the excited gallium light intensity. The result is that the light intensities increase linearly with the RF power, as the plasma density follows this trend. The shape of the Ga* light emission with increasing nitrogen pressure is the same for all RF power, with the same maximal point at about $p_{N_2} = 1.5 \cdot 10^{-3}$ mbar. This again shows that the plasma composition is not changing with the RF power increase.

Some experiments were also performed without the extraction grid, to probe the effect of higher plasma density and T_e. The comparison of OES spectra from nitrogen plasma and plasma with the evaporation of gallium is shown in figure (6.5). The difference is that T_e is near 8 eV, which changes the reaction rates. The table (6.1) summarizes the changes of the reaction rates for the excitation and ionisation as a function of T_e. As it can be seen, with $T_e = 8$ eV, the ionisation is more efficient than the excitation. This explains the lowering of the Ga* light intensity with respect to the N_2 excitation pattern, in comparison with the configuration with the grid. Again the N_2 excitation pattern is unaffected by the evaporation of the gallium, due to the low proportion of Ga in the mixture.

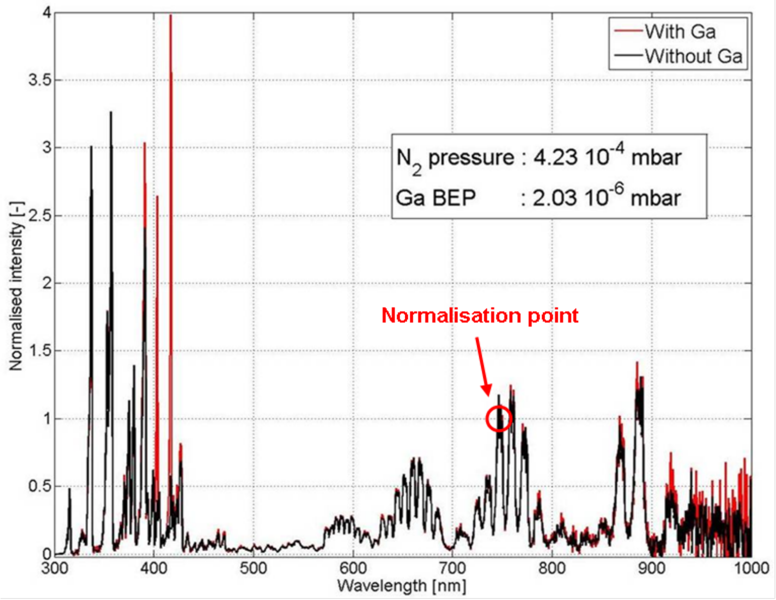

Figure 6.5: OES spectrum comparison of a pure nitrogen plasma and a plasma with gallium. RF plasma source without grid, RF power 1200 W, normalised spectra to the 747.5 nm wavelength.

T_e	k_{Ga*}	k_{Ga^+}
3 eV	$1.5 \cdot 10^{-14}$ m^3s^{-1}	$1.4 \cdot 10^{-14}$ m^3s^{-1}
5 eV	$2.5 \cdot 10^{-14}$ m^3s^{-1}	$4.3 \cdot 10^{-14}$ m^3s^{-1}
8 eV	$3.4 \cdot 10^{-14}$ m^3s^{-1}	$8.5 \cdot 10^{-14}$ m^3s^{-1}

Table 6.1: Reaction rates for the excitation and the ionisation of the Ga for different T_e with a Maxwell EEDF.

The same behaviours as in the configuration with the grid, namely the Ga BEP variation and RF power, are presented in figure (6.6). The Ga* emission light intensity increases when the BEP of the Ga is increased, in this case following the model predictions. Energetic electrons are present in the evaporation zone of the Ga, as T_e is higher in

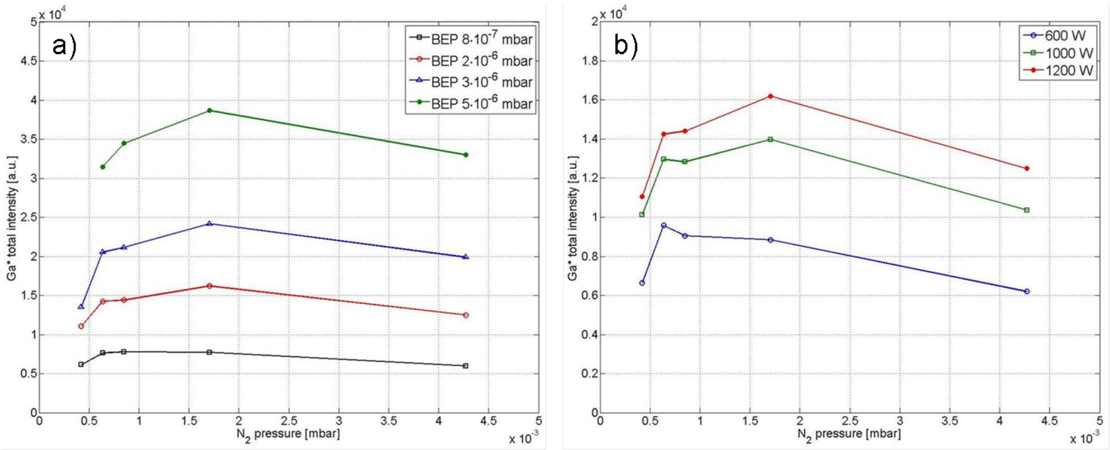

Figure 6.6: Excited gallium intensity variation with increasing nitrogen pressure and *(a)* variation of Ga BEP with 1200 W of RF power and *(b)* variation of the plasma RF power with a fixed Ga BEP of $2 \cdot 10^{-6}$ mbar; RF plasma source without grid.

the nitrogen pressure range probed. This might explain the behaviour of the curves with respect to the increasing BEP. The shape of the curves is the same for all the Ga pressures, which was not the case in the configuration with the grid. There are also some similarities with this configuration, as the existence of an optimal nitrogen pressure for the maximum of the excitation of the Ga and the constant electron density in the N_2 pressure range. The total light intensities are also about 10 times higher in the configuration without the grid than with the grid, because of the higher plasma density in this configuration.

In the part *(b)* of this figure, the behaviour of the Ga* light intensity is shown with different RF power of nitrogen plasma, using the plasma source without the grid. The measurements done in nitrogen plasmas showed that the plasma composition is unchanged with the power increase, only the plasma density changes. This has an effect on the values of the Ga* light intensities, not on the shape of the curves. The increase of the Ga* light intensities follows the one of n_e, the only varying parameter for the determination of the reaction rate.

Both plasma source configurations showed the same behaviour of the Ga light intensity with the nitrogen pressure. The differences in light intensities between both configurations are explained by the differences of the plasma parameters, such as the plasma density and T_e. Both parameters have an effect on the final density of a reaction: T_e on the reaction rate k and n_e is a factor of proportionality. These parameters are independent of the Ga injection, as the proportion is very low in the mixture. The ionisation of the Ga is an unknown of the experiment, because no excited ion is seen with the OES, and no Langmuir measurements were performed, only suggestions from the reaction rates can be made. The impact of the presence of such ions in the deposition procedure is thus also unknown.

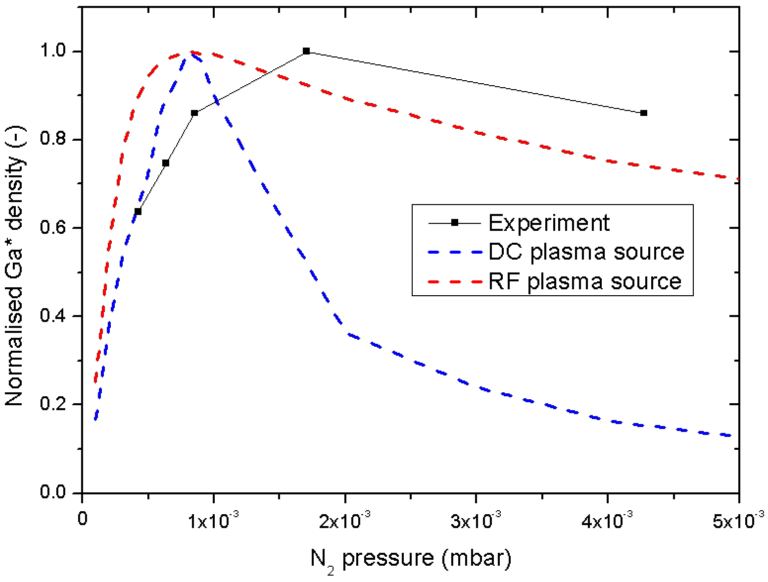

Figure 6.7: Comparison between the experimental measurement and the CR model with both plasma sources EEDFs. The curves are normalised to their maximal values.

The measurements are compared to the CR model in figure (6.7). This figure presents normalised profiles of the excited Ga atoms as a function of the nitrogen pressure obtained experimentally, and using both plasma sources EEDFs: Maxwell EEDF and beam-Maxwell one. The densities from the model are obtained with the CR analytical T_e to get the quasi-neutrality in the plasma, whose T_e are the closest to the experimental ones. The EEDF which fits the best the measurements is the Maxwellian one. In fact the shape of the experimental measurement is well reproduced, but the nitrogen pressure for the maximal Ga* density value obtained with the models is lower than the experimental one. The beam-Maxwell EEDF leads to a fast decrease of the Ga* density after the maximal point. This is due to the presence of the electron beam, which favours more and more the ionisation instead of the excitation of the Ga with the increasing pressure, as the value of the electron beam energy approaches 10 eV, the maximal point of the cross section for the ionisation. This explains the lower Ga* density in all the pressure range, and the faster change in shape. The good agreement between the model predictions and the experimental is another proof that the electron impact excitation and radiative decay are the dominant processes in low pressure plasmas. Other predictions, such as the increase of the Ga* density with BEP and RF power, have been also verified by the experimental results.

6.3 Conclusion

This chapter presented the comparison of the experimental results obtained with both plasma sources: density ratio $N_2(C)/N_2(B)$, electron temperature and plasma density.

The evolution with pressure and power of the extracted plasma parameters are very similar, confirming that the plasma composition is not dependent on the plasma source, but only the plasma density.

The injection of Ga was also presented with the RF plasma source with and without the extraction grid. As the heavy particles collisions are rare at low pressures, the evaporation of Ga in the nitrogen plasma does not influence the nitrogen excitation pattern. The Ga excitation is very effective and the light emission of the excited Ga dominates the spectrum, in both source configurations. The behaviour of the Ga* light intensity follows the predictions of the CR model with increasing Ga BEP and RF power, when energetic electrons are present in the evaporation zone, i.e. in the configuration without the extraction grid.

7 GaN growth

In this chapter the deposition of GaN layers obtained from both plasma sources are correlated with the plasma parameters studied in the previous chapter. The analysis of the layers have been done at LASPE, the Laboratory of Advanced Semiconductors for Photonic and Electronics. As one of the prior objectives of this thesis is to understand the physics of the interaction between the gas and metal vapour, only a portion of the work done to improve the deposition of structured GaN is presented here. The depositions are all made on 4” Si(111) wafers from Siltronix™. The parameter space is large including the wafer temperature, the Ga flux and the argon flow necessary to ignite a plasma using the DC plasma source (chapter 1). The results presented in this chapter will show the changes in the structure (section 7.2) and the growth rates (section 7.3) as a function of the N_2 pressure, with other process parameters constant, to attempt to make a correlation with the important plasma parameters.

7.1 Deposition procedure

The typical deposition procedure is to make first a thermal cleaning of the wafer, then apply a nitridation layer using a nitrogen plasma and finally to grow the GaN layer on it. For this study, no AlN nucleation layer was grown between the Si(111) and the GaN.

A typical procedure consists to first clean the wafer by heating it up to $1000°$C allowing removing the native oxide. The cleanliness is checked during the cooling down, by obtaining the $7x7$ reconstruction of the silicon on the RHEED pattern, as in figure (7.1b).

Once the oxide is removed the temperature is set to the desired growth temperature, typically in the range $600-800°$C. Then the nitrogen plasma is ignited and the wafer is nitrided. This step is used to form Si_xN_y complexes at the surface, to reduce the lattice mismatch between Si and GaN, which can be seen as favourable spots for the growth. Finally the Ga cell is opened with a shutter, allowing to evaporate Ga towards the substrate. The Ga reacts with the nitrogen plasma and from the reactions produces

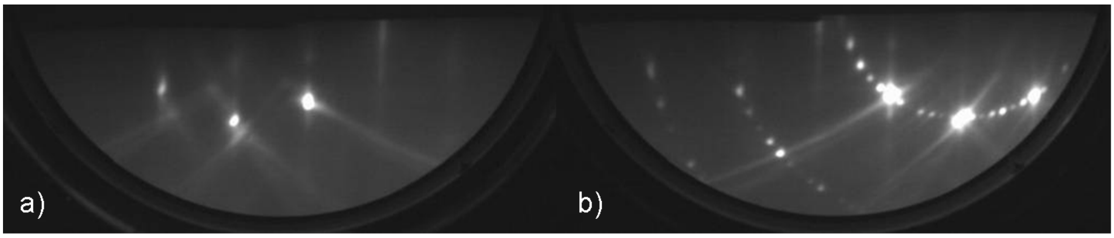

Figure 7.1: Example of RHEED pattern *(a)* during the conditioning at 1000°C and *(b)* at the $7x7$ transition during the cooling down.

a growth of GaN. The type of structure of the grown GaN and the growth rate are determined using SEM and laser reflectometry, respectively. These two aspects of the growth will be correlated to the plasma parameters.

No AlN buffer was grown between the Si and the desired GaN, although it is commonly used [89–91]. The goal of such a buffer is to reduce the lattice mismatch between the Si wafer and the GaN. Another difficulty with direct growth of GaN on Si(111) is encountered during the cooling down after the deposition. This is linked to the large difference of the thermal expansion coefficients of both materials. Such a difference (57% [89]) leads to strong thermal constraints during the cooling down of the substrate, which is the origin of formation of cracks and dislocations in the grown layer. Dislocations and cracks reduce the efficiency of the deposited layer for electronic and optoelectronic applications. The direct growth of GaN on Si(111) also leads to the formation of polycrystalline GaN [92–94], probably due to the formation of an interfacial layer, typically Si_xN_y [95]. AlN buffers were not grown in this work in order to keep the procedure of the growth as simple and fast as possible. Simple in the sense that it was not necessary to install another effusion cell for Al and study the deposited AlN to optimize it for the deposition of the desired GaN structure. The study of such buffer layers can be quite time consuming, as it impacts on the GaN deposition.

The general steps of the deposition described above are identical for both plasma sources. This has some consequences especially for the nitridation. In fact, with the DC plasma source some argon is needed for the ignition of the plasma (chapter 1). The presence of the argon can modify the density and the temperature of the electrons, and the ion composition. This latter can lead to Ar^+ ion implantation in the silicon wafer and change the nitridation procedure. In order to reduce the impact of argon, no magnetic field was used with the DC source during the nitridation, but it was used during the deposition of GaN.

7.2 Structure of the layers

In this section the structure of the layers will be discussed in terms of SEM images, RHEED pattern and XRD full width at half maximum (FWHM). The structure is changing from a 2D layer to 3D nanocolumns just by changing the plasma and the growth parameters. Growths with both plasma sources will be discussed separately, and a general conclusion will be drawn.

7.2.1 Using the gridded RF plasma source

The depositions were firstly made using the RF plasma source with the extraction grid. The structure was probed in terms of RHEED pattern during the growth, and after the deposition procedure to see the morphology of the surface. SEM images from the side of the wafer were also performed to verify the RHEED diffraction pattern.

Figures (7.2) and (7.3) show the layer structure as a function of the N_2 pressure, through SEM images from the side and the RHEED pattern, respectively. As the other plasma and growth parameters are kept constant, the change in structure comes from the increase of the nitrogen pressure. In fact at low N_2 pressures the growth is a 2D layer, compact, as clearly seen on the SEM image, as well as on the RHEED pattern showing vertical lines.

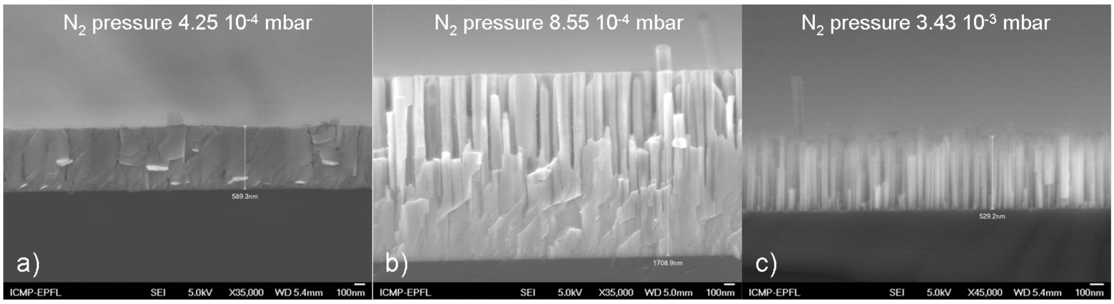

Figure 7.2: SEM images from the side of wafers grown at different N_2 pressures: *(a)* $4.25 \cdot 10^{-4}$ mbar, *(b)* $8.55 \cdot 10^{-4}$ mbar and *(c)* $3.43 \cdot 10^{-3}$ mbar, with a constant Ga BEP of $2 \cdot 10^{-6}$ mbar and RF power of 1000 W, sample temperature during growth 600°C.

The partial pressure ratio between N_2 and Ga is about 200. This gives an indication on the ratio between the density of N and Ga available for the growth. If the same ratio between the N_2 and N densities as in the table (3.2) (CR model) is taken, the density ratio between N and Ga is about 0.5. This means that for each N atom reaching the surface, 2 Ga atoms are present: the growth is in the ”Ga rich” regime. When the N_2 pressure is increased to $8.55 \cdot 10^{-4}$ mbar, the ratio increases to about 1.1, keeping the arbitrary value of the model. This ratio indicates that at this pressure the growth is near the stochiometric point, where the N and Ga densities are equal. At this point it is seen on the SEM image that there is a change in the structure: some nanocolumns are growing on a 2D layer. The quantity of gallium is not sufficient to make a full recovery of the layer and the layer starts to show a 3D structure. This is also seen on the RHEED pattern, with the appearance of dots on the vertical lines.

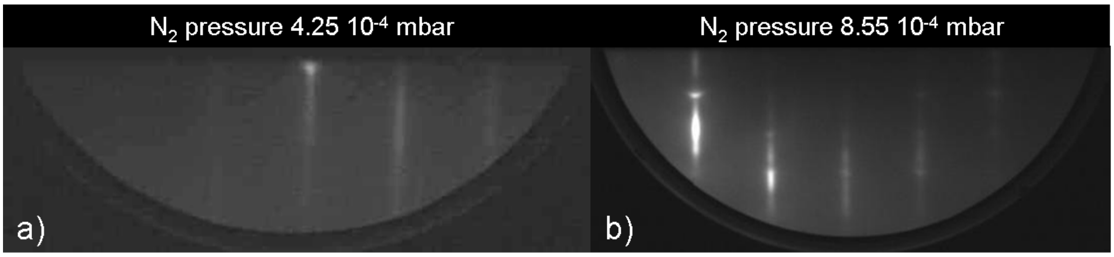

Figure 7.3: RHEED pattern showing the surface structure of wafers grown at N_2 pressure of *(a)* $4.25 \cdot 10^{-4}$ mbar and *(b)* $8.55 \cdot 10^{-4}$ mbar, with a constant Ga BEP of $2 \cdot 10^{-6}$ mbar and RF power of 1000 W, sample temperature during growth 600°C.

There is also a chamfer on the dots, meaning that there are some mechanical constraints during the cooling down of the sample. When the pressure is increased to $3.43 \cdot 10^{-3}$ mbar the nitrogen is in excess with respect to the Ga, the growth is in the ”N rich” regime. In fact the ratio of N and Ga densities increases over 4 in this case, taking the ratio N/N_2 from the model. In this regime the growth shows 3D structure, as nanocolumns. It is clearly seen on the SEM image (figure 7.2c). The fact that nanocolumns can be grown on Si(111) under ”N rich” regime is known [6, 9, 11, 96], but the temperature of the substrate used here is 200°C lower than the ones given in the literature. The growth rate will be compared in the next section.

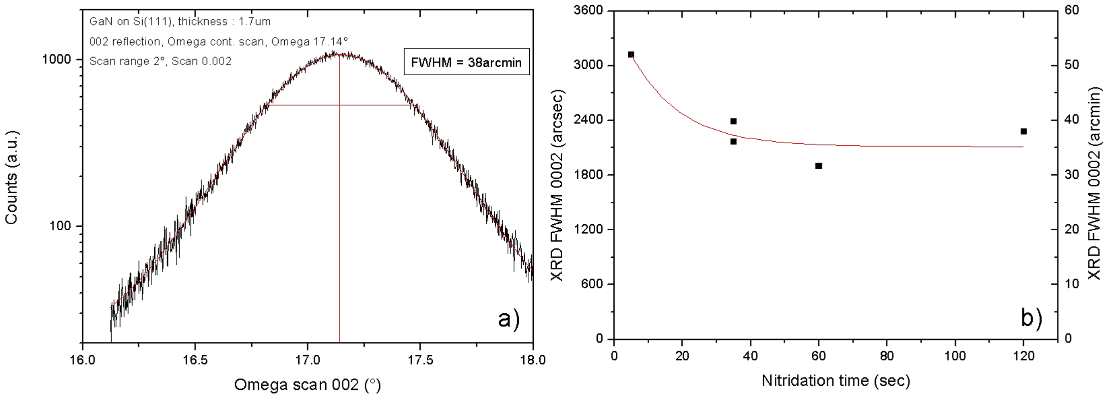

Figure 7.4: *(a)* Diffraction pattern on a Ω scan, showing a Gaussian profile and *(b)* FWHM of the Gaussian as a function of the nitridation time.

The nitridation time has also been varied, to study the effect of a thicker intercalary Si_xN_y layer. It is found in literature that a longer nitridation time can lead to a better material quality [97]. The effect of the nitridation can be seen through XRD, SEM and RHEED measurements. Figure (7.4) shows *(a)* the typical resulting pattern of the XRD Ω scan, and *(b)* the FWHM of the Gaussian profile as a function of the nitridation time.

The diffraction pattern exhibits a large Gaussian profile, with a FWHM of about 40 arcmin. This value is much higher than the ones found with other techniques (MBE or MOCVD [98–101]), indicating that the quality of the layer could be improved. The nitridation time has a low impact on the quality, as seen on figure (7.4b). In fact the trend is that above 30 s of nitridation, the FWHM of the Gaussian remains the same. This indicates that the impact of the nitridation layer on the deposited material quality is limited by the growth conditions of the GaN layer following the nitridation. The shortest nitridation time used in this work shows that the quality is worse and that a consequent $\mathrm{Si}_x\mathrm{N}_y$ layer is necessary to grow better quality GaN with this method.

The same layers were observed with SEM and the resulting images are presented in figure (7.5). The transition from 2D to 3D structure seen in figure (7.2b) is also seen on this figure. In fact the structure of the layers is different between the one with the shortest time (figure (7.5a)) and the others. The nitridation time has no effect on the thickness of the sample, as indicated in the figure. Longer nitridation time, and thus a thicker $\mathrm{Si}_x\mathrm{N}_y$ layer, seems to create some attachment points for the GaN, leading to nanocolumnar growth. The almost full recovery of the GaN layer may also be linked to the nitridation time, in the sense that the Ga is more mobile on the surface with a thinner $\mathrm{Si}_x\mathrm{N}_y$ intercalary layer.

Figure (7.6) shows again the same layers with increasing nitridation times, in terms of RHEED pattern. All of the pattern shows vertical lines, even if on the longest time, they are very faint. Superimposed on the lines dots of varying intensity are seen. The brightest dots are seen on the longest nitridation time, which indicates that the 3D structure is more marked on this layer. As seen on the SEM, the layer presents a 2D pattern with a 3D structure on it. The distinction with the shortest nitridation time is not seen with this diagnostic. In fact the quality or the recovery of the layers cannot be probed with this diagnostic. Nevertheless the hybrid structure can be seen on every pattern of the figure.

The Ga flow has also been varied, in order to obtain a lower growth rate and to grow 2D layers. The BEP has been divided by a factor of 40, from $2 \cdot 10^{-6}$ mbar to $4 \cdot 10^{-7}$ mbar. SEM images and RHEED pattern of the resulting layers are presented in figure (7.7). The thickness of the layer grown with the lower Ga BEP is about 4.8 times less important than with the higher Ga flow. This indicates that the growth regime is ”N rich”, because the limiting factor is the Ga. The SEM images show that the structure of the GaN is only nanocolumns with the smaller flow, which is in the sense of the increasing ratio of N/Ga. Less Ga is evaporated, which increases the ratio and leads to a only nanocolumnar growth. The SEM image of the lower Ga flow shows also that the surface of the GaN layer is less homogeneous and presents a higher roughness. These observations are confirmed with the RHEED pattern, on which only dots appear, which indicates a 3D growth. The size of the spots shows that there is a high surface roughness due to the spread spots. On the higher Ga flow diffraction pattern vertical lines are

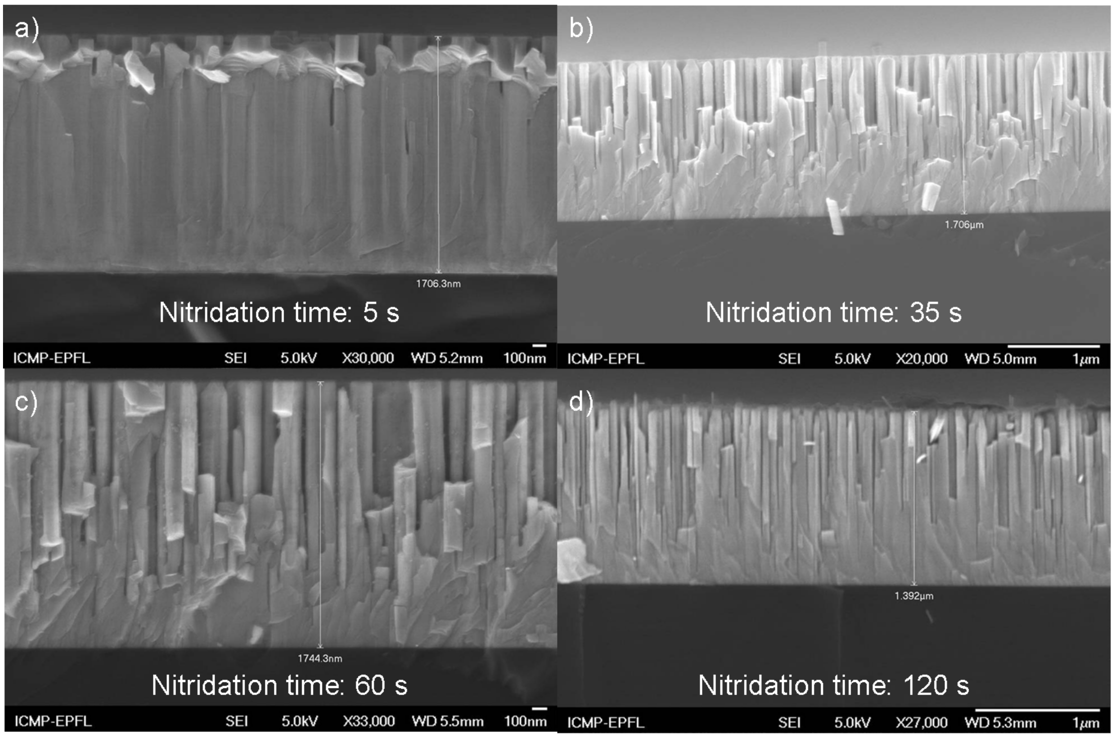

Figure 7.5: SEM images from the side of wafers grown with an increasing nitridation time: *(a)* 5 s, *(b)* 35 s, *(c)* 60 s and *(d)* 120 s.

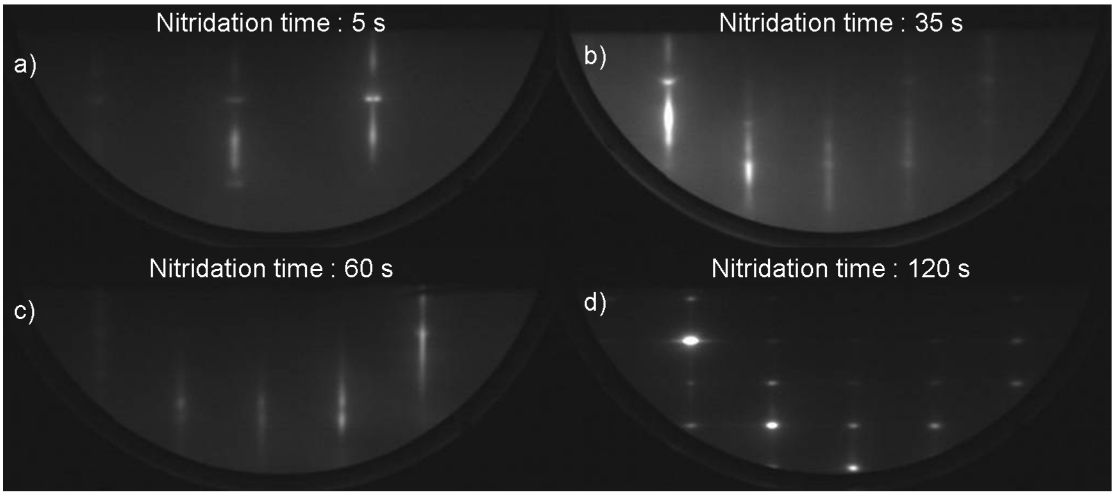

Figure 7.6: RHEED pattern of wafers grown with an increasing nitridation time: *(a)* 5 s, *(b)* 35 s, *(c)* 60 s and *(d)* 120 s.

present, indicating a 2D structure, and the size of the dots is smaller. The chamfer on the spots can be due to the wafer heater temperature ramp for the cooling down.

The external plasma parameters during the growths were set constant, except for the

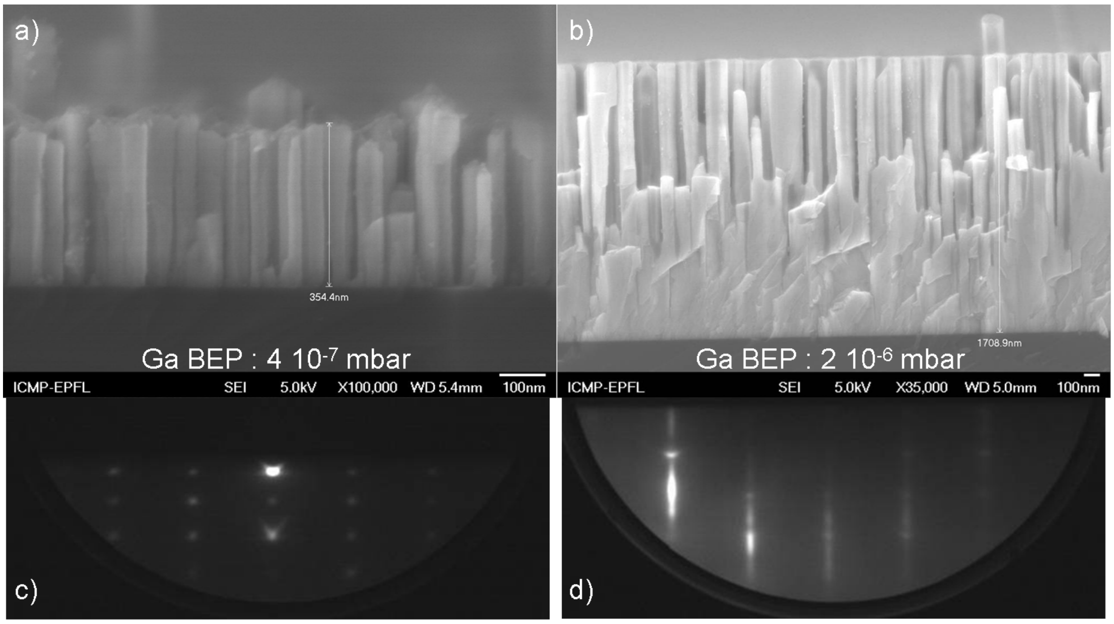

Figure 7.7: SEM images and RHEED pattern of layers grown with different Ga BEP: *(a)+(c)* $4 \cdot 10^{-7}$ mbar and *(b)+(d)* $2 \cdot 10^{-6}$ mbar.

pressure. The measurements done in pure nitrogen plasmas and with the admixture of Ga showed that T_e remains relatively constant with a slight increase of the plasma density. The Ga cell temperature and thus the outcoming flow of Ga are constant, which leads to a varying ratio N/Ga depending on the variation of the atomic nitrogen density and the elastic collisions of the Ga. As the density of the atomic nitrogen seems relatively constant for nitrogen pressure above $5 \cdot 10^{-4}$ mbar (figure (3.25)), the scattering of the Ga is the major reason for the decrease of the density of Ga, thus increasing the ratio N/Ga and changing the morphology of the GaN layer. The estimation with the partial pressures goes into this sense, and is thus a good way to estimate the regime of the growth.

7.2.2 Using the DC plasma source

The first depositions made using the DC plasma source showed nanocolumnar structures. Starting from this point, the nitrogen plasma parameters were set constant and the Ga BEP was modified, in order to control the density and the size of the nanocolumns. The goal was to change the ratio N/Ga to see the transition from nanocolumn to bulk 2D layer. Two plasma parameters were added to the parameter space with this plasma source: Ar flow and magnetic field strength. In fact, as presented in chapter 1, to ignite the DC plasma, some argon is needed. The replacement time of the argon by nitrogen in the reactor takes about 20 seconds, and because of the absence of a shutter in front of the substrate, the nitridation plasma is different with respect to the RF plasma source case. The substrate is nitrided but some argon ion implantation cannot be excluded. As the time to replace Ar by N_2 is long, the argon flow was kept also during the GaN growth step. Based on the results obtained with the RF plasma source, the nitridation time was set to 30 seconds for all growths with the DC plasma source. During the nitridation procedure, no magnetic field was used. The magnetic field was used during the growth phase, to probe the effect of a high plasma density on the structure and the growth rate. As the plasma density profile is a bell-shape in front of the substrate, the uniformity of the morphology and growth rate on the wafer will be affected, see figure (7.10) below.

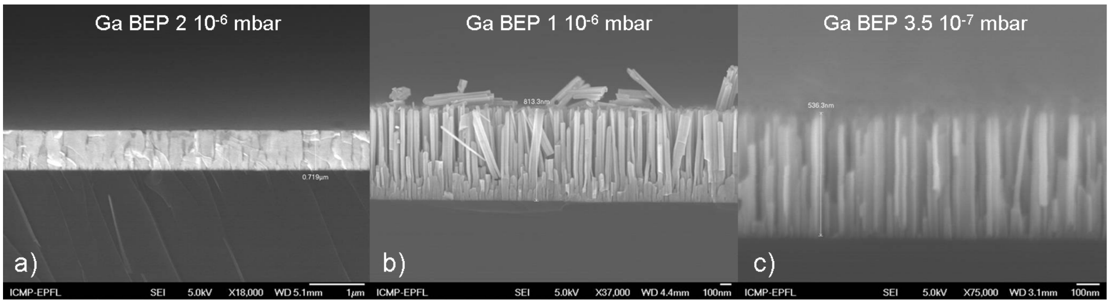

Figure 7.8: SEM images from the side of wafers grown at different Ga BEP pressures: *(a)* $2{\cdot}10^{-6}$ mbar, *(b)* $1{\cdot}10^{-6}$ mbar and *(c)* $3.5{\cdot}10^{-7}$ mbar, with the following plasma parameters: $I_{ARC} = 10$ A, N_2 pressure $3.4 \cdot 10^{-3}$ mbar, Ar pressure $2.1 \cdot 10^{-3}$ mbar, $B_{field} = 32$ G, substrate temperature 600°C during growth.

Figure (7.8) presents SEM images from the side of wafers grown with the same nitrogen plasma but with different Ga BEP, in order to probe the change of morphology from 2D to 3D. With increasing ratio N/Ga (Ga BEP is decreased with constant N density), the structure passes from 2D bulk layer *(a)* to 3D nanocolumns *(c)* with an intermediate step with both morphologies *(b)*. This is the same observation than with the RF gridded plasma source, except for the value of the ratio. In fact with the DC plasma source, the N/Ga ratio passes from 2.5 to 15 when the Ga BEP passes from $2 \cdot 10^{-6}$ mbar to $3.5 \cdot 10^{-7}$ mbar. To calculate this ratio, the ratio between the partial pressure of nitrogen and the Ga in the mixture, as well as the ratio between the atomic nitrogen and neutral molecular nitrogen densities from table (3.3) have been used. The absolute values of the N/Ga ratio are different but the trend is the same: the higher the ratio, the more nanocolumnar shaped layers.

The RHEED pattern from the layers presented in figure (7.8b) and (7.8c) are shown in figure (7.9). Both layers exhibit dots, meaning the presence of 3D structures, but the higher Ga BEP layer presents traces of lines, indicating a partial recovery of the layer, due to the increased density of Ga available for the growth. On the pattern, no chamfer is seen, showing that there is no thermal constraint on the layer. To obtain the layer without constraints the cooling down procedure after the deposition phase has been modified.

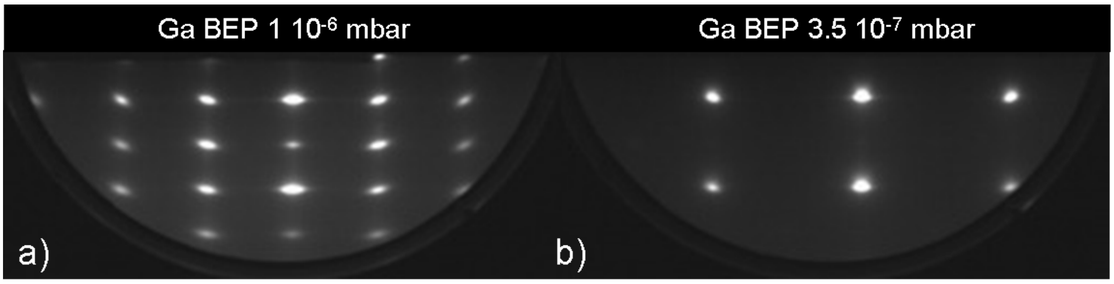

Figure 7.9: RHEED pattern showing the surface structure of wafers grown at different Ga BEP pressures: *(a)* $1 \cdot 10^{-6}$ mbar, *(b)* $3.5 \cdot 10^{-7}$ mbar, with the following plasma parameters: $I_{ARC} = 10$ A, N_2 pressure $3.4 \cdot 10^{-3}$ mbar, Ar pressure $2.1 \cdot 10^{-3}$ mbar, $B_{field} = 32$ G, substrate temperature 600°C during growth.

The change of the Ga BEP had the advantage to modify the ratio N/Ga without changing the plasma parameters. In a second step the Ga BEP was fixed to $1 \cdot 10^{-6}$ mbar and the discharge current, argon pressure and the magnetic field strength were varied. It appeared that these changes had only a slight effect on the morphology of the layer and the density of the nanocolumns. The Ga BEP is so low that the growth regime is only the ”N rich” regime, even in the absence of magnetic field, because only the plasma density is changed. Thus the impact of the parameters is low on the morphology. Another parameter which has been varied is the temperature of the substrate during the growth. It has been increased from 600°C to 800°C. The resulting effect on the morphology is shown in figure (7.10).

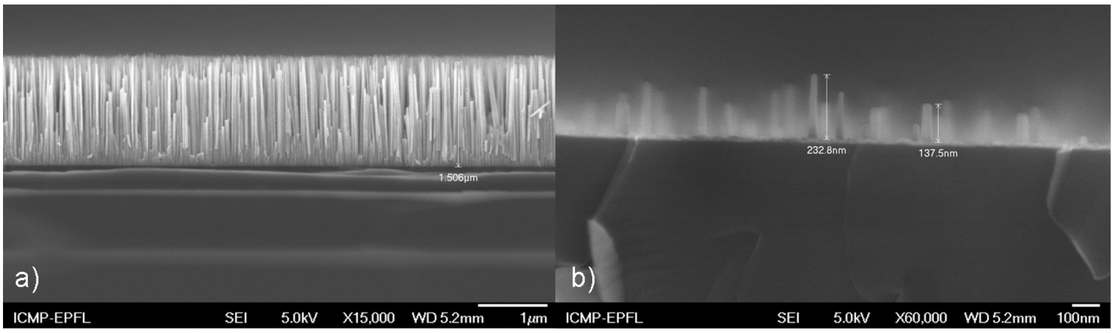

Figure 7.10: SEM images from the side of wafers grown at different temperatures: *(a)* 600°C and *(b)* 800°C, with the following plasma parameters: $I_{ARC} = 10$ A, Ga BEP $1 \cdot 10^{-6}$ mbar, N_2 pressure $3.4 \cdot 10^{-3}$ mbar, Ar pressure $2.1 \cdot 10^{-3}$ mbar, $B_{field} = 32$ G.

The expected effect was to increase the mobility of the Ga atoms on the substrate, lowering the nanocolumns density because of the increased distance between the islands (attachment points for the growth). The effect seen is the desorption of the GaN during the growth, because the temperature on the substrate is too high. In fact the confined plasma brings additional heat to the substrate, whose temperature becomes locally higher than the desorption threshold. This affects the growth rate, the nanocolumns are only

200 nm high (figure (7.10b)) with the same growth time as in *(a)*, where their height is 1500 nm. The hot and dense plasma column formed by the magnetic field leads to an additional heater, but the bell-shape of the plasma density profile suggests that it is a local effect. To corroborate this hypothesis, SEM images of the edge of the wafers were done, shown in figure (7.11), with the comparison with the centre of the wafers.

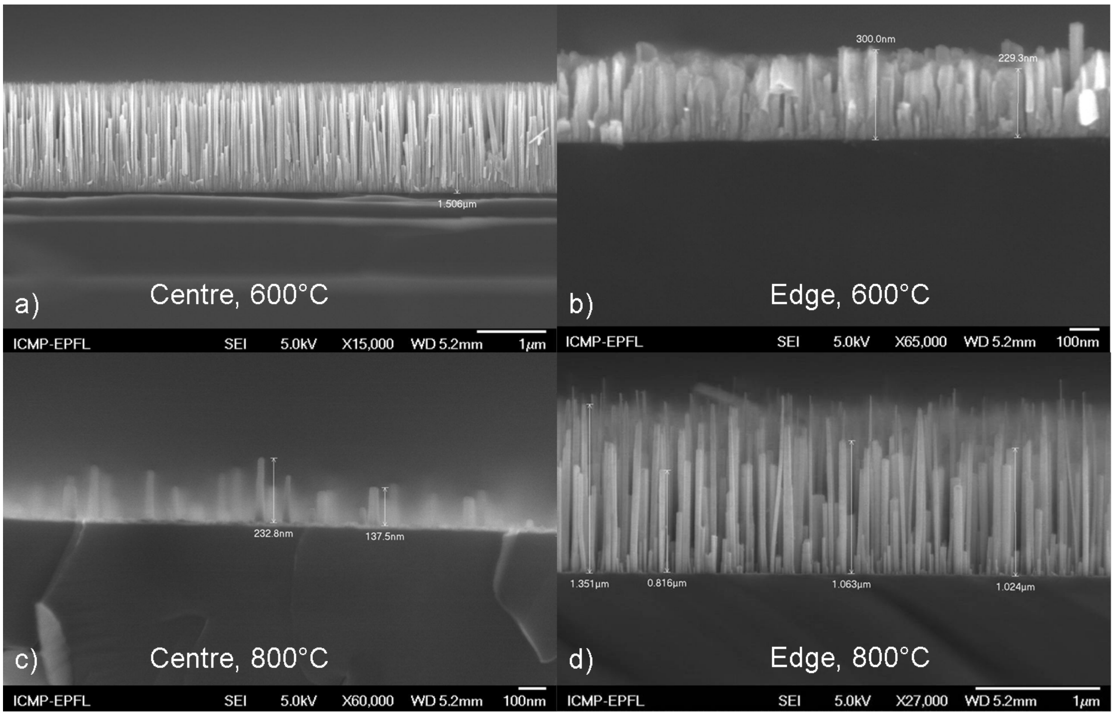

Figure 7.11: SEM images from the side of wafers showing the non-uniformity of the deposition under different growth conditions. *(a)+(c)* centre of wafer, *(b)+(d)* edge of wafer, same wafers as in figure (7.10).

The wafer grown at 600°C shown in *(a)* and *(b)* exhibits a higher growth rate in the centre than in the edges, because the size of the nanocolumns is larger in the centre, about a factor 5 with respect to the nanocolumns at the edges of the wafer. The morphology of the wafer is more or less the same, except that at the edges the recovery of the layer is more pronounced. The difference of height of the nanocolumns follows the plasma density profile from a columnar plasma shape (figure (5.16)). The ratio N/Ga is higher in the centre of the wafer, leading to "pure" nanocolumnar growth, whereas in the edges the ratio is lower meaning a mix between 2D and 3D growth regime. The substrate grown at 800°C (*(c)* and *(d)* on figure) exhibits a different behaviour. In fact in the centre of the wafer the size of the nanocolumns is lower than the one of the nanocolumns in the edges of the wafer. The reason for this inversion of size might be the increase of the mobility of the species. The hot dense plasma column heats the centre of the wafer above the desorption threshold temperature, see figure (7.12b). The GaN formed starts to be re-evaporated, which is not the case in the edges of the wafer. The recovery of the layer in the edges is more pronounced at the lower temperature of growth.

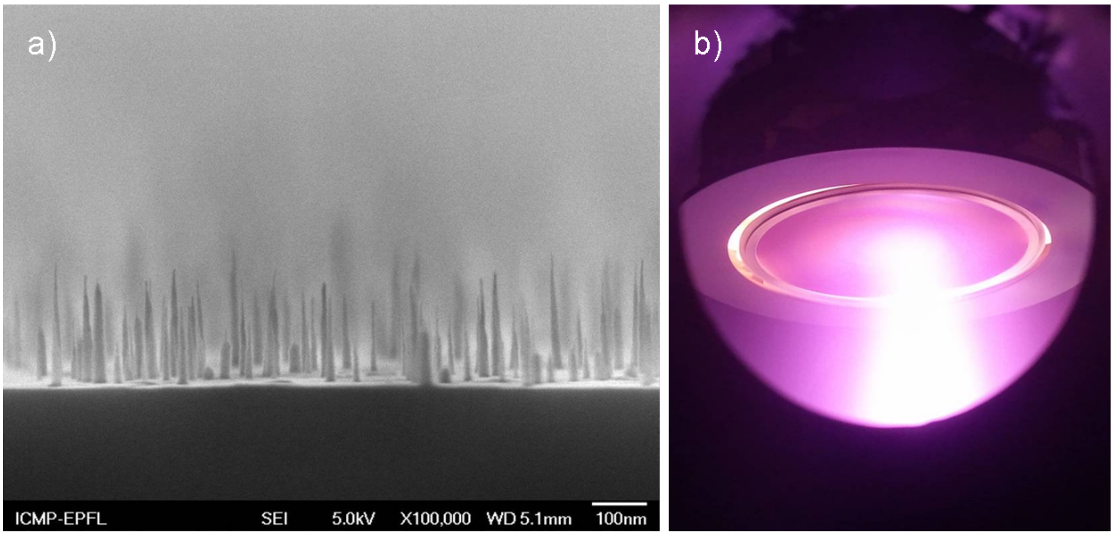

Figure 7.12: *(a)* SEM image from the side of the centre of a wafer grown at 800°C, showing the etching of the nanocolumns, the following plasma parameters were used: $I_{ARC} = 10$ A, Ga BEP $2 \cdot 10^{-6}$ mbar, N_2 pressure $3.4 \cdot 10^{-3}$ mbar, Ar pressure $2.1 \cdot 10^{-3}$ mbar, $B_{field} = 32$ G. *(b)* Picture of a wafer during the GaN growth, showing the hot and dense plasma column hitting the wafer.

Another explanation for the absence of growth in the centre of the wafer might be the etching of the wafer by ions hitting the surface. To illustrate this effect the Ga BEP was increased in order to grow higher nanocolumns. Figure (7.12) shows a SEM image of the centre of this wafer, grown with the same temperature of 800°C. The nanocolumn density is increased with respect to the one found in figure (7.11c), but their height is the same. The resolution of the picture has been increased to observe more in details the shape of the nanocolumns. They exhibit a large base for a tiny top, as if they have been etched during their growth. The ion bombardment from N_2^+, Ga^+ or Ar^+ ions can be the source of etching, mostly in the centre, due to the magnetic field.

7.3 Growth rates studies

The morphology of the layer grown is dependent on the ratio N/Ga, which can be varied using both plasma sources. The growth rate was then an important motivation for the change of the RF plasma source to the DC plasma source, as the plasma density is higher with this type of source. The growth rates are measured *in situ* using the laser reflectometry system or can be deduced from the SEM images, knowing the growth time. With the RF plasma source laser reflectometry was used and permits to make some multi-layers processes, allowing scanning a parameter during the same growth procedure. The analysis of each oscillation during the same run permits to extract the growth rate of the desired condition. With the DC plasma source, certainly due to the heating of the substrate by the plasma, the signal of the laser could not be detected, due to the bending of the surface and/or the use of the magnetic field. The growth rates were then determined by the layer thickness on the SEM images. This method has the advantage that the growth rate can be determined locally on the substrate, due to the non uniformity of the deposition, because of the use of magnetic field.

7.3.1 Using the gridded RF plasma source

Using the laser reflectometry system some parameters have been varied, to explore the parameter space. The first parameter which has been probed is the Ga flow on the substrate, as a function of the nitrogen pressure, to see the impact of the stoichiometry on the growth rate. Figure (7.13) shows the evolution of the growth rate for different Ga BEP as a function of the nitrogen pressure. The point where the growth rate is maximum shifts with the increasing BEP. In fact as the quantity of Ga available for the growth increases, the quantity of atomic nitrogen should also be increased to keep the maximal growth rate obtained at the stoichiometric point. Below this point, i.e. when the nitrogen pressure is lower than the pressure of the stoichiometric point, the Ga is in excess ("Ga rich" regime), and the limiting factor is the atomic nitrogen. This explain the linear increase to the maximal growth rate, because the atomic nitrogen density linearly increases with the pressure.

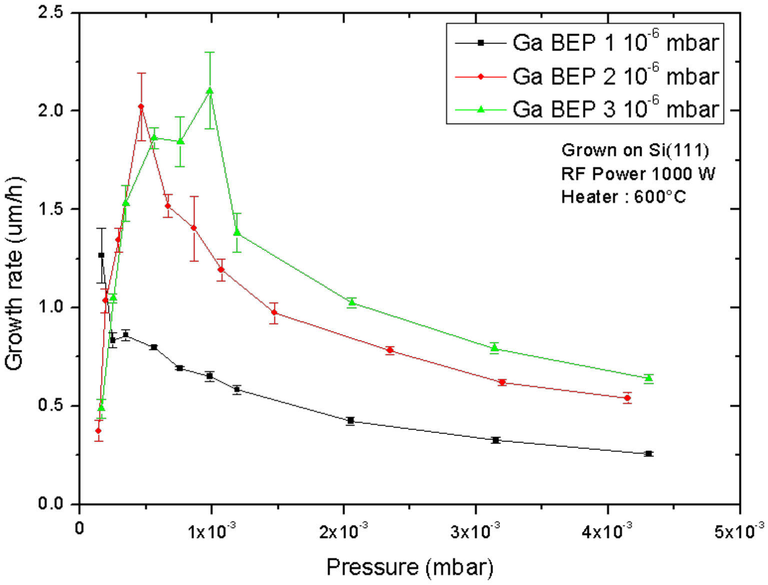

Figure 7.13: Growth rate with various Ga BEP as a function of nitrogen pressure.

When the pressure is greater than the one needed for the stoichiometry, the atomic nitrogen is in excess ("N rich" regime). Normally, from this point, the growth rate should be constant, as it is limited by the quantity of Ga available. Nevertheless on the graph the growth rate is decreasing with the increasing nitrogen pressure. This is due to the scattering of the Ga by the nitrogen. This has two effects: reducing the growth rate and increasing the N/Ga ratio, leading to the growth of nanocolumns. On the curve with the lowest Ga BEP, the stoichiometric point is not reached, as the nitrogen pressure needed for this point is below the limit for the operating of the RF plasma source. In the "N rich" regime the growth rate is increased with increasing Ga BEP, confirmed by the measurements. The distance between the Ga effusion cell and the substrate plays an important role, as it changes the amount of Ga available for the growth, when the cell is heated at a fixed temperature. This explains that, in this work, no higher Ga BEP than $3 \cdot 10^{-6}$ mbar was maintained for this type of measurement to prevent breaking the Ga effusion cell.

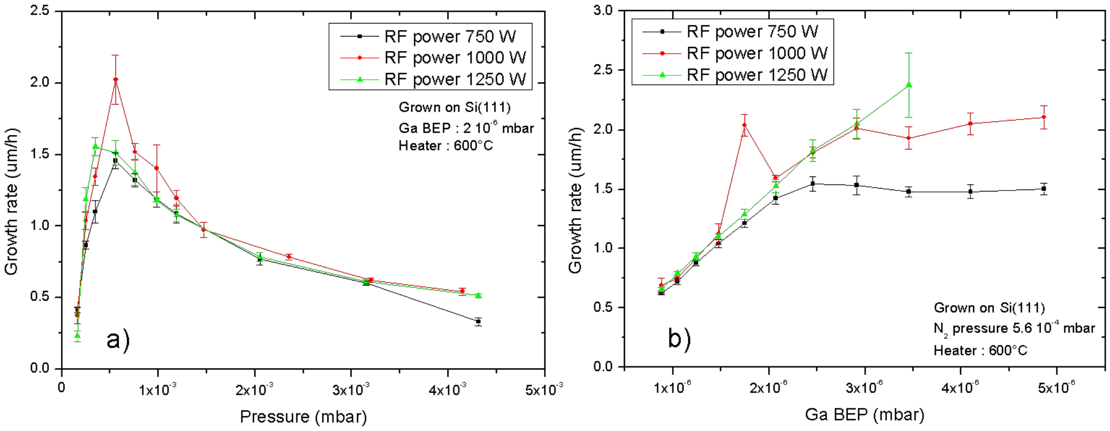

Figure 7.14: Growth rate as a function of the RF power at *(a)* constant Ga BEP with various N_2 pressure and *(b)* fixed N_2 pressure with increasing Ga BEP.

Figure (7.14) shows the impact of the RF power on the growth rate with changes of *(a)* nitrogen pressure and *(b)* Ga BEP. In this type of measurement, due to the short time required for the growth rate measurement, higher Ga BEP have been tested. In fact the cell was heated up to the maximal limit specified, but for a short time, which permitted to probe the effect of higher Ga densities on the substrate. Three RF powers were tested with a fixed Ga BEP and a varying nitrogen pressure (figure (7.14a)). The curves are similar and are very similar in the "N rich" regime. As only the plasma density is changing, and not the composition, it explains the change in slopes before the stoichiometry in the "Ga rich" regime. In fact at a fixed N_2 pressure the density of atomic nitrogen is increased with the power, leading to an increase of the growth rate, due to more material available for the growth. At pressures higher than the stoichiometry, the slopes of the growth rates are identical, due to the scattering of the Ga. For all RF powers tested the growth is in "N rich" regime, thus the rate is determined by the quantity of Ga reaching the surface.

The stoichiometric point is shifted to lower N_2 pressures if the RF power is increased, due to the fixed Ga BEP and increasing plasma density. This is seen more explicitly in figure (7.14b). On this figure the growth rates are shown as a function of the Ga BEP for a fixed N_2 pressure and for different RF powers. The effect of the power is to increase the N atomic density without changing the pressure. For BEP lower than $2 \cdot 10^{-6}$ mbar, the curves are superimposed, because of the "N rich" regime, due to the low Ga density on the substrate. The point reaching 2 μm/h for 1000 W seems to be out of the measurement error. At higher Ga flows, there is a formation of plateau. This is due to the "Ga rich" regime of the growth. The point for which the growth changes its regime is dependent on the RF power, because it determines the N atomic density (N_2 pressure is fixed). The pressure is low enough to not scatter the Ga, leading to plateaus of growth rates and not decreasing values as in figure (7.13). The more nitrogen available for the growth, the higher the growth rate and thus the plateau values. The same argument explains the stoichiometric point shifting to higher Ga BEP. For 1250 W the stoichiometric point has not been reached in this measurement run.

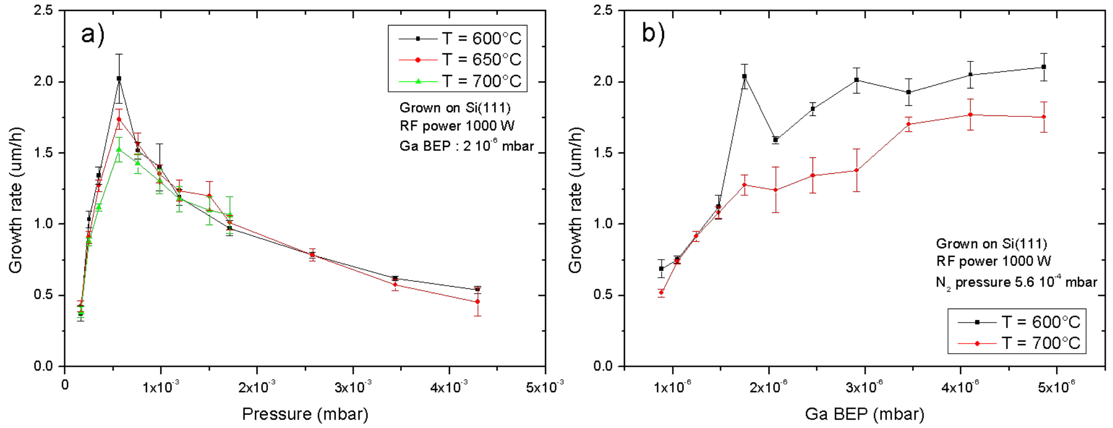

Figure 7.15: Substrate temperature effect on the growth rate: *(a)* constant Ga BEP with various N_2 pressure and *(b)* fixed N_2 pressure with increasing Ga BEP.

The effect of the substrate temperature on growth rate is shown in figures (7.15) and (7.16). The first study was to vary the N_2 pressure with fixed Ga BEP and RF power. It is seen that the growth rates are globally lower with increasing growth temperature. The same stoichiometric point is obtained in these conditions, due to the unchanged ratio N/Ga. The slope of the growth rate increase at low nitrogen pressures is depending on the temperature, whereas the same evolution is seen at pressures higher than the stoichiometry. The second study was made at fixed N_2 pressure and RF power and increasing Ga BEP. The same conclusion can be drawn regarding the temperature effect: the growth rate is lower when the temperature is increased. At low Ga BEP the atomic nitrogen is in excess, as in figure (7.14b), and the growth rate increases linearly with the Ga BEP. Then the growth rate evolution flattens. The BEP at which it occurs depends on the substrate temperature. The reason for the flattening is unknown. This can come from a higher mobility of the Ga on the surface, lowering the attachment spots; or from a less effective nitridation because of a too high temperature; or from a desorption of the

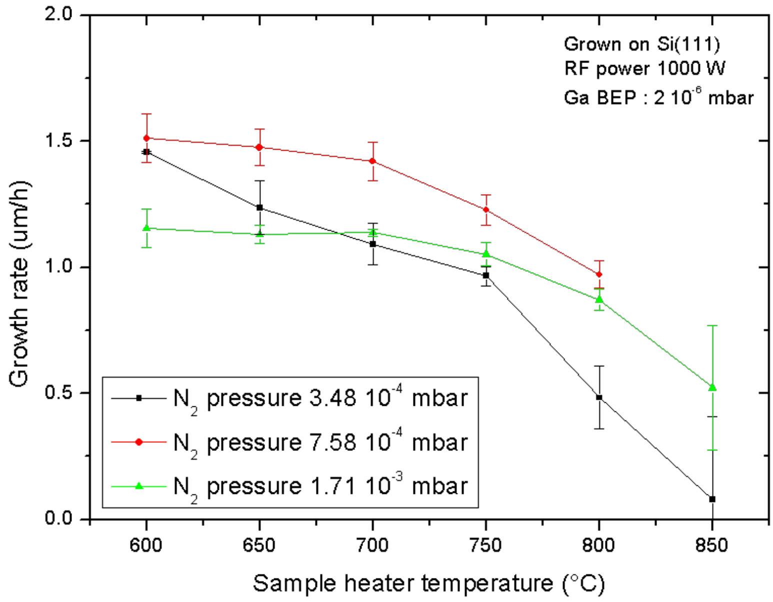

Figure 7.16: Growth rate as a function of the substrate heater temperature with fixed Ga BEP and RF power for different N_2 pressures.

nitrogen at the surface. No distinction could be made between the hypotheses.

Higher temperatures for the substrate have been tested, allowing the desorption of GaN. The temperature threshold of GaN decomposition is about 830°C, but a significative decay of the growth rate is seen at temperature lower than this threshold. In fact, for temperatures lower than 700°C, the growth rate is relatively constant for all nitrogen pressures tested (figure (7.16)). As the Ga BEP and the RF power are fixed, for each curve the atomic nitrogen is also fixed, leading to a constant N/Ga ratio. This explains the plateaus at low temperatures. From about 700°C all curves show a decreasing trend. This indicates that the formation of GaN on the surface is less efficient. Nevertheless at high N_2 pressures the point where the growth rate decreases down to 0 seems to be at higher substrate temperature.

The conclusion of the temperature study is that to maximize the growth rate the temperature should not be greater than 700°C, and should also be higher than a certain value, not determined in this work. However the temperature range is far below the required growth temperatures of the MOCVD technique. The growth rate values between 600°C and 700°C are very similar for many growth conditions (Ga BEP and N_2 pressure). As these growth rate measurements were done on multi-layers samples, the morphology of the GaN grown has not been determined by SEM or RHEED.

7.3.2 Using the DC plasma source

The additional heating created by the plasma column due to the use of the magnetic field made the reflectometry system unusable with the DC plasma source. In fact the reflected signal could not be detected, certainly due to the bending of the centre of the substrate. The growth rates could only be determined by analysing the thickness of the deposited layer by SEM images, knowing the growth time. For convenience, this latter was fixed at 20 minutes. With this method for the determination of the growth rate, only one growth condition could be experimented at once, not as with the RF plasma source, where multi-conditions layers could be grown.

As already said, most of the wafers grown presented nanocolumns and the goal was to control their density, thus no real study on the growth rates was done. The non-uniformity on the wafer size is also a factor which degrades the notion of growth rate. In fact the claim of a growth rate of 7 μm/h is interesting, but if it is only on a third of a 4” wafer, the industrial interest becomes less important.

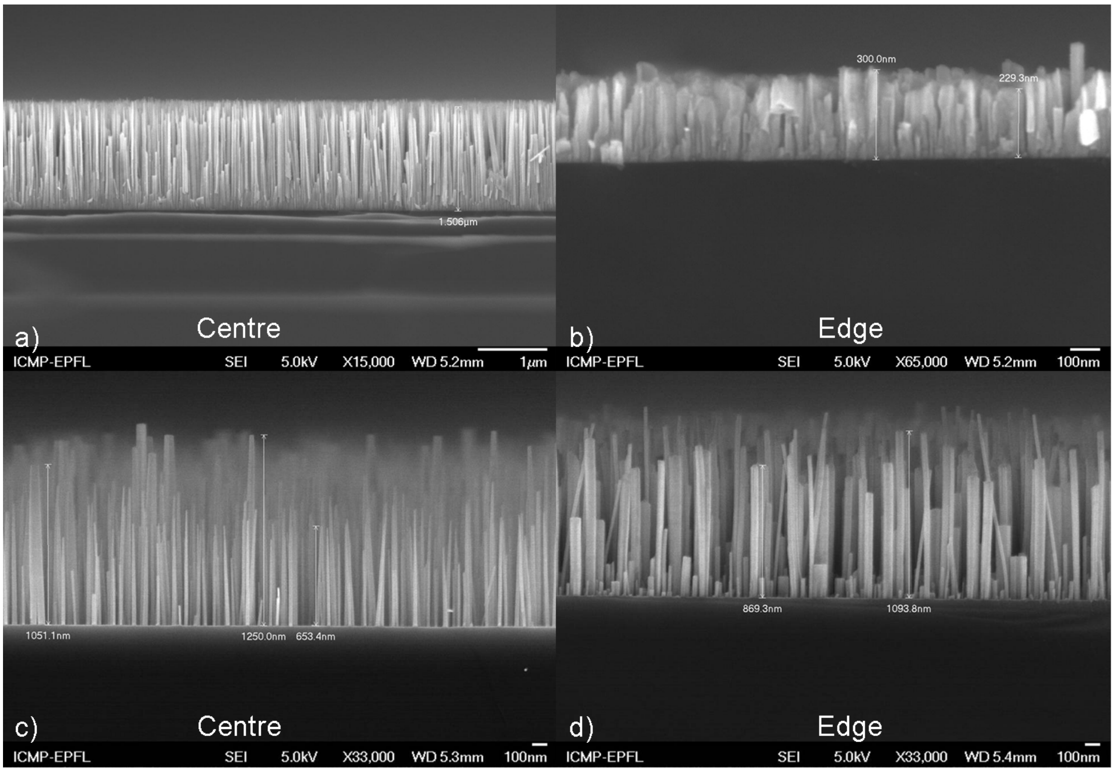

Figure 7.17: SEM image from the side of some wafers grown at high growth rates: *(a)+(b)* growth rate of 4.5 μm/h in the centre and 0.6 μm/h in the edge, *(c)+(d)* 3 μm/h in the centre and 2.7 μm/h in the edge.

Figures (7.17) and (7.18) present SEM images of the best growth rates obtained with the DC plasma source. The maximal growth rate obtained with the RF plasma source with the grid was 2 μm/h and with the DC plasma source the maximal obtained is 6.9 μm/h,

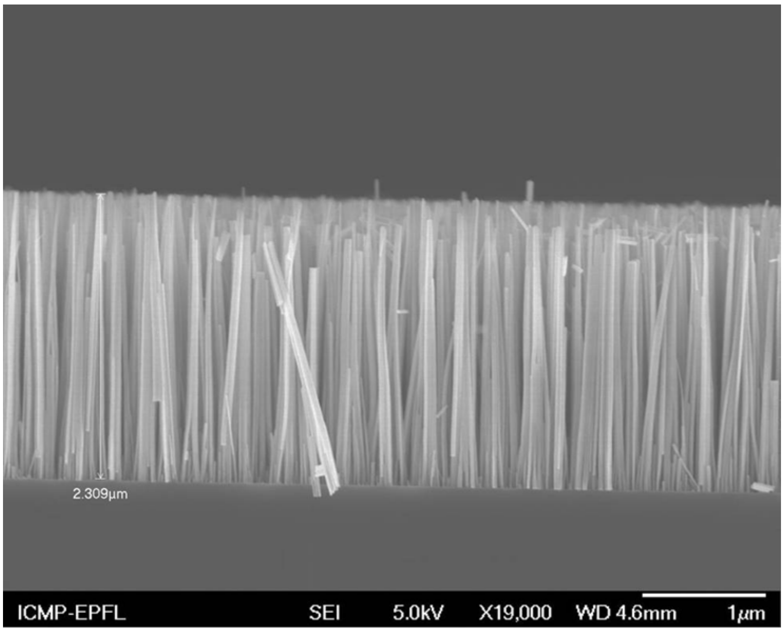

Figure 7.18: SEM image from the side of the edge of the maximal growth rate of 6.9 μm/h obtained with both plasma sources, with the following plasma parameters: I$_{ARC} = 20$ A, Ga BEP $2 \cdot 10^{-6}$ mbar, N_2 pressure $3.4 \cdot 10^{-3}$ mbar, Ar pressure $2.1 \cdot 10^{-3}$ mbar, B$_{field} = 32$ G, substrate temperature during growth 800°C, growth time 20 minutes.

but the uniformity on this wafer is poor. In fact the growth rate in the centre of the wafer differs from the one of the edges, due to the magnetic field, which brings more atomic nitrogen in the centre. The maximal growth rate in the centre of the wafer (figure (7.17a)) was 4.5 μm/h, in the following growth conditions : I$_{ARC} = 10$ A, Ga BEP $1 \cdot 10^{-6}$ mbar, N_2 pressure $3.4 \cdot 10^{-3}$ mbar, Ar pressure $2.1 \cdot 10^{-3}$ mbar, B$_{field} = 32$ G and a growth temperature of 600°C. The wafer presents a large non uniformity, as the growth rate decreases to 0.6 μm/h in the edges. The most uniform high speed growth is presented in the figure (7.17c,d), with a growth rate of about 3 μm/h on the whole wafer. To achieve this uniformity the pressure in the chamber was increased by reducing the pumping speed, keeping the same gas flows. The ultimate growth rate was 6.9 μm/h (figure (7.18)), in the edge of a wafer where a strong etching occurred in the centre due to the high growth temperature (800°C) and magnetic field. It is the same wafer as in figure (7.12).

7.4 Conclusion

This chapter presented the results of the deposition procedure with both plasma sources without AlN nucleation layer, in terms of surface morphology and growth rate. As the plasma composition is unchanged, only the plasma density plays a role. The effect of the other N_2 species present in the plasma could not be investigated. The GaN growths using the RF plasma source showed that, depending on the growth regime, the morphology might be 2D compact layer or 3D nanocolumns. The growth regime is determined by the density ratio N/Ga of atomic nitrogen and gallium atoms reaching the surface. With low values of this ratio, the growth is in the ”Ga rich” regime, leading to 2D compact layers, and with higher values of this ratio, the ”N rich” regime leads to nanocolumnar growth. The values of the ratio are different between both plasma sources. As the plasma density is higher with the DC plasma source, the ”N rich” regime is easier found with this source. The growths with the RF plasma source showed a good uniformity along the wafer, due to the uniform patter of the plasma density. The magnetic field used to increase the atomic nitrogen density with the DC plasma source also generates a non-uniformity on the 4” wafer, and might lead to the desorption of the growth during the deposition procedure. The etching of the GaN nanocolumns by the ion bombardment has also been observed. Growth rate studies with the RF plasma source showed the impact of the growth temperature when approaching 750°C.

Final conclusion and outlook

This thesis work presented an investigation of nitrogen plasmas used for the deposition of structured GaN layers. Due to the use of effusion cells for the evaporation of Ga, the gas pressure range in the deposition chamber is limited to $10^{-4} - 10^{-2}$ mbar. In this pressure range, particle diffusion is important, and some processes in the plasma composition determination can be neglected, such as heavy particle and three-body collisions. The changes in the plasma composition, determined through OES, T_e and plasma density, both determined using Langmuir probes, was investigated with the change of important process parameters, such as the gas pressure, input power and magnetic field. Many electrical configurations of the reactor were tested in order to change the plasma composition, which has been revealed to be very robust. The behaviour of the plasma composition and the various plasma parameters is similar in each configuration tested using both the RF and DC plasma sources, leading to changes only in plasma density and in density uniformity. The similar composition is explained by the limited gas pressure range, which determines the reaction rates through the dependence of T_e. The density fluctuates depending on the configuration and is found to be higher using the DC plasma source with the use of magnetic field. The increase of density influences also the profile of density uniformity along the wafer size, as the profiles become bell-shaped.

OES technique to study the changes in T_e was set up, based on the ratio of the total intensities of different excited states, and the results obtained were in good agreement with the measurements of the Langmuir probe. The uniformity of the plasma investigated in the same way gave similar results with both diagnostics. OES is found to be a powerful and non-intrusive tool for the plasma characterisation, even if the interpretation of the spectra is somewhat complex.

Three models were developed to simulate the plasma parameters (T_e and n_e) and the plasma composition. The particle balance model predicted higher electron temperatures than the measured ones, certainly due to the strong hypothesis of uniform density. In the case of the RF plasma source with a grid, the predicted density by the model is overestimated. Furthermore, two models were developed to estimate better the plasma composition: The corona model, with only one populating and one de-populating process, and the CR model, taking into account other mechanisms. This latter has also been used to determine an analytical value for T_e. The comparison with the experiment was done through the ratio of density of the radiative states $N_2(C)$ and $N_2(B)$. Good agreement was found between the CR model and the experimental electron temperatures, and the density ratios. The key mechanisms leading to nitrogen plasmas in such low pressures were thus identified. The model can be run with a custom EEDF, in this thesis work a Maxwell and a beam-Maxwell EEDF were used, as observed experimentally with both plasma sources.

Besides plasma characterisation, GaN depositions were made to correlate the plasma parameters and the morphology of the layers. Depositions made using both plasma sources showed 2D compact layer and 3D nanocolumns morphology, depending on the ratio of densities N/Ga. The lower value of the ratio leads to a 2D compact layer morphology due to the abundance of Ga, but with increasing ratio, the morphology shows a transition with both regimes: 3D columns starts to grow on the compact layer. If the atomic nitrogen density is increased only 3D nanocolumns form on the substrate. The uniformity of the deposition is linked to the plasma density uniformity, as it determines also the atomic nitrogen density. Using the DC plasma source the growth rate is higher than with the RF plasma source, explained by the globally higher plasma density. GaN was deposited directly on Si(111) wafer, without the help of an AlN nucleation layer, lowering the time needed for a deposition procedure.

Impact for the industrial project

The plasma characterisation performed during this thesis work highlighted that the plasma only acts as an atomic nitrogen source even with the higher N_2 pressure than in other PA-MBE systems, whose density can be tuned with external parameters, such as the nitrogen pressure, input power, plasma source or magnetic field. As the plasma composition is similar in each configuration tested, the key points for the industry are the uniformity of the deposited layers and the growth rates. The plasma source which showed the best density uniformity is the RF plasma source, whereas the highest growth rates were obtained with the DC plasma source with magnetic field. Nevertheless, the RF plasma source without the extraction grid is a good compromise between both plasma density and its uniformity.

The pressure limitation, due to the use of the effusion cell, fixes the plasma composition, thus being not a parameter influencing the growth. Other Ga injection procedures are known but their use requires major changes in the deposition system. For example the trimethylgallium (TMG) is a toxic liquid containing Ga which is used in MOCVD. This compound needs the installation of many safety factors to prevent health issues.

The effusion cell also limits the Ga flow to the substrate, because of the limitation of the heating capacity of the filaments inside the cell. As shown, the atomic nitrogen flow dominates in almost all pressures tested. Thus if the Ga flow would have been higher, the growth rates certainly would be increased, and the growth of 2D compact layers directly on Si(111) would have taken less time than other techniques, becoming interesting for industrial application. The method of deposition used in this thesis work is not yet suitable for industrial application, because the density of nanocolumns is not controllable and the quality of the deposited material is poor. Nevertheless the growth of nanocolumns directly on a bare Si(111) was demonstrated.

Outlook

The thesis focused on the plasma characterisation and modelling in order to correlate the plasma parameters to the deposited layer morphology. Nevertheless some more investigations could be made to still increase the knowledge of such procedure.

Langmuir probe profiles measurements, far from the DC plasma source using the multi-holes separation plate and structured anode or steering wheel anode set floating with respect to the walls, showed a high and uniform plasma density when using the magnetic field. OES measurements could confirm the trends shown by the Langmuir probe, as it is non-intrusive, and even evaluate faster the changes in T_e. The expected deposition layers using these particular electrical configurations are 3D nanocolumnar growths with very high growth rates. The limiting factor is the incoming Ga flow to transit to 2D compact layer. The advantage of those configurations is that the high energetic electron beam is stopped by the anode, thus limiting the etching of the growing layer. To guarantee the uniformity of the deposited layers, the RF plasma source is preferred. To increase the atomic nitrogen density to increase the growth rates, the extraction grid can be removed. The results in terms of growth rates might be the same as with the DC plasma source, with a higher uniformity of the deposition.

To increase the Ga flow on the substrate, another Ga source is needed. This implies several hardware modifications on the existing reactor. Nevertheless, high growth rate 2D compact layers could be reached, increasing the interest for industrial applications. If the effusion cell concept is kept, in order to increase the Ga density on the substrate, by reducing for example the distance between the effusion cell and the substrate, the reactor design should also be modified. The reactor used shows a large unused volume for the deposition, increasing the losses of Ga by elastic collisions. A smaller reactor, for example, a glass cylinder with a diameter slightly larger than the one of the wafer, would decrease the losses by diffusion. An external plasma source, such as inductively coupled plasmas (ICP) or helicon plasmas, could be used in such small reactors. The atomic nitrogen production with this type of source is expected to be in the same order of magnitude, or even higher, than the one obtained with the DC plasma source with magnetic field.

In order to increase the Ga flow on the substrate, another idea is to heat the reactor walls above 800°C, the temperature preventing GaN to form on the walls of the reactor. The reactor size should again be reduced to lower the energy required to maintain the walls at such a high temperature. This situation is similar to the one of MOCVD reactors.

Finally the models could be improved and be extrapolated into 2D modelling. The magnetisation of the electrons, density profiles and diffusion could then be implemented and Ga scattering could be modelled. This would help to find an optimal reactor design to maximise the deposition of GaN. In this sense, particle-in-cell simulation could be set up, to model the trajectory of the particles in a given geometry, which may be as simple as in our case or more complex.

Bibliography

[1] A. Botchkarev et al., *Properties of GaN films grown under Ga and N rich conditions with plasma enhanced molecular beam epitaxy*, J. Appl. Phys. **77** 4455 (1995)

[2] J. Kuznia et al., *Influence of buffer layers on the deposition of high quality single crystal GaN over sapphire substrates*, J. Appl. Phys. **73** (9) 4700–4702 (1993)

[3] A. Ohtani, K. Stevens and R. Beresford, *Microstructure and photoluminescence of GaN grown on Si (111) by plasma-assisted molecular beam epitaxy*, Appl. Phys. Lett. **65** (1) 61–63 (1994)

[4] A. Krost and A. Dadgar, *GaN-based optoelectronics on silicon substrates*, Materials Science and Engineering: B **93** (1) 77–84 (2002)

[5] Y. Nakada, I. Aksenov and H. Okumura, *GaN heteroepitaxial growth on silicon nitride buffer layers formed on Si (111) surfaces by plasma-assisted molecular beam epitaxy*, Appl. Phys. Lett. **73** (6) 827–829 (1998)

[6] M. Sanchez-Garcia et al., *The effect of the III/V ratio and substrate temperature on the morphology and properties of GaN-and AlN-layers grown by molecular beam epitaxy on Si (1 1 1)*, J. Cryst. Growth **183** (1) 23–30 (1998)

[7] R. Debnath et al., *Mechanism of molecular beam epitaxy growth of GaN nanowires on Si (111)*, Appl. Phys. Lett. **90** (12) 123117–123117 (2007)

[8] F. Furtmayr et al., *Nucleation and growth of GaN nanorods on Si (111) surfaces by plasma-assisted molecular beam epitaxy-The influence of Si-and Mg-doping*, J. Appl. Phys. **104** (3) 034309–034309 (2008)

[9] S. Fernández-Garrido et al., *A growth diagram for plasma-assisted molecular beam epitaxy of GaN nanocolumns on Si (111)*, J. Appl. Phys. **106** (12) 126102–126102 (2009)

[10] A. Trampert et al., *TEM study of (Ga, Al) N nanocolumns and embedded GaN nanodiscs*, in *Conference Series - Institute of Physics*, Philadelphia; Institute of Physics; 1999 (2003), volume 180, pp. 167–170

[11] C. Foxon et al., *A complementary geometric model for the growth of GaN nanocolumns prepared by plasma-assisted molecular beam epitaxy*, J. Cryst. Growth **311** (13) 3423–3427 (2009)

[12] H. Schmidt et al., *Improving plasma uniformity using lens-shaped electrodes in a large area very high frequency reactor*, J. Appl. Phys. **95** (9) 4559–4564 (2004)

[13] M. Gindrat, *Characterization of supersonic low pressure plasma jets*, Ph.D. thesis, École Polytechnique Fédérale de Lausanne (EPFL) (2004)

[14] W. Yinglong, *Friction and wear performances of detonation-gun-and plasma-sprayed ceramic and cermet hard coatings under dry friction*, Wear **161** (1) 69–78 (1993)

[15] H. Prengel, W. Pfouts and A. Santhanam, *State of the art in hard coatings for carbide cutting tools*, Surf Coat Technol **102** (3) 183–190 (1998)

[16] A. Sublet et al., *Atmospheric and sub-atmospheric dielectric barrier discharges in helium and nitrogen*, Plasma Sources Sci. Technol. **15** (4) 627 (2006)

[17] M. Ricci et al., *Influence of Argon and Nitrogen Admixture in HMDSO/O_2 Plasmas onto Powder Formation*, Plasma Processes Polym. **8** (2) 108–117 (2011)

[18] J. Pelletier, *La stérilisation par le procédé plasma*, Agressologie **33** 105–110 (1992)

[19] M. Laroussi, *Sterilization of contaminated matter with an atmospheric pressure plasma*, Plasma Science, IEEE Transactions on **24** (3) 1188–1191 (1996)

[20] J. H. Noh et al., *Surface modification of polytetrafluoroethylene using atmospheric pressure plasma jet for medical application*, Surf. Coat. Technol. **201** (9) 5097–5101 (2007)

[21] J. Kolb et al., *Cold atmospheric pressure air plasma jet for medical applications*, Appl. Phys. Lett. **92** (24) 241501 (2008)

[22] R. Bussiahn et al., *The hairline plasma: An intermittent negative dc-corona discharge at atmospheric pressure for plasma medical applications*, Appl. Phys. Lett. **96** (14) 143701 (2010)

[23] J. Ehlbeck et al., *Low temperature atmospheric pressure plasma sources for microbial decontamination*, J. Phys. D: Appl. Phys. **44** (1) 013002 (2011)

[24] T. Delachaux et al., *Nitriding of tetragonal zirconia in a high current DC plasma source*, Thin Solid Films **425** (1) 113–116 (2003)

[25] P. Johnson and H. Randhawa, *Zirconium nitride films prepared by cathodic arc plasma deposition process*, Surf. Coat. Technol. **33** 53–62 (1987)

[26] R. Friedl and U. Fantz, *Spectral intensity of the N_2 emission in argon low-pressure arc discharges for lighting purposes*, New Journal of Physics **14** (4) 043016 (2012)

[27] S. Ivanov et al., *Plasma-assisted MBE growth and characterization of InN on sapphire*, J. Cryst. Growth **269** (1) 1–9 (2004)

[28] G. Tourbot et al., *Structural and optical properties of InGaN/GaN nanowire heterostructures grown by PA-MBE*, Nanotechnology **22** (7) 075601 (2011)

[29] J. Loureiro and C. Ferreira, *Electron excitation rates and transport parameters in direct-current* N_2 *discharges*, J. Phys. D: Appl. Phys. **22** 67 (1989)

[30] J. Loureiro, *Dissociation rate and N (4S) atom concentrations in a* N_2 *glow-discharge*, Chem. Phys. **157** (1-2) 157 – 168 (1991)

[31] J. Loureiro and C. Ferreira, *Coupled electron energy and vibrational distribution functions in stationary* N_2 *discharges*, J. Phys. D: Appl. Phys. **19** 17 (1986)

[32] J. Loureiro et al., *Non-equilibrium kinetics in* N_2 *discharges and post-discharges: a full picture by modelling and impact on the applications*, Plasma Sources Sci. Technol. **20** 024007 (2011)

[33] J. Loureiro and A. Ricard, *Electron and vibrational kinetics in an* N_2-H_2 *glow discharge with application to surface processes*, J. Phys. D: Appl. Phys. **26** 163 (1993)

[34] V. Guerra, E. Galiaskarov and J. Loureiro, *Dissociation mechanisms in nitrogen discharges*, Chem. Phys. Lett. **371** (5-6) 576 – 581 (2003)

[35] V. Guerra and J. Loureiro, *Electron and heavy particle kinetics in a low-pressure nitrogen glow discharge*, Plasma Sources Sci. Technol. **6** 361 (1997)

[36] V. Guerra, P. Sa and J. Loureiro, *Electron and metastable kinetics in the nitrogen afterglow*, Plasma Sources Sci. Technol. **12** S8 (2003)

[37] V. Guerra, P. A. Sa and J. Loureiro, *Kinetic modeling of low-pressure nitrogen discharges and post-discharges*, Eur. Phys. J. Appl. Phys. **28** 125 (2004)

[38] X. M. Zhu et al., *A novel method to determine electron density by optical emission spectroscopy in low-pressure nitrogen plasmas*, Phys. Plasmas **13** 123501 (2006)

[39] X. M. Zhu and Y. K. Pu, *Using OES to determine electron temperature and density in low-pressure nitrogen and argon plasmas*, Plasma Sources Sci. Technol. **17** 024002 (2008)

[40] X. M. Zhu and Y. K. Pu, *A simple collisional-radiative model for low-pressure argon discharges*, J. Phys. D: Appl. Phys. **40** 2533 (2007)

[41] X. M. Zhu and Y. K. Pu, *A molecular kinetic model for the optical emission spectroscopy technique in inductively coupled nitrogen plasma*, Phys. Plasmas **13** 063507 (2006)

[42] X. M. Zhu and Y. K. Pu, *Determining the electron temperature in inductively coupled nitrogen plasmas by optical emission spectroscopy with molecular kinetic effects*, Phys. Plasmas **12** 103501 (2005)

[43] D. Boris et al., *Controlling the electron energy distribution function of electron beam generated plasmas with molecular gas concentration: I. Experimental results*, Plasma Sources Sci. Technol. **22** (6) 065004 (2013)

[44] G. Petrov et al., *Controlling the electron energy distribution function of electron beam generated plasmas with molecular gas concentration: II. Numerical modeling*, Plasma Sources Sci. Technol. **22** (6) 065005 (2013)

[45] CTI project Nr. 8355.1 NMPP-NM, *Development of high throughput plasma processes for Gallium Nitride epitaxy at low substrate temperatures for applications in the field of lighting* (2009)

[46] L. Derendinger, *Design, Characterisation and Modelling of a High Current DC Arc Plasma Source for Silicon and Silicon Carbide Processing at Low Pressure*, Ph.D. thesis, École Polytechnique Fédérale de Lausanne (EPFL) (2008)

[47] C. Rosenblad et al., *Silicon epitaxy by low-energy plasma enhanced chemical vapor deposition*, Journal of Vacuum Science & Technology A: Vacuum, Surfaces, and Films **16** (5) 2785–2790 (1998)

[48] C. Rosenblad et al., *Epitaxial growth at high rates with LEPECVD*, Thin solid films **336** (1) 89–91 (1998)

[49] M. Weiler and R. Dahl, *High frequency plasma source, Patent number US 6,936,144 B2* (2005)

[50] M. Weiler et al., *Deposition of tetrahedral hydrogenated amorphous carbon using a novel electron cyclotron wave resonance reactor*, Appl. Phys. Lett. **72** (11) 1314–1316 (1998)

[51] H. Mott-Smith and I. Langmuir, *The theory of collectors in gaseous discharges*, Phys. Rev. **28** (4) 727 (1926)

[52] F. Chen and J. Chang, *Lecture notes on principles of plasma processing*, Springer (2003)

[53] M. Lieberman and A. Lichtenberg, *Principles of plasma discharges and materials processing*, Wiley-Blackwell (2005)

[54] N. Hershkowitz, *How Langmuir probes work*, Plasma Diagnostics **1** 113–183 (1989)

[55] A. Ricard, *Plasma Réactifs*, Societe Francaise du Vide (1995)

[56] D. Smith et al., *Efficient radiation production in a weakly ionized, low-pressure, nonequilibrium gallium-iodide positive column discharge plasma*, J. Phys. D: Appl. Phys. **40** 3842 (2007)

[57] E. Condon, *A theory of intensity distribution in band systems*, Phys. Rev. **28** (6) 1182 (1926)

[58] A. S. Coolidge, H. M. James and R. D. Present, *A Study of the Franck-Condon Principle*, The Journal of Chemical Physics **4** 193 (1936)

[59] F. Gilmore, R. Laher and P. Espy, *Franck-Condon Factors, r-Centroids, Electronic Transition Moments, and Einstein Coefficients for Many Nitrogen and Oxygen Band Systems*, J. Phys. Chem. Ref. Data **21** (5) 1005–1107 (1992)

[60] A. Einstein, *Über einen die Erzeugung und Verwandlung des Lichtes betreffenden heuristischen Gesichtspunkt*, Annalen der Physik **322** (6) 132–148 (1905)

[61] J. Levaton et al., *A detailed discussion of the* $N_2(C^3\Pi_u)$ *and* $N_2(X^1\Sigma_g^+)$ *vibrational temperatures in* N_2 *glow discharges*, Eur. Phys. J. Appl. Phys. **26** 59–64 (2004)

[62] B. Beaumont et al., *High quality GaN grown by MOVPE*, J. Cryst. Growth **170** (1) 316–320 (1997)

[63] H. Fitouri et al., *Laser-reflectometry monitoring of the GaN growth by MOVPE using SiN treatment: study and simulation*, physica status solidi (a) **202** (13) 2467–2473 (2005)

[64] B. Damilano, *Nanostructures (Ga,In,Al)N: croissance par épitaxie sous jets moléculaires, propriétés optiques, application aux diodes électroluminescentes*, Ph.D. thesis, Nice-Sophia Antipolis (2001)

[65] M. Cesaria, A. Caricato and M. Martino, *Realistic absorption coefficient of ultrathin films*, Journal of Optics **14** (10) 105701 (2012)

[66] W. Braun, *Applied RHEED: reflection high-energy electron diffraction during crystal growth*, 154, Springer (1999)

[67] Z. L. Wang, *Reflection electron microscopy and spectroscopy for surface analysis*, Cambridge University Press (2005)

[68] J. C. Vickerman and I. S. Gilmore, *Surface analysis: the principal techniques*, volume 2, Wiley Online Library (2009)

[69] A. Ichimiya, *Reflection high-energy electron diffraction*, Cambridge University Press (2004)

[70] S. D. Kevan, *Angle-Resolved Photoemission: Theory and Current Applications*, Elsevier (1992)

[71] R. Schlier and H. Farnsworth, *Structure and adsorption characteristics of clean surfaces of germanium and silicon*, The Journal of Chemical Physics **30** 917 (1959)

[72] M. Dabrowska-Szata, *Analysis of RHEED pattern from semiconductor surfaces*, Materials chemistry and physics **81** (2) 257–259 (2003)

[73] L. Reimer, *Scanning Electron Microscopy: Physics of Image Formation and Microanalysis*, Springer (1985)

[74] J. Goldstein et al., *Scanning electron microscopy and X-ray microanalysis*, Springer (2003)

[75] B. E. Warren, *X-ray Diffraction*, DoverPublications. com (1969)

[76] E. J. Mittemeijer and P. Scardi, *Diffraction analysis of the microstructure of materials*, volume 68, Springer (2004)

[77] A. Guinier, *X-ray diffraction: in crystals, imperfect crystals, and amorphous bodies*, Courier Dover Publications (2013)

[78] B. D. Cullity and S. R. Stock, *Elements of X-ray Diffraction*, volume 3, Prentice hall Upper Saddle River, NJ (2001)

[79] B.-R. Yeom et al., *Growth behavior of GaN epilayers on Si (111) grown by GaN nanowires assisted epitaxial lateral overgrowth*, CrystEngComm **14** (17) 5558–5563 (2012)

[80] Y. Itikawa, *Cross sections for electron collisions with nitrogen molecules*, J. Phys. Chem. Ref. Data **35** (1) 31–54 (2006)

[81] A. V. Phelps, *Cross Sections and Swarm Coefficients for Nitrogen Ions and Neutrals in N_2 and Argon Ions and Neutrals in Ar for Energies from 0.1 eV to 10 keV*, J. Phys. Chem. Ref. Data **20** 557 (1991)

[82] J. Bacri and A. Medani, *Electron diatomic molecule weighted total cross section calculation: III. main inelastic processes for N_2 and N_2^+*, Physica B+ C **112** (1) 101–118 (1982)

[83] S. Adamson et al., *Multiscale multiphysics nonempirical approach to calculation of light emission properties of chemically active nonequilibrium plasma: application to Ar–GaI3 system*, J. Phys. D: Appl. Phys. **40** (13) 3857 (2007)

[84] Y. Raizer, *Physics of gas discharge*, Springer-Verlag (1987)

[85] A. Fridman, *Plasma chemistry*, Cambridge Univ Pr (2008)

[86] K. Behringer and U. Fantz, *Spectroscopic diagnostics of glow discharge plasmas with non-Maxwellian electron energy distributions*, J. Phy **27** 2128 (1994)

[87] R. B. Bird, W. E. Stewart and E. N. Lightfoot, *Transport phenomena*, volume 2, Wiley New York (1960)

[88] G. L. Rogoff, *The diffusion length for gas discharge columns with electron production and loss rates linear and quadratic in electron density*, J. Appl. Phys. **52** (11) 6601–6607 (1981)

[89] A. L. Louarn, *Première étape de la croissance de GaN sur Si(111): la nucléation d'AlN*, Ph.D. thesis, Nice-Sophia Antipolis (2006)

[90] P. Chen et al., *Growth of high quality GaN layers with AlN buffer on Si(111) substrates*, J. Cryst. Growth **225** (2–4) 150 – 154 (2001), proceedings of the 12th American Conference on Crystal Growth and Epitaxy

[91] P. Hageman et al., *High quality GaN layers on Si (111) substrates: AlN buffer layer optimisation and insertion of a SiN intermediate layer*, physica status solidi (a) **188** (1/2) 523–526 (2001)

[92] E. Calleja et al., *Effect of Ga/Si interdiffusion on optical and transport properties of GaN layers grown on Si(111) by molecular-beam epitaxy*, Phys. Rev. B **58** 1550–1559 (1998)

[93] T. Lei et al., *Epitaxial growth of zinc blende and wurtzitic gallium nitride thin films on (001) silicon*, Appl. Phys. Lett. **59** (8) 944–946 (1991)

[94] P. Kung et al., *High quality AIN and GaN epilayers grown on (001) sapphire,(100), and (111) silicon substrates*, Appl. Phys. Lett. **66** (22) 2958–2960 (1995)

[95] B. Yang et al., *Structural properties of GaN layers on Si (001) grown by plasma-assisted molecular beam epitaxy*, J. Appl. Phys. **83** (7) 3800–3806 (1998)

[96] J. Ristić et al., *On the mechanisms of spontaneous growth of III-nitride nanocolumns by plasma-assisted molecular beam epitaxy*, J. Cryst. Growth **310** (18) 4035–4045 (2008)

[97] K. J. Lee et al., *Growth of high quality GaN epilayers with Si_xN_y inserting layer on Si(111) substrate*, Journal of the Korean Physical Society **45** (DEC) S756–S759 (2004)

[98] S. Nikishin et al., *High quality GaN grown on Si (111) by gas source molecular beam epitaxy with ammonia*, Appl. Phys. Lett. **75** (14) 2073–2075 (1999)

[99] S. Zhou et al., *Comparison of the properties of GaN grown on complex Si-based structures*, Appl. Phys. Lett. **86** (8) 081912–081912 (2005)

[100] P. Chen et al., *Deposition and crystallization of amorphous GaN buffer layers on Si (111) substrates*, J. Cryst. Growth **213** (1) 27–32 (2000)

[101] H. Marchand et al., *Metalorganic chemical vapor deposition of GaN on Si (111): Stress control and application to field-effect transistors*, J. Appl. Phys. **89** (12) 7846–7851 (2001)

Acknowledgements

Effectuer une thèse n'est pas une mince affaire et cela n'aurait pas pu être possible sans mes superviseurs, collègues et amis. J'aimerais donc remercier chaleureusement mon directeur de thèse Christoph Hollenstein et mon co-directeur Minh Quang Tran, premièrement de m'avoir permis de faire ce travail de doctorat dans leur groupe et de m'avoir guidé tout du long durant ces quatre années de labeur. Lors des nombreuses discussions et réunions, Christoph a su me corriger et me diriger vers mon but grâce à ses connaissances énormes en terme de phyisque des plasmas. Son aide précieuse m'a permis de ne pas me noyer dans les méandres de cette physique somme toute difficile.

Cette thèse n'aurait pas pu être effectuée sans la collaboration de notre partenaire industriel Sulzer Metco AG, que je remercie également. Je tiens aussi à remercier Matthias pour l'installation du réacteur de dépôt, ainsi que de la mise en place du système d'automatisation, et ce malgré la distance hebdomadaire à parcourir, afin de venir à Lausanne. Merci aussi au LASPE, laboratoire sans lequel les analyses de couches n'auraient pas pu être effectuées. Cette thèse n'aurait pas vu le jour non plus sans l'aide aussi bien au laboratoire qu'aux analyses de couches de Pierre Demolon, avec qui j'ai eu énormément de plaisir à travailler. Merci mon lapin!

Je voudrais également remercier les membres du jury Holger Kersten, Nicolas Grandjean et Malko Gindrat d'avoir accepté de juger mon travail et pour leur temps consacré à lire et commenter cette thèse.

Je tiens aussi à remercier chaleureusement tous les membres présents et passés du groupe des plasmas industriels: Alan, Pierre, Michael, Boris, Marina, Sylvain, David, Hamster, Loïc, Rémy et Philippe. Merci à tous pour les bons moments passés en votre compagnie, que ce soit à midi pour des discussions aussi douteuses qu'intéressantes sur les tendances politiques, en passant par les week-ends extraordinaires des uns et les problèmes de santé des autres. Merci aussi à ceux qui ont osé se mesurer à moi lors des nombreuses parties de fléchettes, tantôt m'humiliant, tantôt se prenant une bien belle raclée. À Alan pour ses "french jokes", pour sa joie de vivre parfois dissimulée et surtout pour ses aussi impressionnantes connaissances de la physique. À Michael pour les sujets plus sérieux amenés sur la table lors des pauses de midi, pour ses invitations aux soirées jeux de plateau et pour ses visites organisées dans les Grisons, et surtout de ne pas avoir abimé

ma voiture lors des cours de conduite. À Boris pour l'apport de la cible de fléchette, qui est toujours au bureau, et pour les discussions plasmiques. À Hamster mon frère valaisan toujours là pour défendre avec ferveur nos valeurs et nos origines. À Loïc pour ses points de vue souvent différents lors des débats, et pour la transmission de sa passion de la musique classique. À Rémy pour accentuer la touche française du groupe et pour les colis passés en douce à la frontière. À Philippe pour ses critiques sanglantes sur mes présentations, rapports et autres façons de travailler, au désodre créé au laboratoire, aux appareils empruntés pour une durée indéterminée et pour les très nombreuses parties de fléchettes. Merci à tous et à ceux que j'ai oubliés.

J'aimerais également remercier ceux sans qui la science ne progresserait pas: tous les techniciens du CRPP (ateliers mécanique, électrique et du vide), spécialement aux travailleurs acharnés que sont Christian, pour tous les tuyaux, lignes de gaz et autres pièces spéciales, Steve, pour tous les problèmes électriques, Nelson et William pour toutes les pièces mécaniques. Merci aussi aux secrétaires du CRPP pour leur aide dans le brouillard administratif: Edith, Heidi, Séverine, Colin, Céline, Roxanne et à Anh, secrétaire de l'école doctorale.

Un grand merci aussi à mes amis, qui m'ont soutenu et permis de me changer les idées lors des moments difficiles, et pour les soirées poker, souper, sorties dans la vaudoisie lointaine: Guillaume L., Yannick, Laurent, Guillaume M., Rolando et tous ceux que j'oublie.

Les personnes les plus importantes restent encore à remercier: ma famille. Stéphanie, mon amie, qui a toujours été à mes côtés pour m'épauler, me supporter et m'encourager, surtout lors des moments difficiles, mon frère pour les joyeux moments en moto et lors des repas de famille, et en particulier mes parents qui m'ont soutenu corps et âme lors de mon parcours d'étudiant et qui ont toujours été là pour moi.

Un grand merci à tous!

CURRICULUM VITAE

David MARTINET

Ch. du Vallon 14
3960 Sierre
Switzerland

Tel.: +41 (0) 79 488 21 41
E-mail: dav.martinet@gmail.com

Nationality: Swiss

Marital status: Single

Date of birth: 24.04.1986

PLASMA PHYSICS DOCTOR-ENGINEER

EDUCATION

Since February 2010

PhD thesis in Plasma Physics at the *Centre de Recherche en Physique des Plasmas* (CRPP) in *Swiss Federal Institute of Technology* (EPFL), Lausanne, Switzerland. Directed by Ch. Hollenstein

“Characterisation and modelling of nitrogen plasmas for the deposition of nanostructured GaN using different plasma sources”

2005-2010

Master of Sciences MSc in Physics, at the *Faculté des Sciences de Base* (FSB), EPFL

Master thesis in plasma processing, financial support from Oerlikon Solar

2000-2005

Swiss Scientific Federal Matura, option Physics at the *Lycée Collège des Creusets*, Sion.

Bilingual formation: french and german

PROFESSIONAL EXPERIENCE & PROJECTS

2010-2014

PhD position, in the frame of a CTI project in collaboration with *Sulzer Metco* and the *Laboratory of Advanced Semiconductors for Photonics and Electronics* (LASPE) at EPFL: “Development of industrial gas-metal plasma sources for the deposition of nanostructured GaN semiconductor layers for lighting applications”

- Characterisation of DC and RF plasmas in two different plasma reactors using Langmuir probe, Faraday cup and optical emission spectroscopy (OES)
- Investigation of various reactor configurations to study the plasma characteristics
- Epitaxy of GaN layers and nanostructures on 4” Silicon substrates by Low-Energy Plasma-Enhanced Vapor Phase Epitaxy (LEPEVPE)
- Continuous development of two different plasma reactors with both DC and RF plasma source configurations

Teaching assistant in *General Physics lectures* for several professors at EPFL, supervising exercises lectures, conception of exercises and tests for the students.

2009 (5 months)

Collaborator at *Etat de Vaud*, Service immeubles, patrimoine et logistique (SIPAL), Lausanne

Consolidation of data (heating and electricity consumption, maintenance contracts) and creation of energy certificates to supply projects and budget allocating

LANGUAGES AND COMPUTER SKILLS

▪ French :	mother tongue
▪ English:	C1, fluent
▪ German:	B1, conversational
▪ Scientific tools:	Matlab, Mathematica, COMSOL Multiphysics, LabView, C++
▪ Office software:	Origin, Word, Excel, PowerPoint, LaTeX